Study of the electronic states in heavy fermion compound URu_2Si_2

Ph. D Thesis

December 2013

Department of Physics, Graduate School of Science,
Kyoto University, Kyoto, Japan

Sho Tonegawa

Abstract

Quantum many-body problem is one of the grand challenges in the condensed matter physics. The most striking consequence of interactions among many particles is the appearance of new phases whose collective dynamics is very different from that of a few particles. The important clue to know how the order changes during the phase transition is the elucidation of the order parameter in the system. Especially, for second-order phase transitions, the nature of the transition is most fundamentally characterized by spontaneous symmetry breaking and the degree of symmetry breaking can be described by an order parameter with a reduced symmetry in the low-temperature ordered phase. In the ferromagnetic transition, for instance, the order parameter is the magnetization and breaks the spin rotation symmetry, whereas in the superconducting transition a gauge symmetry is broken.

In this thesis, we will focus on the unusual properties of the heavy fermion compound URu_2Si_2. This compound undergoes at 17.5 K a phase transition accompanying a huge amount of entropy loss, but no magnetic and structural ordering have been observed. Despite considerable experimental and theoretical efforts for more than a quarter century, the order parameter is not yet totally understood and therefore the phase is called "hidden order phase" In general, a second-order phase transition causes a change in various types of symmetries, such as crystal, rotational, gauge and time reversal symmetries. Therefore the key to the nature of hidden order lies in understanding which symmetry is being broken. Recent magnetic torque measurements reveal the in-plane anisotropy of magnetic susceptibility, which suggests that the crystal C_4 rotational symmetry in the tetragonal URu_2Si_2 is broken below the hidden order phase transition. This newly suggested rotational symmetry breaking has raised several theoretical proposals, and calls for further experimental verifications by using other techniques.

The experimental determination of broken symmetries is the most essential step toward elucidating the nature of the hidden order phase transition. One of the most direct ways of observing such symmetry breaking is to use X-ray diffraction, which sensitively probes the lattice symmetries. In solids we always have finite electron-lattice coupling, and when the electronic system breaks one of the symmetries of the crystal structure at the transition, then the same symmetry should also be broken in the lattice at the same time. If the electron-lattice coupling constant is small, the amount of lattice change (or distortion) may also be small, and experiments focusing on particular Bragg points may be required to achieve the highest resolution. In the previous crystal-structure studies on URu_2Si_2, no symmetry

change has been detected for $[h00]$ and $[00l]$ directions. We therefore perform high-resolution synchrotron X-ray crystal-structure analysis for a high-angle (880) Bragg diffraction by four-circle diffractometer. These results reveal tiny but finite orthorhombic distortion of the order of 10^{-5} (or lattice constant change less than 100 fm), which is discussed in Chapter 3.

The nature of electronic orders in metals and semiconductors is, in general, closely related to the electronic structure, and the most essential information is the structure of Fermi surface. In the case of URu_2Si_2, the large loss of entropy below $T_{\rm HO}$ signifies that a large portion of the Fermi surface is gapped in the hidden order phase, which has also been supported by the transport and tunneling measurements. For the understanding of the nature of hidden order, it is indispensable to determine how the electronic structure changes with the gap formation, and in particular it is important to clarify how this is related to the rotational symmetry breaking suggested by the torque measurements. We therefore perform cyclotron resonance measurements in the hidden order phase, which allows the full determination of angle-dependent electron-mass structure of the main Fermi-surface sheets. Furthermore, we find an anomalous splitting of the sharpest resonance line under in-plane magnetic-field rotation. This is most naturally explained by the domain formation, which breaks the fourfold rotational symmetry of the underlying tetragonal lattice. The results reveal the emergence of an in-plane mass anisotropy with hot spots along the [110] direction, which can account for the anisotropic in-plane magnetic susceptibility reported recently. These results are shown in Chapter 4.

Another important aspect of URu_2Si_2 is that the hidden order phase hosts the unconventional superconducting phase below the transition temperature $T_{\rm SC} = 1.4$ K at ambient pressure. The cyclotron mass m_{CR} in the superconducting state has also been a subject of theoretical debate. By considering the ac dynamics of superconducting vortices, a theory predicts the violation of the Kohn's theorem and a peculiar temperature dependence of the resonance frequency in clean type-II superconductors. Experimentally, however, this point has not yet studied mainly because the observation of cyclotron resonance in the superconducting state is difficult due to the limitation of microwave penetration depth which is usually short. By using a ^{3}He microwave cavity we are able to observe cyclotron resonance in the superconducting phase of URu_2Si_2. Contrary to the proposed temperature dependence, we find that the mass does not show any significant change below T_{SC}. We rather find that the scattering rate at low temperatures exhibits characteristic temperature dependence; it shows non-Fermi liquid-like quasi T-linear dependence followed by a sudden decrease below the vortex-lattice melting transition temperature, which has been determined by the resistivity measurements. This supports the formation of a coherent quasiparticle Bloch state in the vortex lattice phase. These results are shown in Chapter 5.

Finally we will summarize and conclude the our study in Chapter 6.

Contents

Chapter 1

Introduction

The heavy-fermion systems which contain the lanthanide or actinide compounds have been studied extensively for almost two decades. In heavy-fermion compounds, the magnetic moment of localized f electrons are present in every Ce($4f$) or U($5f$) atoms. The f electrons behave like diluted magnetic moments in spite of their periodicity just above the Kondo-temperature. On the other hand, at a still lower temperature T_{coh} Kondo coherence effects start to play a role and the correlations between spins of conduction electrons and the moment of f electrons become important. Below this temperature Bloch waves develop and a band of quasiparticles is formed. In these Kondo lattices the resistivity drops strongly due to coherent scattering and the effective electron mass m^* is renormalized, which can be up to 1000 times larger than that of free electron (that is a origin of a name "heavy-fermion"). In spite of the strong renormalization, the low temperature behavior of macroscopic properties in heavy fermion systems can first be analyzed by Fermi-liquid picture. In this theory strongly interacting fermions are substituted by weakly interacting quasiparticles with an enhanced effective mass. This theory results large specific heat C, susceptibility χ and A value of the resistivity ($\rho(T) = \rho_0 + AT^2$) at low temperature and crudes proportionality of C/T, χ and A to m^* and m^{*2} is roughly valid. By contrast in $3d$ itinerant magnetism this proportionality is not observed.

The simpler examples of heavy-fermion metals are well understood within theoretical frameworks based on the Kondo lattice, where the f electrons which localize at high temperature become itinerant at low temperature through Kondo hybridization with the conduction electrons. On the other hand, the local moments interact indirectly via the conduction electrons by the Ruderman-Kittel-Kasuya-Yoshida (RKKY) interaction, which favors parallel as well as antiparallel orientation of the moments at neighboring sites. Kondo interaction and RKKY interaction both depend on the exchange J between the conduction electrons and the f electrons. The system will take the ground state with the lower energy. If the RKKY interaction is stronger, this will be a magnetic ground state but if the Kondo interaction is stronger it will be a non-magnetic one. The competition of those two interactions has been studied by Doniach diagram [1]. The competition between the RKKY interaction which favors long range magnetic order and the moment screening of Kondo effect leads to differ-

ent ground states in heavy fermion systems. At zero temperature the system can be driven from a magnetically ordered ground state to an non-magnetic state by changing a parameter other than temperature. Moreover, the characteristic energy scales of heavy fermions are comparably low, which indicates the strength of the two competing forces can be tuned by conveniently accessible values of pressure, magnetic field or chemical substitution. Such a phase transition happens at a quantum critical point. In the vicinity of this point usually the typical properties of a Fermi liquid are violated at least down to a rather low temperature and so-called Non-Fermi-liquid behavior is found. In addition to quantum criticality and non-Fermi liquid behavior, the competition of various interactions arising from Kondo physics in heavy-fermion materials makes a wide variety of characteristic phenomena such as multipolar ordering, unconventional superconductivity, Kondo insulator and metamagnetism, *etc*. Furthermore, heavy fermion compounds usually have complicated 3D Fermi surfaces, which makes their unusual properties more complicated. For these reasons, the elucidation of fundamental electronic properties in heavy-fermion materials is challenging and continuously draws the attention of experimental and theoretical physicists.

In the $5f$ electrons U-based systems the effective radial charge density of the U atom are less localized than than that of $4f$ electrons Ce-based systems. This indicates f-state in U-based compounds has a duality, that is to say, itinerant and localized characters. In the dual model, the itinerant electrons hybridize with the conduction states and form energy bands while the localized ones form multiplets to reduce the local Coulomb repulsion. The two subsystems interact, leading to a mass enhancement of the delocalized quasiparticles. This dual picture gives a natural description of heavy-fermion superconductivity coexisting with $5f$-derived magnetism. For example, UPt_3, UPd_2Al_3 and UNi_2Al_3 superconductors coexists antiferromagnetism [2–4] and UGe_2, URhGe, UIr and UCoGe superconductors coexists ferromagnetism [5–8]. The coexistence of magnetism and superconductivity indicates that the Cooper pairs are formed magnetically mediated interactions in these systems, although the superconducting gap structures of these materials have not yet been clarified. In particular, a highly unusual superconducting state is expected in URu_2Si_2, since it coexists with a mysterious "hidden order", whose order parameter has not been clarified.

Chapter 2

Heavy fermion compound URu_2Si_2

2.1 Crystal structure & Phase diagram

After the discovery of the heavy-fermion compound URu_2Si_2 [9–11], it has been attracted much attention for its mysterious phase, the so called hidden-order phase, whose order parameter is not yet identified despite intense experimental and theoretical efforts more than a quarter century. In the high-temperature disordered phase, URu_2Si_2 has a body-centered tetragonal $ThCr_2Si_2$-type structure(see Fig. 2.1a) belonging to the $I4/mmm$ symmetry group (No. 139 in the international tables for crystallgraphy). The lattice constants are $a = 4.1327(3)$ Å and $c = 9.5839(6)$ Å at 300 K and atomic coordinates are summarized in the Table 2.1.

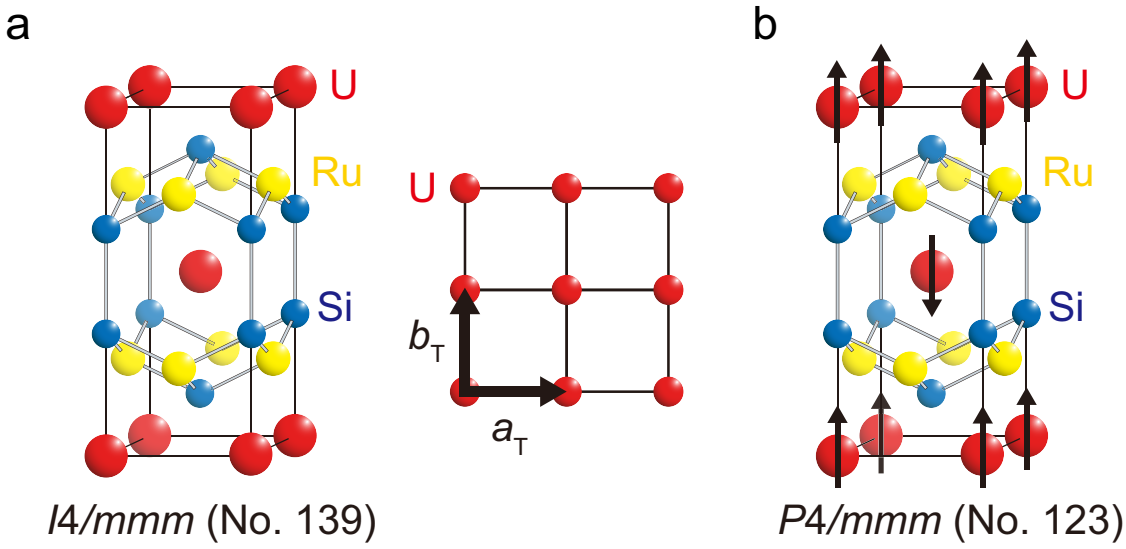

Figure 2.1: a. The body-center tetragonal crystals structure of URu_2Si_2 in the paramagnetic phase and a schematic picture of U-site configuration. b. The same body-center tetragonal crystal structure of URu_2Si_2 with known long-range magnetic order in the antiferromagnetic state. The arrows represent the magnetic moment of U atoms aligned antiferromagnetically along c-axis.

Table 2.1: Atomic coordinates of URu_2Si_2 at 300 K from X-ray measurements [12, 13].

$I4/mmm$	Atom	Position		
(No. 139)	(site)	x	y	z
$a = 4.1327(3)$ Å	U ($2a$)	0	0	0
$c = 9.5839(6)$ Å	Ru ($4d$)	0	1/2	1/4
$V = 163.685(17)$	Si ($4e$)	0	0	0.3724(5)

Some pressure induced experiments have been revealed the relation between hidden order and the antiferromagnetic (AFM) state [14–20]. In this pressure-induced antiferromagnetic phase URu_2Si_2 has type-I AFM with ferrmagnetic a-a planes, alternating antiferromagnetically along the c-direction, whose space group is $P4/mmm$ as shown in Fig. 2.1b. The AFM ordering vector of $Q_{\mathrm{AF}} = (0, 0, 1)$ indicates the zone folding associated with the lattice doubling and such a zone folding has also been suggested by the recent angle-resolved photoemission [21–23] study in the hidden-order phase when compared with the Fermi surface above T_{HO} [24–26], which further supports the similarity between AFM and the hidden order states. The electronic structure in AFM state is discussed in more detail later.

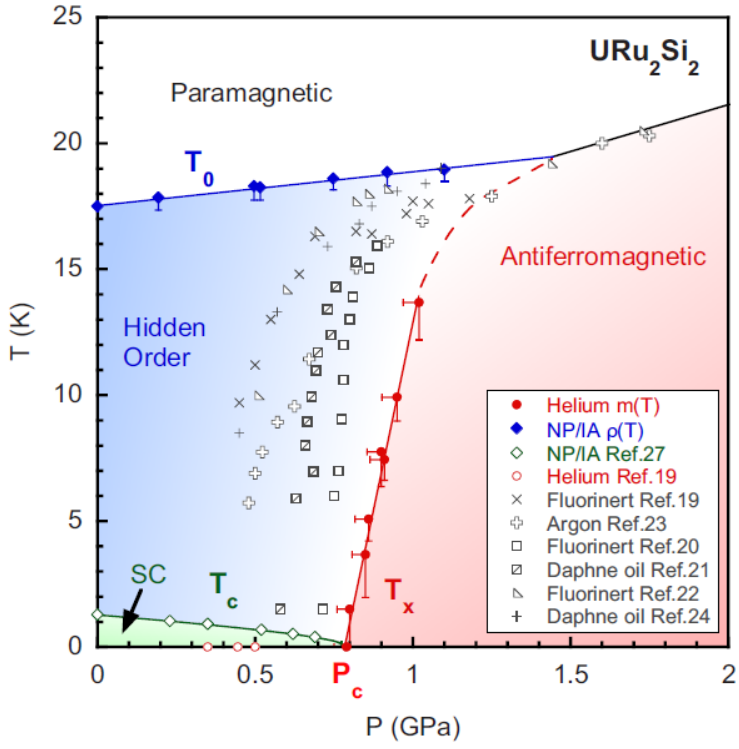

Figure 2.2: Pressure-temperature phase diagram of URu_2Si_2 [14]. The some phase boundaries between hidden order and AFM phase revealed various experiments [15–20] are displayed and show the almost same behavior.

Crystal structure with broken rotational symmetry

Recent magnetic torque measurements [27] and NMR experiments [28], discussed in detail later, reveal that the tetragonal rotational symmetry is broken below the hidden order phase transition. The $I4/mmm$ symmetry group (No. 139) has seven maximal non-isomorphic t subgroups, eight maximal non-isomorphic k subgroups. Among them, the only two $Immm$ and $Fmmm$ space groups break the in-plane rotational symmetry (Fig. 2.3). In the $Immm$-type orthorhombic structure, the U atom arrangements are in a rectangle shape (Fig. 2.3b). On the other hand, the $Fmmm$-type orthorhombic distortion demands the unit cell axes are rotated $\pi/4$ about the c-axis and a and b lattice parameters are multiplied by about $\sqrt{2}$, respectively (Fig. 2.3a).

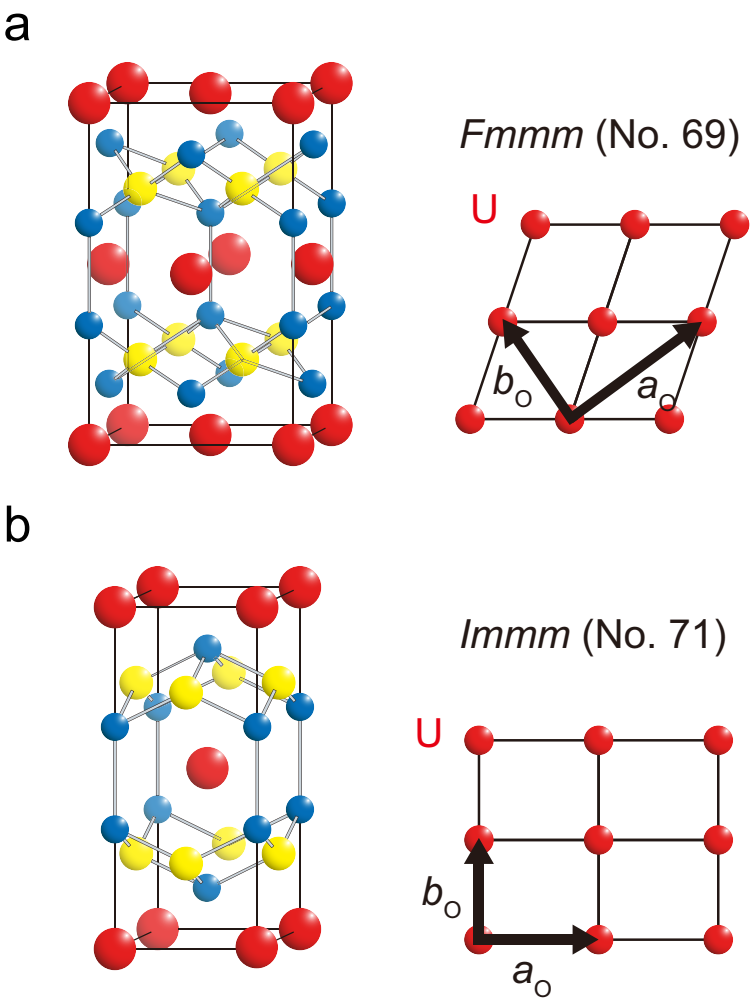

Figure 2.3: Crystals structure with the broken rotational symmetry in $I4/mmm$ symmetry group: **a**. $Fmmm$ (No. 69), **b**. $Immm$ (No. 71). The right figure is a schematic picture of U-site. The unit vector a_O, b_O is shown on it ($a_O > b_O$).

2.2 Transport experiments in the hidden order phaase

The heavy-fermion compound URu_2Si_2 has attracted much attention for its mysterious phase, the so called hidden-order (HO) phase, whose order parameter is not identified despite intense experimental and theoretical efforts for more than a quarter century. Various thermodynamic and transport properties show a large anomaly at the HO transition at $T_{HO} = 17.5\,\mathrm{K}$.

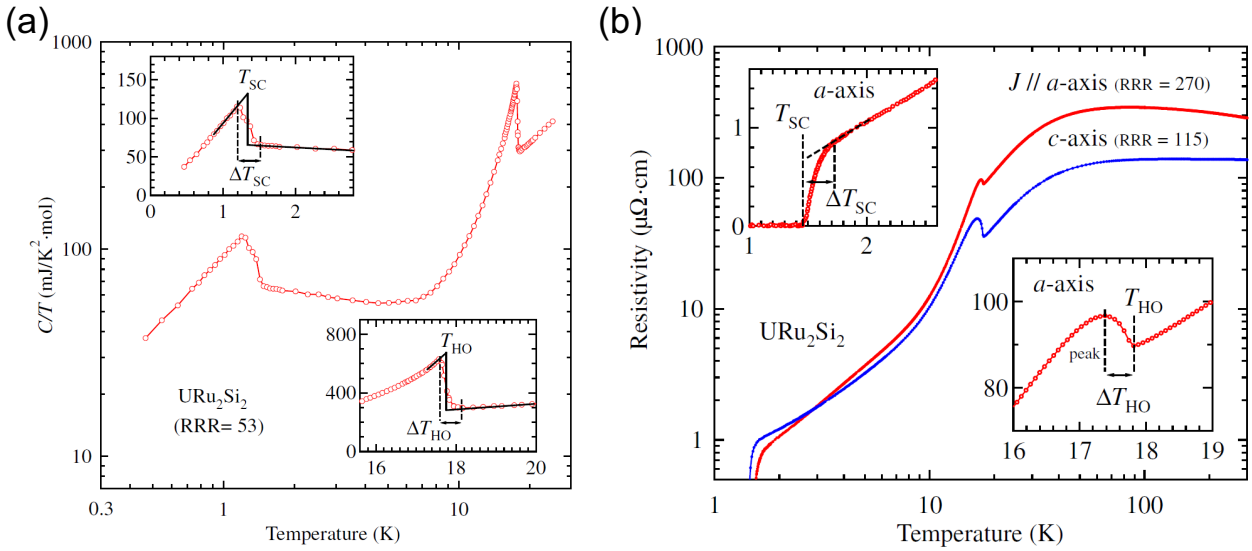

Figure 2.4: (a) Specific heat plotted as C/T as function of T. (b) Temperature dependence of the electrical resistivity ρ for current along a- and c-axis. ρ exhibits a distinct peak immediately below T_{HO} [12, 13].

Figure 2.4 (a) show the temperature dependence of the specific heat [12, 13]. Sharp specific heat anomalies are observed at $T_{HO} = 17.5\,\mathrm{K}$ and at $T_{SC} = 1.4\,\mathrm{K}$, which is linked to the second order phase transition. At $T_{HO} = 17.5\,\mathrm{K}$, the specific heat reduces its magnitude from $\simeq 180\mathrm{mJ/mol\,K^2}$ to $\simeq 70\mathrm{mJ/mol\,K^2}$ with a concomitant reduction of carrier density due to the gap opening at the HO transition. The distinct reduction of entropy in this HO transition reach $\Delta S \simeq 0.2 k_B \ln 2$ per formula unit. The specific heat jump at $T_{SC} = 1.4\,\mathrm{K}$ suggests the superconducting transition. Figure 2.4 (b) depicts the temperature dependence of the resistivity [12, 13]. At the HO transition, the resistivity shows a jump due to the opening gap and in the HO state the experimental data is well fitted by using a simple formula: $\rho(T) = \rho_0 + AT^x + B\exp(-\Delta/T)$, where ρ_0 is the residual resistivity and Δ is energy gap. By fitting, The gap size shows $\Delta \simeq 90\mathrm{K}$ for $J \parallel a$ and $\Delta \simeq 70\mathrm{K}$ for $J \parallel c$, which are closet to the gap estimated from the specific heat. The temperature dependence of resistivity follow $T^{1.5}$ behavior which is not different from $x = 2$ expected from Fermi liquid.

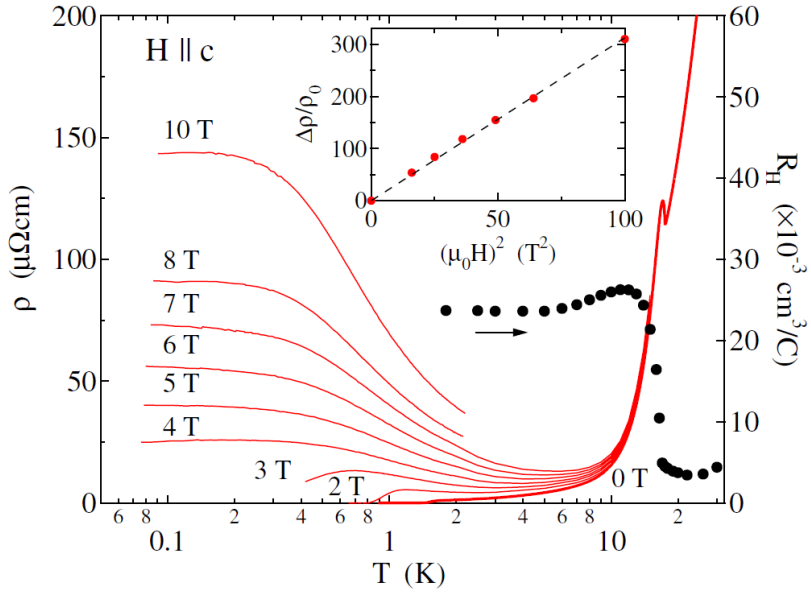

Figure 2.5: The temperature dependence of resistivity ρ (solid lines) in zero and finite magnetic fields ($\boldsymbol{H} \parallel c$) and the Hall coefficient R_H (solid circles). Inset shows the magnetoresistance at $T \to 0\,\mathrm{K}$ as a function of H^2 [29].

Figure 2.5 depicts the temperature dependence of the resistivity in several magnetic fields and the Hall coefficient R_H, where $R_\mathrm{H} \equiv d\rho_{xy}/dH$ at $H \to 0$ for $H \parallel c$ [29]. At high magnetic fields, ρ increases with decreasing temperatures, but then saturates at the lowest temperatures. The magnetoresistance $\Delta\rho/\rho$ at $T \to 0\,\mathrm{K}$ represents a nearly perfect H^2-dependence up to 10 T, which suggests URu_2Si_2 is a nearly compensated metal such as bismuth and graphite. In a compensated metal, the magnetoresistance $\Delta\rho/\rho$ is described as

$$\Delta\rho/\rho \simeq (\omega_c^e \tau^e)(\omega_c^h \tau^h), \tag{2.1}$$

where ω_c and τ are the cyclotron frequency and the scattering time, respectively. The Hall coefficient is given by

$$R_H = \frac{1}{ne} \times \frac{\sigma_h - \sigma_e}{\sigma_h + \sigma_e}, \tag{2.2}$$

where n denotes the carrier number and the suffixes e and h denote"electron" and "hole", respectively. At the upper critical field $H_{c2}^c = 2.8\,\mathrm{T}$, $(\omega_c^e \tau^e)(\omega_c^h \tau^h)$ is about 25, which is currently the maximum value among the type-II superconductors. The fact that the Hall coefficient R_H is positive indicates that the hole band dominates transport properties ($\sigma_h > \sigma_e$). Also, an about fivefold increase of R_H suggests that most carriers disappears below T_HO. The number of holes n_h, estimated from R_H as $n_h = 1/R_H e$ using a single band model, gives an upper limit of $n_h \simeq 2.6 \times 10^{26}\mathrm{m}^{-3}$, corresponding to 0.021 holes per U-atom. Consequently, these magneto-transport measurements have revealed a "semimetallic" electronic state is realized below T_HO in URu_2Si_2, characterized by the carrier compensation with small carrier density.

2.3 Electronic structure in the hidden order phase

Various experiments such as specific heat, thermal conductivity and Hall effect, show the gap opening in a large portion of Fermi surface (FS) below $T_{\mathrm{HO}} = 17.5\,\mathrm{K}$, leading to a large reduction of carrier density. This implies a drastic reconstruction of the electronic state at $T_{\mathrm{HO}} = 17.5\,\mathrm{K}$. For the understanding of the nature of hidden order, it is indispensable to determine how the Fermi surface topology changes with the gap formation. Experimental information on the Fermi surface topology in the hidden order state has been gained from nesting vectors revealed by neutron inelastic scattering experiments [30–32], and through extremal Fermi surface orbits, obtained from quantum oscillation measurements [33, 34].

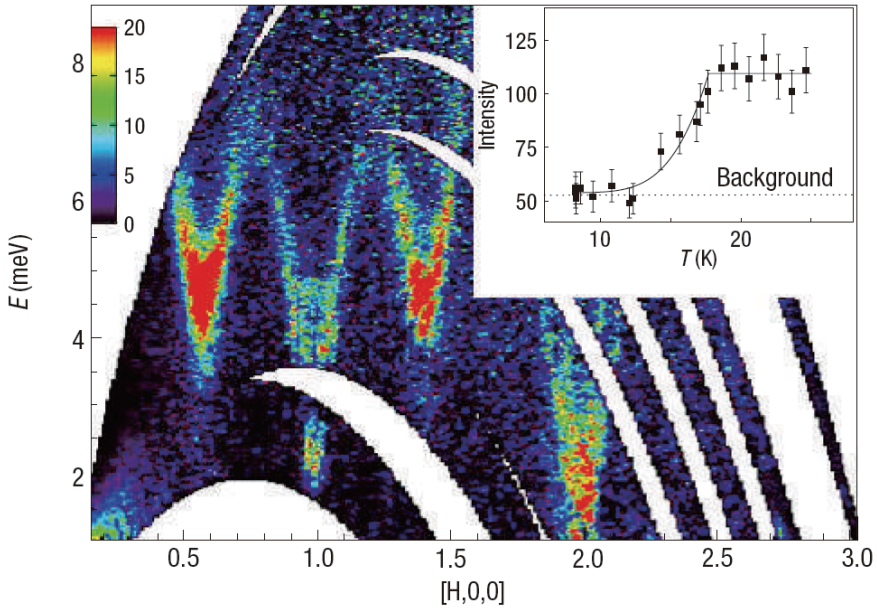

Figure 2.6: Inelastic neutron scattering of URu_2Si_2 in the $[H, 0, 0]$ plane at $T = 1.5$ K. The inset shows how the incommensurate excitations become gapped through the transition by counting at the point (0.6, 0, 0) at 0.25 meV [30].

Figure 2.6 shows the excitation spectrum of URu_2Si_2 revealed by Neutron inelastic experiments [30]. The gap is formed in the magnetic excitations characterized by two wave vectors: $\boldsymbol{Q}_C = (1, 0, 0) = (0, 0, 1)$ with an energy gap of $E_0 \cong 1.9\,\mathrm{meV}$ and $\boldsymbol{Q}_{IC} = (1 \pm 0.4, 0, 0)$ with an energy gap of $E_1 \cong 4 - 5.7\,\mathrm{meV}$. These inelastic magnetic responses for paramagnetic, HO and AFM phases are revealed by the inelastic neutron scattering experiments under hydrostatic pressure. The sharp low energy magnetic excitation at $\boldsymbol{Q}_C$ in the HO phase is strongly damped in the paramagnetic and AFM phase. On the other hand, the observed signal at $\boldsymbol{Q}_{IC}$ in the HO state persists on entering the antiferromagnetic phase. These results indicate that the low-energy resonance at $\boldsymbol{Q}_C$ plays an important role for the reconstruction of the Fermi surface in the HO phase.

2.3.1 Fermi surface of URu_2Si_2

Electronic band-structure is calculated in two steps [35]. First, the ab initio calculations are performed for the paramagnetic state of URu_2Si_2 by using the Wien2k package [36], in which the relativistic full-potential (linearized) augmented plane-wave (FLAPW) + local orbitals method is implemented. The crystallographical parameters are the space group No. 139, $I4/mmm$, the lattice constants, $a = 4.126$ Å, $c = 9.568$ Å, and Si internal position, z = 0.371 [37]. Then the Fermi surface in the antiferromagnetic state was obtained by applying several values of effective field, and the Brillouin zone is folded to the space group No. 123, $P4/mmm$. The obtained Fermi surface is essentially consistent with the previous density functional band-structure calculations [38].

Fermi surface in the Paramagnetic phase

Figure 2.7 shows a side view of the paramagnetic Fermi surface and the band structure near the Fermi energy. The drawn Fermi surface is essentially consistent with the previous calculations. The outer Fermi surface around Z point and the outer Fermi surface around Γ point reveal the existence of a nesting vector Q_C, as indicated by the arrow in Fig. 2.7. These two Fermi surface have a similar round curvature, favorable for nesting, with the exception that close to $Z/2$ where the Γ-centered sheet has a more pointed part. This nesting vector coincides accurately with the antiferromagnetic wave vector $Q_{\mathrm{AF}} = (0, 0, 1)$ indicated by the inelastic neutron experiments [30–32].

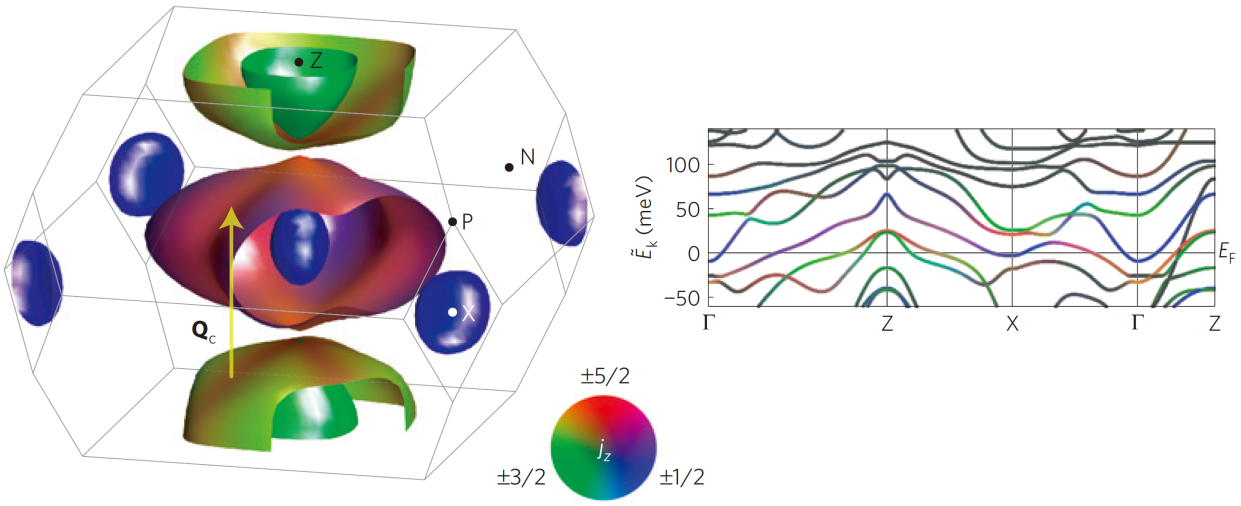

Figure 2.7: Schematic picture of the Fermi surface and enegy band dispersion of paramagnetic URu_2Si_2. The color indicates the weight of the j_z component: red, green and blue color gauges correspond to $j_z = \pm 5/2, \pm 3/2$ and $\pm 1/2$ components, respectively. The arrow indicates the antiferromagnetic nesting vector connecting the two Fermi surface sheets [35].

Fermi surface in the Antiferromagnetic phase

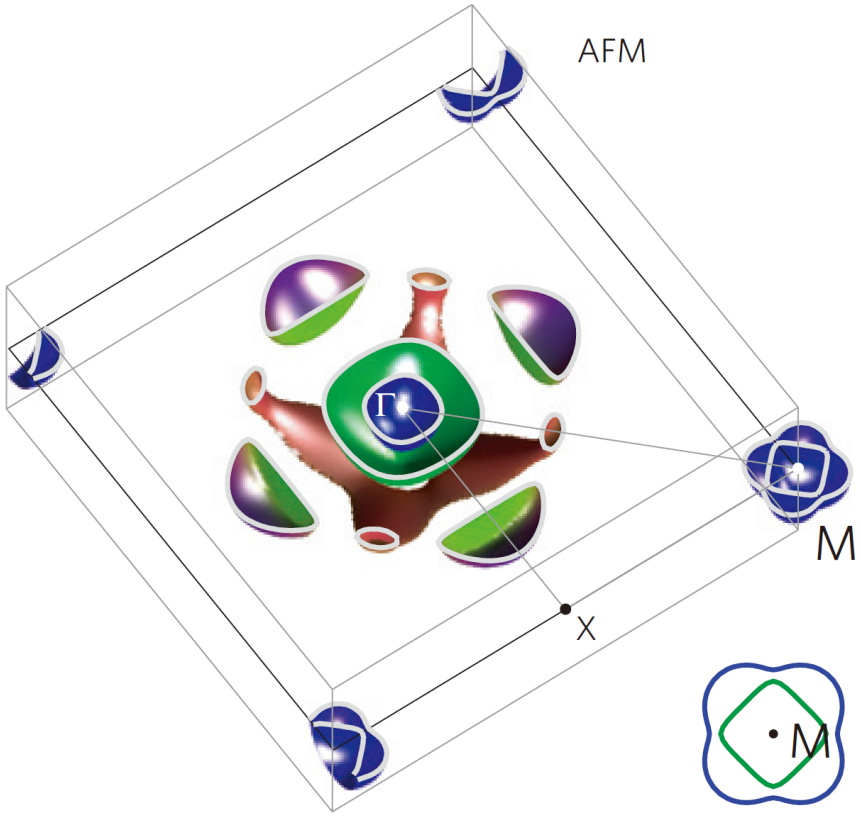

Figure 2.8: Two-dimensional cut of antiferromagnetic Fermi surface at $k_z = 0$. The effective field of 40 meV is used which corresponds to antiferromagnetic gap of $\sim$4 meV. High-symmetry points are indicated [35].

The antiferomagnetic Fermi surface sheets of URu_2Si_2 due to the band folding by the ordering vector $Q_{\mathrm{AF}} = (0, 0, 1)$ is displayed in Fig. 2.8 [35]. The results in Fig. 2.8 are obtained with the effective field of 40 meV, which corresponds to an antiferromagnetic gap of $\sim$4 meV when the renormalization of $\sim 1/10$ is taken into account.

There are six kinds of Fermi surfaces in the Brillouin zone:

(i) an outer large hole pocket at Γ point,
(ii) a small ellipsoidal electron pocket at Γ point,
(iii) four electron pocket around Γ in the shape of rounded half sphere,
(iv) a cross-shaped outer electron pocket at M point,
(v) a inner small electron pocket at M point,
(vi) the Fermi surface with a cage-like structure around Γ point.

Recent quantum oscillation experiments under pressure implies a similar electronic structure in both the hidden order and antiferrmagnetic state, which is discussed in the latter section.

2.3.2 Quantum oscillation experiments

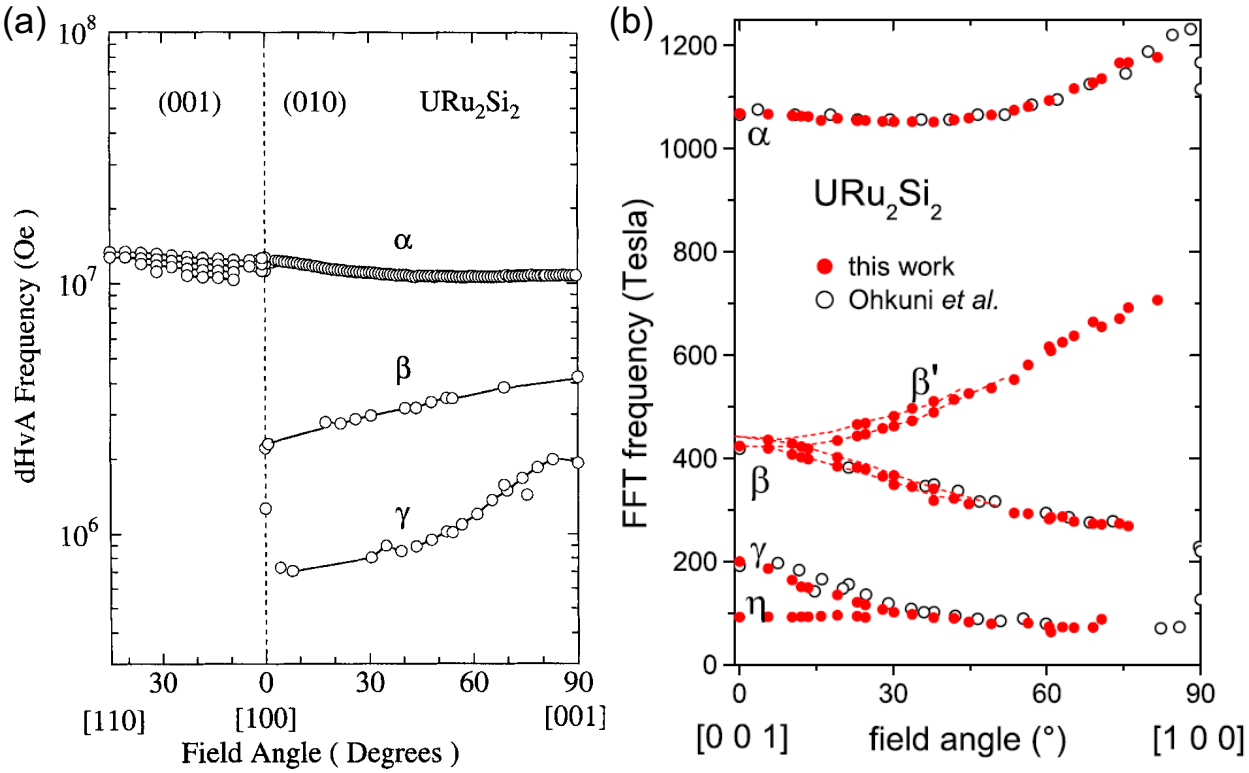

Figure 2.9: Field angular dependence of the FFT frequencies obtained from (a) dHvA [33] and (b) SdH [34] measurements in URu_2Si_2, reflecting the cross sectional areas of the different Fermi surface branches perpendicular to the magnetic field. The dHvA results are also plotted in (b) SdH results and are in excellent agreement.

The studies of quantum oscillations in the de Haas-van Alphen (dHvA) frequencies [33] and Shubnikov-de Haas (SdH) frequencies [34] can yield direct information on the Fermi surface. We compare quantum oscillation results with the band structure calculations assuming the antiferromagnetism in Fig. 2.8 and discuss the Fermi surface structure in the hidden-order phase. The angular dependences of the dHvA and SdH frequencies in the hidden order phase are shown in Fig. 2.9. The fundamental branches revealed in both experiments are named α, β and γ. The angular dependences of the SdH frequency of α, β and γ branches are coincident with the dHvA results.

The α branch is almost constant as a function of the field angle indicating that the Fermi surface is spherical in shape. Moreover, α branch has the largest dHvA frequency and large dHvA oscillation amplitude, which indicates α pocket has the largest volume in the Brillouin zone. For the above reasons, α branch corresponds to the outer hole pocket located around the center of the folded Brillouin zone (Γ point). The Fermi wavelength of α branch estimated from dHvA frequency is $k_F \simeq 1.8 \times 10^9\,\mathrm{m}^{-1}$ which corresponds 0.017 holes/U. Hall coefficient analysis using a single band model gives an upper limit $\simeq 0.021$ holes/U [29], which agree well with the quantum oscillation experiments.

The further branches labeled β' and η in addition to the three branches are observed by the recent SdH experiments (Fig. 2.9 (b)). The splitting of β branch indicates that the corresponding Fermi surface have two different orbits for $H//[100]$, but these two merge towards for $H//[001]$. For the topology reason, the β branch corresponds to non-central four pockets in the shape of half spheres in the $z = 0$ plane. The assigns of γ and η branches are discussed later with our cyclotron resonance results.

Table 2.2 summarizes the SdH frequencies and effective masses obtained by the SdH experiments [34]. The Sommerfeld coefficient γ is estimated by the Fermi wave length and the effective mass m^*, as shown by

$$\gamma \simeq \sum_i \frac{k_B^2 V m^* k_F}{3\hbar^2}, \tag{2.3}$$

assuming spherical isotropic Fermi surface, where $V = 49\,\mathrm{cm}^2/\mathrm{mol}$ is the molar volume and i is theindex of the branch. However, the calculated Sommerfeld coefficient $\gamma \simeq 37.5\,\mathrm{mJ/mol\,K}^2$ account for 55 % of $\gamma \simeq 65\,\mathrm{mJ/mol\,K}^2$ determined by the specific heat measurements. This result indicates there must be some Fermi surface sheets with heavy mass missing in these experiments.

Table 2.2: SdH frequencies and effective masses for the magnetic field parallel to a-axis and c-axis [34].

branch	$F_{H//c}$(T)	$F_{H//a}$(T)	$m^*_{H//c}$ (m_0)	$m^*_{H//a}$ (m_0)
α	1070	1230	12.4	11
β	422	219	23.8	13.5
β'	422	751		25
γ	195	73	10	2.9
η	93	93	20.5	20.5

SdH experiments under pressure

The α, β and η branches are observed by the SdH experiments under pressure [34], as shown in the Fig. 2.10(a). Fig. 2.10(b) shows the pressure dependence of the FFT frequencies. All observed branches indicate tiny change of the FFT frequencies at P_x, which is the transition presuure from HO to AFM phase. Consequently, no significant change of the band structure between the HO and the AFM phase is observed. These experiments indicate that the HO phase have the similar electronic structure proposed in the AFM phase, where tha band folding appears due to the ordering vector $Q_{\mathrm{AFM}} = (0, 0, 1)$. Fig. 2.10(c) show that all the masses decrease as increasing pressure. This decrease of the masses are related to the decrease of the A coefficient of the T^2 behavior of $\rho - \rho_0$ with pressure.

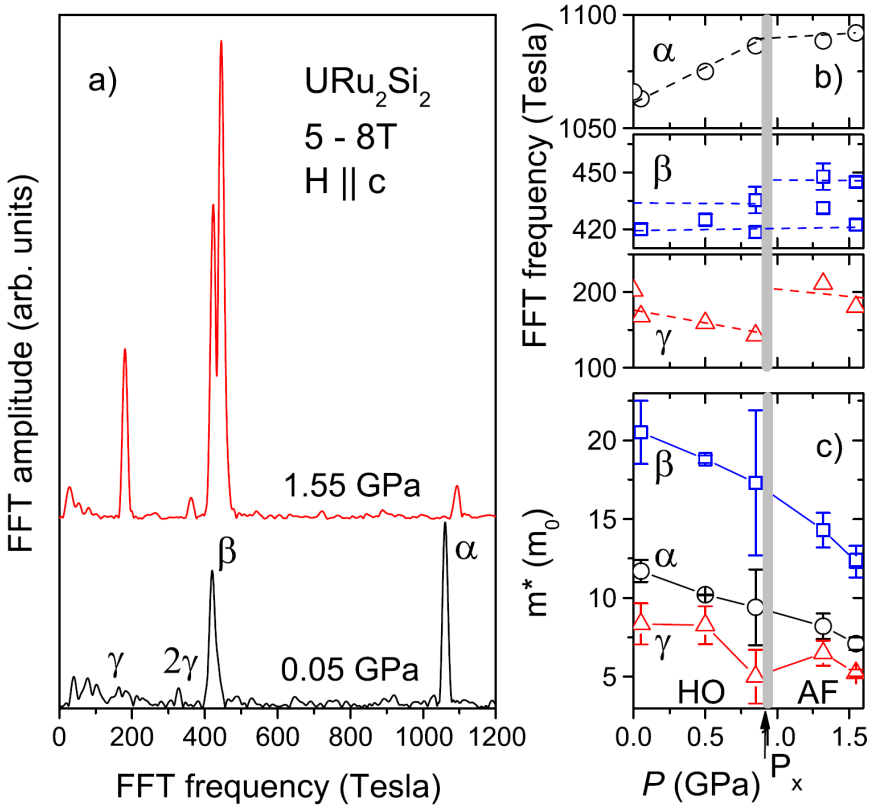

Figure 2.10: (a) FFT spectra of SdH measurements in URu_2Si_2 for $\boldsymbol{H} \parallel c$ at the lowest temperature of $T \simeq 35$ mK for $P = 0.05$ GPa and $T \simeq 35$ mK for $P = 0.05$ GPa. (b) Pressure dependence of the FFT frequencies. (c) Pressure dependence of the effective masses determined in afield range of 8-13 T [34].

2.3.3 Nematic state

A Second order phase transition is characterized by spontaneous symmetry breaking. However, despite more than 25 years intensive research, the fundamental question "which symmetry is broken in the hidden order phase?" has been unresolved. In order to elucidate the order parameter of the hidden order phase in URu_2Si_2, it is the most important to clarify the symmetry breaking at $T_{HO} = 17.5\,K$. Recently, magnetic torque measurements [27] and NMR experiments [28] show the in-plane anisotropic state in the hidden order, called "nematic state". The results of these experiments are detailed below.

Magnetic torque experiments

The in-plane magnetic torque is measured by a micro-tip cantilever, whose method has a high sensitivity for detecting magnetic anisotropy. In Fig. 2.11(a), a schematic picture of the magnetic torque measurement system is shown [27]. The magnetic field H rotates within the ab plane, where the azimuthal angle formed by H and a-axis is defined as ϕ. The magnetic torque is expressed as

$$\tau = \mu_0 MV \times H, \tag{2.4}$$

where M is the induced magnetization, H is the magnetic field, V is the sample volume, and μ_0 is the permeability of vacuum. The crystal structure of URu_2Si_2 in the paramagnetic state has four-fold symmetry, so that the in-plane magnetic torque in the paramagnetic phase also preserves C_4 symmetry. If the magnetic torque has the component of the two-fold oscillation in the HO phase, the rotational symmetry is broken in the HO phase (Fig. 2.11(b)).

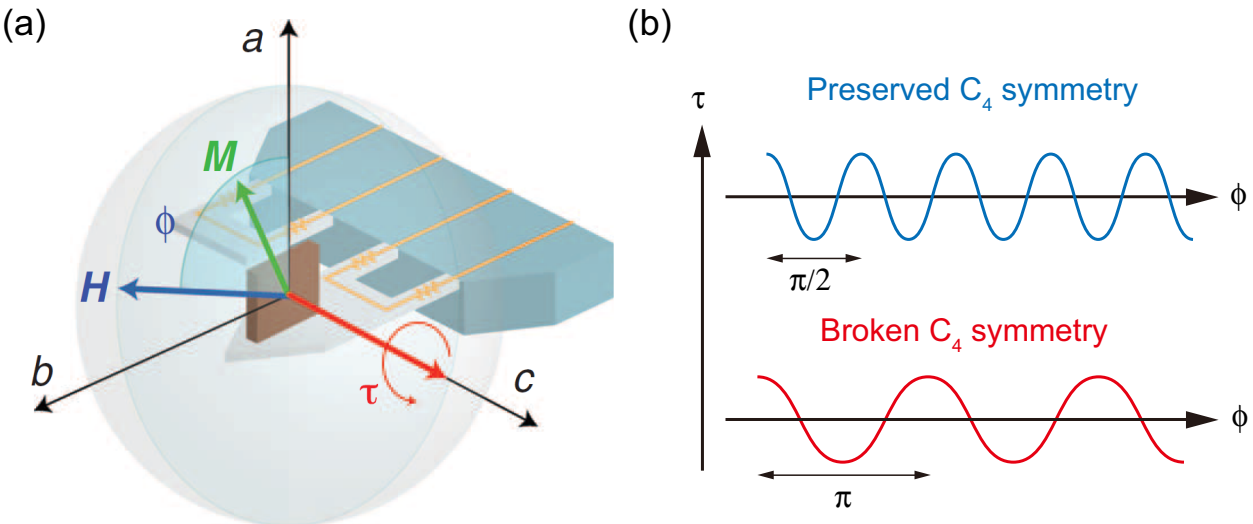

Figure 2.11: (a) A schematic picture of the magnetic torque system. (b) Expected magnetic torque signal [27].

Figure 2.12 shows the temperature evolution of the in-plane torque $\tau(\phi)$ at $\mu_0|H| = 4\,\mathrm{T}$ in the paramagnetic and the hidden-order phases. The raw torque curves are shown in the upper panels of Fig. 2.12 and the two-fold and four-fold components obtained from Fourier analysis are displayed in the middle and lower panels of Fig. 2.12. These results indicate that the two-fold oscillation, which should be zero in a crystal with tetragonal symmetry, emerges below $T_{\mathrm{HO}} = 17.5\,\mathrm{K}$. The two-fold component is expressed as

$$\tau_{2\phi} = \frac{1}{2}\mu_0 H^2 V[(\chi_{aa} - \chi_{bb})\sin 2\phi - 2\chi_{ab}\cos 2\phi], \tag{2.5}$$

where the susceptibility tensor χ_{ij} is given by $M_i = \Sigma_j \chi_{ij} H_j$. The presence of the two-fold oscillation, which follows the functional form $\tau_{2\phi} = A_{2\phi}\cos 2\phi$, clearly demonstrates that $\chi_{ab} \neq 0$, whereas $\chi_{aa} = \chi_{bb}$. This indicates the intrinsic in-plane anisotropy of the susceptibility:

$$\chi[110] = \chi_{aa} + \chi_{bb} \neq \chi[\bar{1}10] = \chi_{aa} - \chi_{bb} \tag{2.6}$$

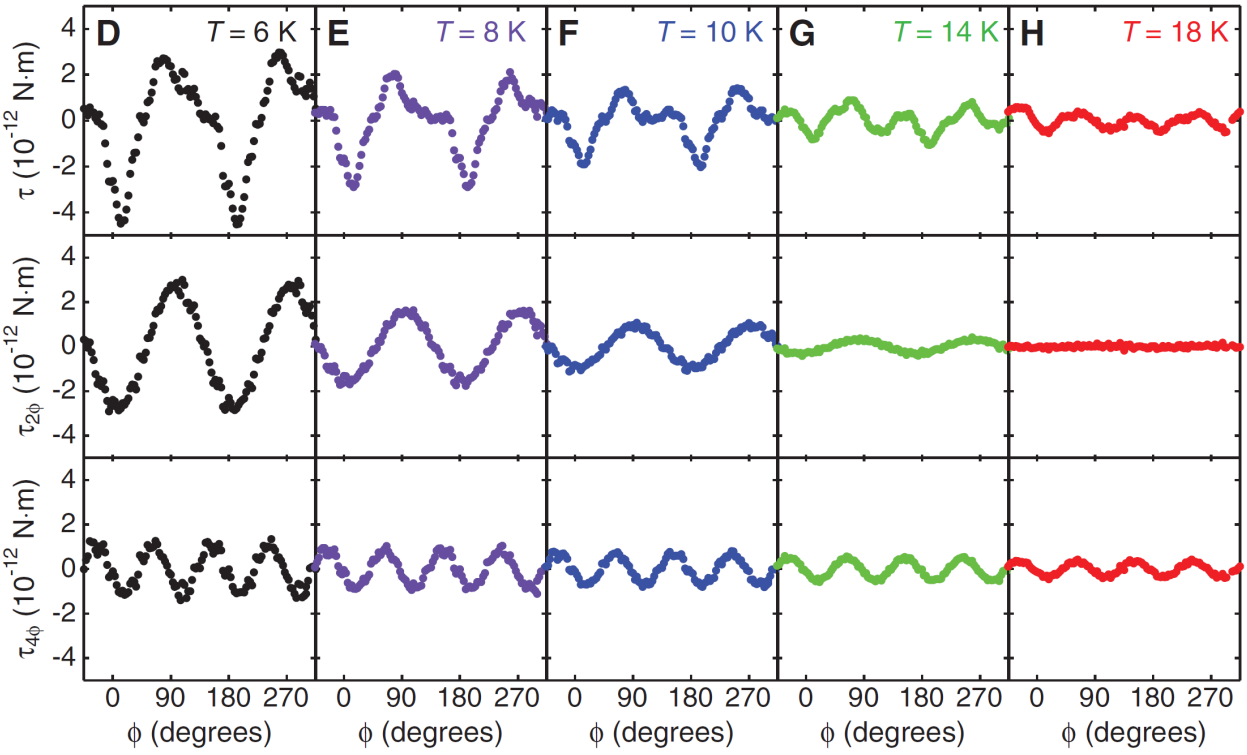

Figure 2.12: In-plane magnetic torque curves measured at $\mu_0|H| = 4$ T. Upper panels show raw torque signals $\tau(\phi)$ as a function of the azimuthal angle ϕ at several temperatures. In the middle and lower panels, the two-fold $\cos 2\phi$ and four-fold $\sin 4\phi$ components of the torque curves are shown, respectively. These curves are obtained from Fourier analysis of the raw torque curves in the upper panels [27].

The results of magnetic torque study is summarized in Fig. 2.13. In the paramagnetic phase of URu_2Si_2, the four-fold rotational symmetry is preserved ($\chi_{aa} = \chi_{bb}$ and $\chi_{ab} = 0$), as shown in Fig. 2.13(b). In the hidden order phase, on the other hand, the four-fold rotational symmetry is broken ($\chi_{aa} = \chi_{bb}$ but $\chi_{ab} \neq 0$).

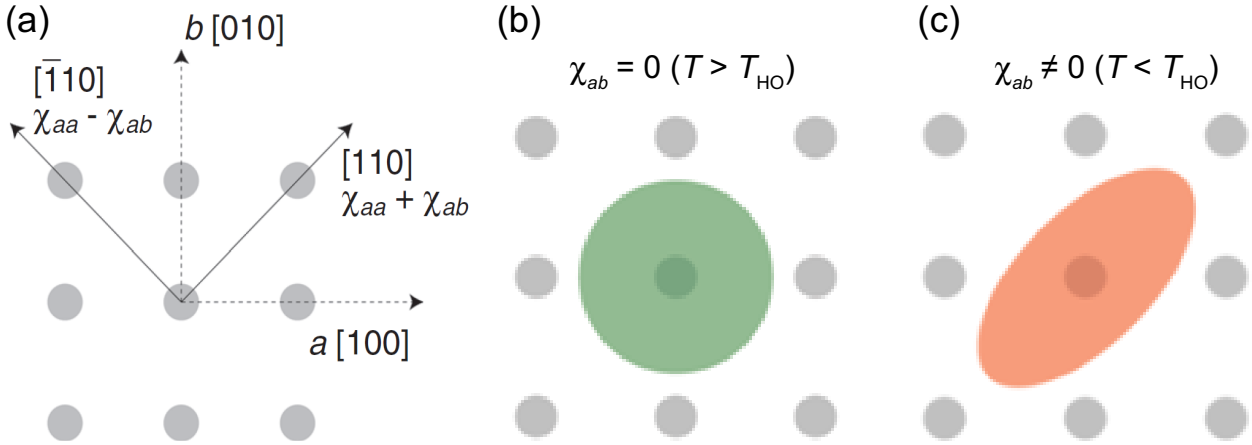

Figure 2.13: (a) Uranium atm arrangement in the [100]-[010] plane of URu_2Si_2. (b) The schematic picture of four-fold rotational symmetry ($\chi_{ab} = 0$). (c) The schematic picture of the two-fold rotational symmetry ($\chi_{ab} \neq 0$) [27].

Figure 2.14 depicts the temperature dependence of the two-fold amplitude for three samples with different sizes. In large millimeter-sized crystals, no difference between $\chi[110]$ and $\chi[\bar{1}10]$, but in samples with a smaller volume, $2\chi_{ab} \propto |A_{2\phi}|/V$ is finite below $T_{HO} = 17.5\,\mathrm{K}$. This indicates that the domains with different preferred directions in the ab plane are formed. From these results, a domain size is estimated the order of tens of micrometers, which signifies the difficulties to observe the in-plane anisotropy.

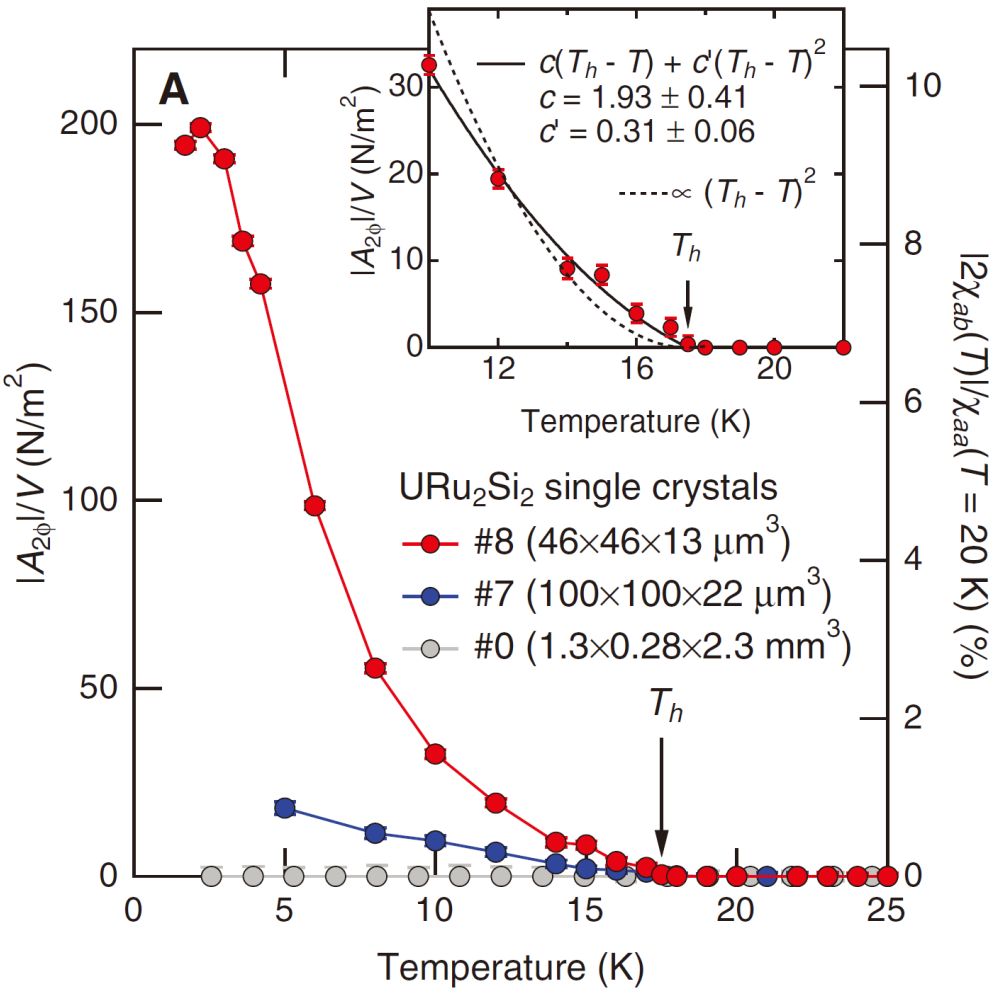

Figure 2.14: Temperature dependence of two-fold oscillation amplitude divided by the sample volume $|A_{2\phi}|/V$. The normalized in-plane susceptibility anisotropy $|2\chi_{ab}(T)|/\chi_{aa}(T = 20\,\mathrm{K}) = (\mathrm{C} - \chi[1\bar{1}0])/\chi[100]$ is evaluated in the right axis [27].

NMR experiments

Recently, the two-fold intrinsic susceptibility anisotropy in the ab plane below $T_{\rm HO}$ was reported by ^{29}Si NMR experiments [28]. In the magnetic torque experiments, the two-fold amplitude of the millimeter-sized sample is absent due to the domain formation. On the other hand, NMR microscopy exploits the magnetic properties at each atomic nuclei, so the signals obtained from domains with different directions are separated from one another. According to the two-fold nematicity proposed by the magnetic torque results, there are two domains with [110] direction and [1$\bar{1}$0] direction (A and B). In such a case, the magnetic susceptibility with in-plane anisotropy reflects the anisotropic ^{29}Si Knight shift K defined as $K(\theta) \equiv (f_{\rm res} - f_0)/f_0$, where $f_{\rm res}$ is the resonance peak frequency and $f_0 \equiv \gamma_{29}H/2\pi$. Expected the angular dependences of the Knight shifts of domain A and B are expressed by,

$$\begin{aligned} K_A(\theta) &= K_{\parallel}\cos^2\theta + K_{\perp}\sin^2\theta = K_{\rm iso} - \frac{1}{2}\Delta K_{\rm nem}, \\ K_B(\theta) &= K_A(\theta + \frac{\pi}{2}) = K_{\rm iso} + \frac{1}{2}\Delta K_{\rm nem}, \end{aligned} \tag{2.7}$$

where $K_{\rm iso} \equiv (1/2)(K_{\parallel} + K_{\perp})$ is the isotropic shift, $K_{\parallel,\perp}$ is the Knight shift for the domain parallel and perpendicular to the magnetic field, and $\Delta K_{\rm nem} \equiv K_{\perp} - K_{\parallel}$ is the anisotropic shift (Fig. 2.15(b)).

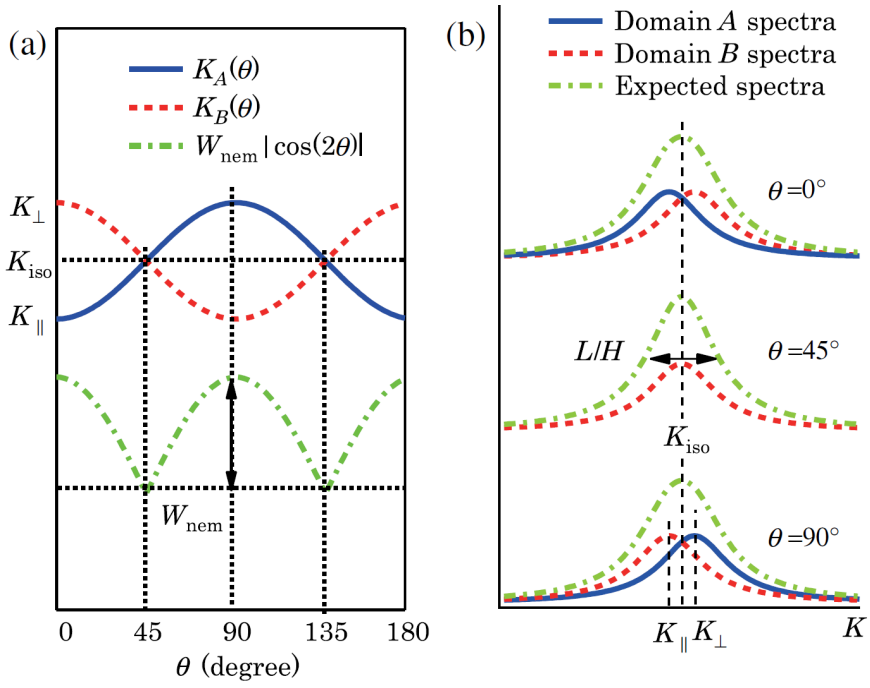

Figure 2.15: (a) The angular dependence of Knight shifts $K_A(\theta)$ and $K_B(\theta)$. (b) Angular dependence expected for ^{29}Si NMR line broadening in the two-fold ordered domain state. Solid lines and broken lines represent spectra for domains A and B, respectively [28].

In the two-fold domain state, the NMR linewidth at half maximum (FWHM) $L_{\rm nem}(\theta)$ is given by

$$L_{\rm nem}(\theta) = H\Delta K_{\rm nem}|\cos(2\theta)| + L_{\rm para}(\theta) + \text{const.}, \tag{2.8}$$

where $L_{\rm para}(\theta)$ has the four-fold symmetry reflected the tetragonal crystal structure. Assuming the nematic component $\Delta K_{\rm nem}$ is finite, the angular dependence of the linewidth exhibits a characteristic sharp minimum (Fig. 2.15(a)).

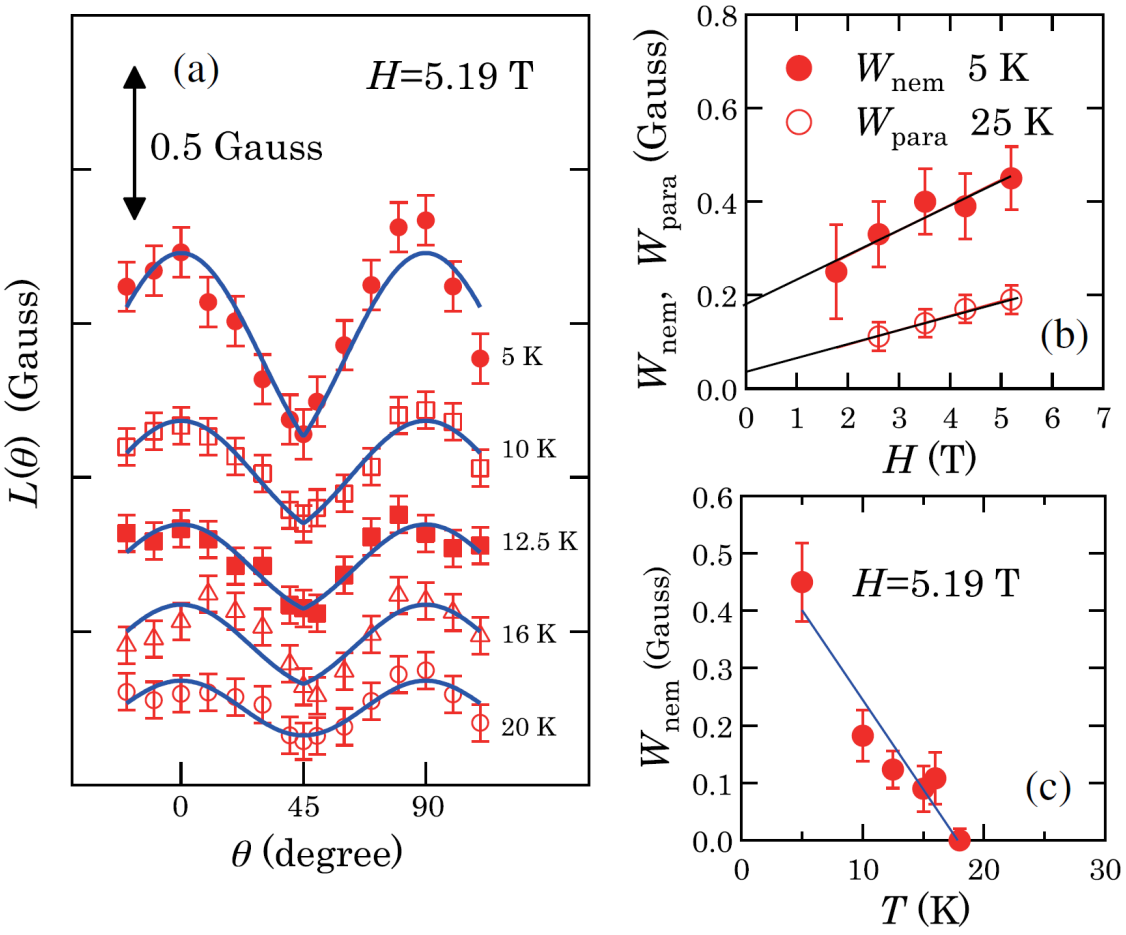

Figure 2.16: (a) Angle dependence of fitted Lorentzian linewidths $L(\theta)$ and calculated results. (b) Field dependence of the four-fold amplitude $W_{\rm para}$ at 25 K and two-fold amplitude $W_{\rm nem}$ at 5 K. (c) Temperature dependence of $W_{\rm nem}$ [28].

The ^{29}Si linewidth at $H = 5.19\,\mathrm{T}$ is displayed in the Fig. 2.16. In the paramagnetic state, $L(\theta)$ presents a small four-fold oscillation expected from the tetragonal crystal structure. Below $T_{\rm HO} = 17.5\,\mathrm{K}$, the oscillation amplitude increases and the two-fold amplitude $W_{\rm nem} = H\Delta K_{\rm nem}$ becomes finite (Fig. 2.16 (c)). Moreover, the peak at $\theta = 45°$ forms a cusp-like structure at low temperature. These results show the proposed nematically ordered domain state where two domains with [110] direction and [1$\bar{1}$0] direction are formed in the URu_2Si_2 sample below the hidden order transition.

2.4 Proposed theory in the hidden order phase

To clarify the order parameter of the hidden order phase, a large number of microscope scenarios have been theoretically proposed, but it still remains controversial. These theories can be roughly divided into three groups, in which th $5f$ electrons are considered to be localized [39–49, 57, 58, 62–64], itinerant [35, 50, 52–54, 59–61, 65–67], or both simultaneously (dual model) [51,55,56]. Table 2.3 shows various theoretical models proposed for the hidden order phase. Nevertheless, the origin of the phase transition at T_0 in URu_2Si_2 is still puzzling and the nature of hidden order phase has became a issue of great interest in heavy-fermion physics.

Table 2.3: Various theoretical models proposed for the hidden order phase in URu_2Si_2.

		references
Multipole	quadrupole	[39–42]
	octupole	[43–46]
	hexadecapole	[47–49, 62]
	dotriacontapole	[35, 50]
Spin density waves	SDW	[51]
	unconventional SDW	[52]
	d-density wave	[53]
	dynamical order	[54]
Others	Duality	[55, 56]
	Mixed valence	[57]
	2-channnel Kondo	[58]
	Orbital anitiferromagnetism	[59]
	Helicity order	[60]
	Hybridization wave	[61]
	Modulated spin liquid	[62]
	Nematic/hastatic model	[35, 44, 63–67]
	...	

2.5 Unconventional superconductivity in URu_2Si_2

Another important aspect of URu_2Si_2 is that the hidden order phase hosts the unconventional superconducting (SC) phase below transition temperature $T_{SC} = 1.4\,K$.

2.5.1 Superconducting gap structure

An important question about the superconductivity of URu_2Si_2 is the nature of the microscopic pairing interaction responsible for the superconductivity. In order to clarify the pairing mechanism, the identification of the symmetry of the superconducting order parameter is of primary importance. Several measurements including NMR [68,69] and the specific heat [70] and the thermal conductivity [29] have revealed that the superconducting gap function of URu_2Si_2 is anisotropic.

NMR experiments

Figure 2.17 shows (a) the NMR relaxation rate$1/T_1$ of ^{29}Si and (b) the NQR relaxation rate of $1/T_1$ ^{101}Ru [68, 69]. These results indicate T^3-dependence down to $T/T_{SC} \simeq 0.2$ without the Hebel-Slichter coherence peak immediately below T_{SC}, suggesting the existence of line nodes in the gap function.

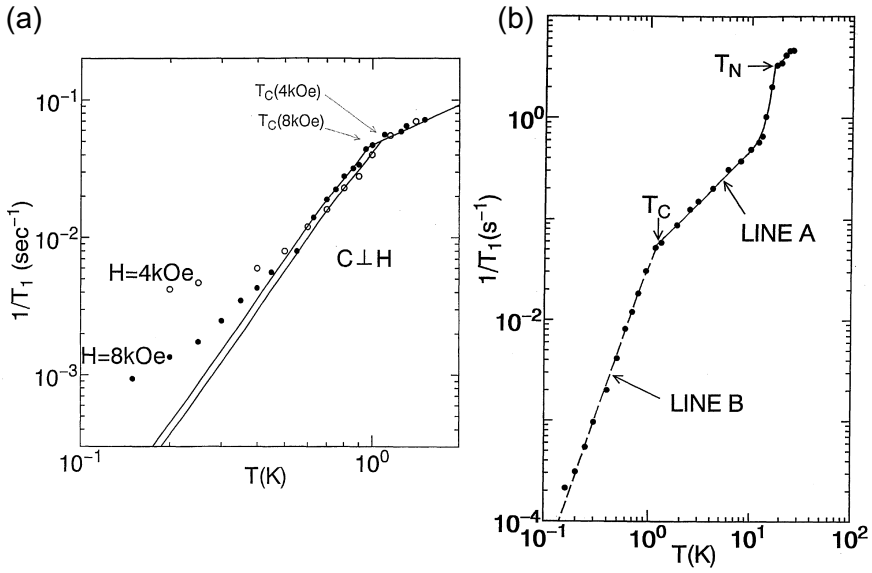

Figure 2.17: (a) Temperature dependence of $1/T_1$ of ^{29}Si obtained by ^{29}Si NMR [68]. (b) Temperature dependence of $1/T_1$ of ^{101}Ru obtained by ^{101}Ru NMR [69].

Specific heat experiments

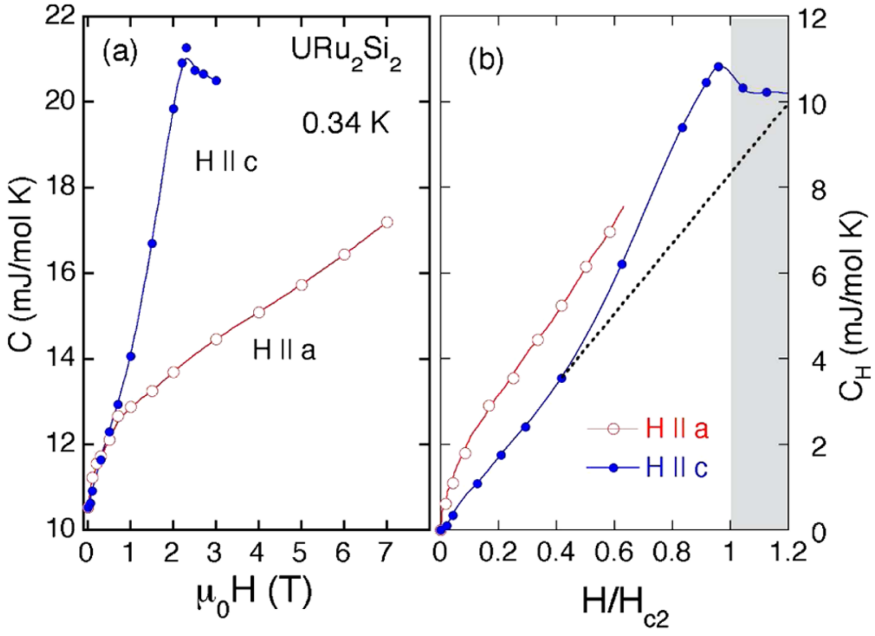

Figure 2.18: (a) Field dependence of the specific heat $C(H)$ of URu_2Si_2 at T =0.34 K for $H \parallel a$ and $H \parallel c$. (b) The specific heat $C(H)$ as a function of the normalized field H/H_{c2} [70].

The specific heat, which is a bulk probe sensitive to the low-energy quasiparticle excitations, yields useful information on the superconducting gap structure. In the superconducting state, the specific heat detects all quasiparticle states. Therefore, in the full gap superconductors, the localized quasiparticle states bound in the vortex cores can contribute to the specific heat, which exhibits H-linear dependence. In nodal superconductors, the specific heat contains contributions from both localized and delocalized quasiparticles, and shows $\sqrt{H}$-dependence because of the dominance of the contribution from the delocalized quasiparticle state.

Figure 2.18 (a) displays the field dependence of the specific heat $C(H)$ of URu_2Si_2 at T =0.34 K for $H \parallel a$ and $H \parallel c$ [70]. $C(H)$ for $H \parallel c$ has a peak structure at H_{c2}^{c} ($\sim$ 2.5 T) and reaches the normal-state value at higher H. $C(H)$ for $H \parallel a$ continues to increase at 7 T because H_{c2}^{a} ($\sim$ 12.5 T) is much higher in this direction. Figure 2.18 (b) shows the specific heat $C(H)$ as a function of the normalized field H/H_{c2}. At low H, $C(H)$ for $H \parallel c$ shows a linear field dependence, suggesting a full gap structure. On the other hand, $C(H)$ for $H \parallel a$ shows the rapid increase, indicating a nodal gap structure. This distinctive $C(H)$ behavior for two directions is consistent with the gap structure with the point nodes locating at the north and south poles on the Fermi surface.

Thermal conductivity experiments

The thermal conductivity, which is a bulk probe sensitive to the low-energy quasiparticle excitations, also yields valuable information on the superconducting gap structure. The localized quasiparticles cannot contribute to the heat transport, in contrast to the specific heat. Therefore, the thermal conductivity can probe the response purely originating from the delocalized quasiparticles, which directly reflects the Doppler shifted density of states. As a result, in the full-gap superconductors, the thermal conductivity is almost zero and it exhibits an exponential behavior at low fields. In a d-wave superconductor with line nodes where the density of states has a linear energy dependence $N(E) \propto |E|$, $N(H)$ increases steeply in proportion to $H^{1/2}$ because of the Doppler shift of the quasiparticle energy, which leads to a $H^{1/2}$ dependence of κ/T.

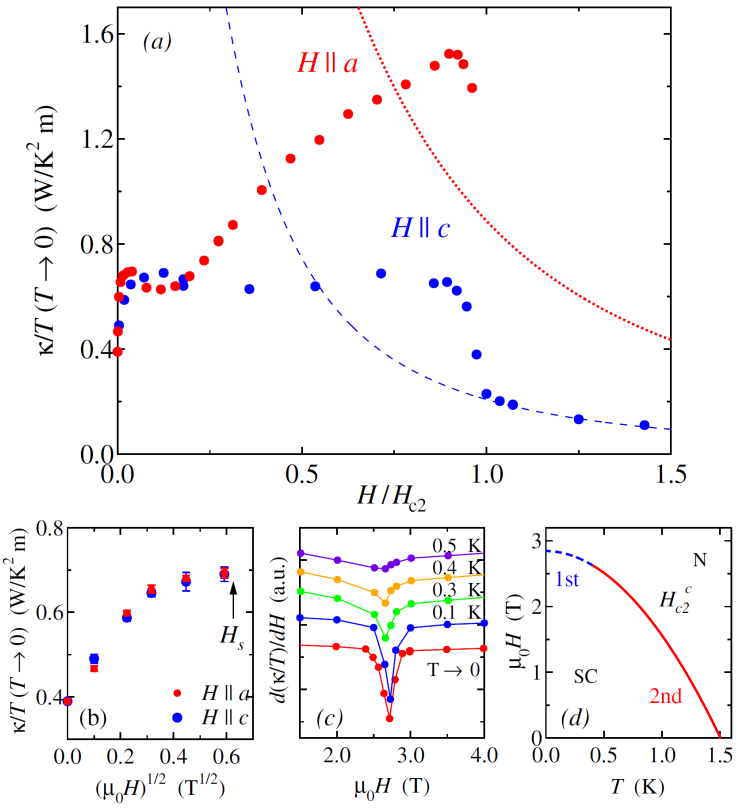

Figure 2.19: (a) The thermal conductivity divided by temperature $\kappa/T(T \to 0)$ as a function of H/H_{c2}. The dashed and dotted lines represent the expected κ/T by the Wiedemann-Franz law for $H \parallel c$ and $H \parallel a$, respectively. (b) κ/T as function of $\sqrt{H}$ at low fields. (c) The field derivative of κ/T for $H \parallel c$ plotted as a function of H. (d) $H-T$ phase diagram for $H \parallel c$ [29].

Figure 2.19 (a) shows the field dependence of the thermal conductivity $\kappa(H)/T$ at $T \to 0$ K limit [29]. $\kappa(H)/T$ shows anomalous field dependence different from typical s-wave and nodal superconductors for two field directions. The two-fold increase in $\kappa(H)/T$ for $\boldsymbol{H} \parallel a$ with a plateaulike behavior following an initial steep increase is very similar to that of $\kappa(H)/T$ in MgB_2 [71] and $PrOs_4Sb_{12}$ [72], which are well known multiband superconductors having two distinct gap. In the multiband system, it is natural to assume that the smaller (larger) gap, which contributes to the low (high) field part of $\kappa(H)/T$, originates from the hole (electron) band having a light (heavy) effective mass. The end point of the initial steep $H_s \simeq 0.4$ T is regarded as a virtual upper critical field of the light hole band. For both field directions, $\kappa(H)/T$ show $\sqrt{H}$ dependence below H_s in Fig. 2.19 (b) indicates a presence of line nodes in the light hole band.

Above H_s, on the other hand, $\kappa(H)/T$ is highly anisotropic. For $\boldsymbol{H} \parallel a$, exhibits a steep increase with increasing H, which is implies the presence of the Doppler shifted the density of states due to nodes. For $\boldsymbol{H} \parallel c$, on the other hand, $\kappa(H)/T$ is almost flat up to H_{c2}, indicating that the quasiparticle excitation is negligibly small. This anisotropic excitation behaviors above H_s strongly suggest the presence of point nodes along the c axis in the heavy electron band.

Consequently, thermal conductivity measurements indicate that nodal topologies in the SC gap of the spherical light hole and the elliptical heavy electron band are line and point nodes, respectively. From the symmetry analysis, the superconducting paring function is most likely to be a "chiral" d-wave symmetry with the superconducting gap function given by

$$\Delta = \Delta_0 \sin\frac{k_z}{2}c\left(\sin\frac{k_x+k_y}{2}a + i\sin\frac{k_x-k_y}{2}a\right). \tag{2.9}$$

The NMR and specific heat experiments are consistent with this gap symmetry.

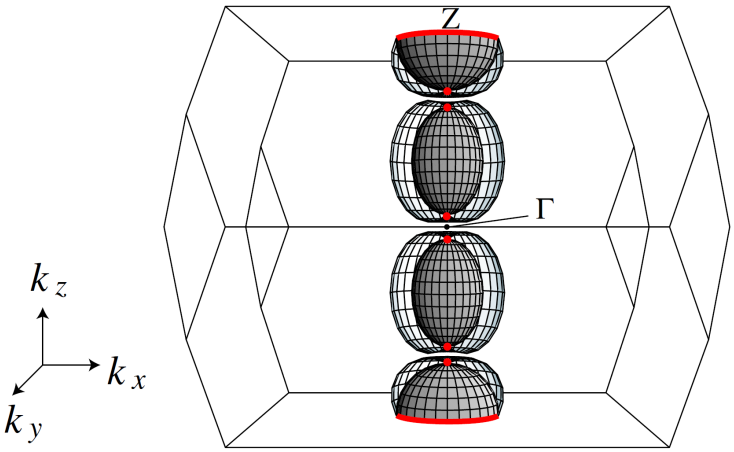

Figure 2.20: The schematic figure of the Fermi surface and superconducting gap structure inferred from thermal conductivity measurements. Thick points and lines at the Fermi surface denote the nodal part [29].

2.5.2 Voltex lattice melting transition

In conventional type II superconductors, Abrikosov vortex lattice is formed in the mixed state. On the other hand, in high-T_{SC} superconductors various vortex phases, such as a vortex-glass, a vortex-liquid have been observed by many experimental work. In the vortex liquid state, Abrikosov lattice with periodic pinning arrays for a system melts due to the thermal fluctuation, namely the thermal displacement of the vortices is an appreciable fraction of the distance between vortices. However, despite low T_{SC} superconductor, the giant thermal fluctuation, which is due to a very small number of carriers and heavy mass, is shown in URu_2Si_2 [73].

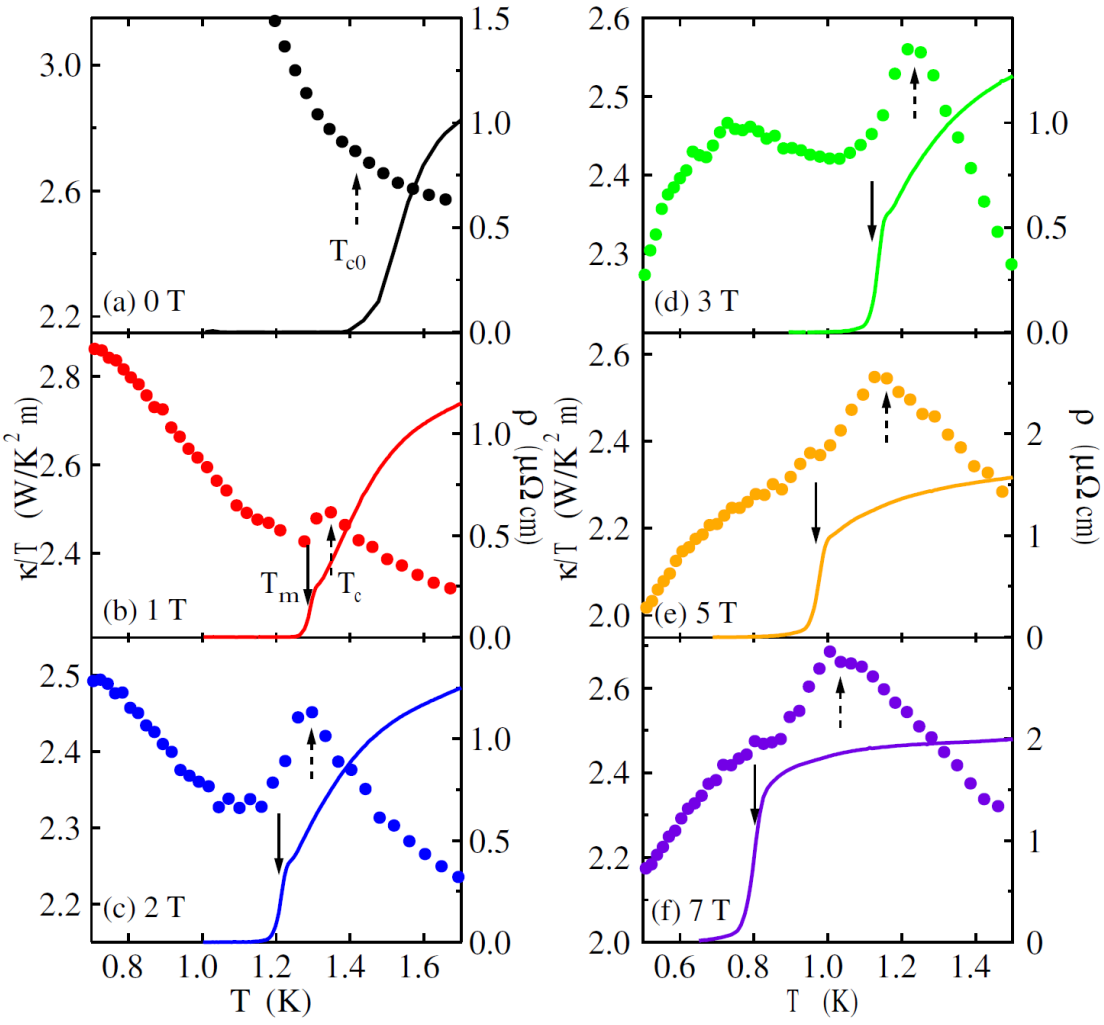

Figure 2.21: Temperature dependence of κ/T (left axis) and ρ (right axis) measured in several magnetic fields for $H \parallel a$. The dotted arrow indicates a cusp at $T_{SC}(H)$. The solid arrows denote the melting temperature T_m [73].

The temperature dependence of the thermal conductivity divided by the temperature κ/T is displayed in Fig. 2.21 [73]. In zero field, κ/T exhibits a notable enhancement below $T_{\rm SC}$. The electronic thermal conductivity is described by $\kappa/T \simeq N(0)v_F l$, where $N(0)$ is quasiparticle density of states, v_F is Fermi velocity and l is mean free path. The enhancement of κ/T below $T_{\rm SC}$ is caused by a striking enhancement of l due to the gap formation, which overcomes the reduction $N(0)$ in the superconducting state. On the other hand, the κ/T behavior begins to decrease with a distinct cusp under a magnetic field as temperature is lowered. According to recent theories, thermal conductivity has no fluctuation correction, in contrast to other transport and thermodynamic properties such as resistivity and specific heat which are subject to the fluctuations. Therefore, it is natural to consider that the cusp temperature of κ/T corresponds to the mean-field transition temperature $T_{\rm SC}(H)$. The decrease of κ/T below $T_{\rm SC}(H)$ immediately indicates that l is not enhanced and the reduction of $N(0)$ becomes dominantly. Further lowering temperature brings a second anomaly below which κ/T increase from that extrapolated from high temperature. This second anomaly is located very close to T_m but far from $T_{\rm SC}$ indicating that the quasiparticle scattering is dramatically changed.

In Fig. 2.21, $\rho(T)$ shows only a gradual decrease near $T_{\rm SC}(H)$ and a sudden drop at T_m. The difference between $T_{\rm SC}(H)$ and $T_m(H)$ becomes more pronounced at higher fields. Here, the feature of the resistive transition in clean $YBa_2Cu_3O_7$, where the sharp drop of the resistivity is observed in a linear scale at the melting temperature without clear anomaly at $T_{\rm SC}(H)$. These results indicate that the vortex lattice melting transition takes place at T_m in URu_2Si_2.

The H-T phase diagram is shown in Fig. 2.22 [73]. The open symbols denote the mean-field H_{c2} lines and the solid square shows the melting transition temperature T_m determined by the clear peak of $d\rho/dT$. The most remarkable feature in this phase diagram is that the melting transition occurs even at very low temperatures and the vortex liquid phase occupies a large portion of the phase diagram compared to conventional low-$T_{\rm SC}$ superconductors. The fundamental parameter that governs the strength of thermal fluctuation is known as the Ginzburg number G_i,

$$G_i = \frac{1}{2}\left(\frac{\epsilon k_B T_{\rm SC}}{H_c(0)^2 \xi_a(0)^3}\right)^2 = \frac{1}{2}\left(\frac{8\pi^2 \epsilon k_B T_{\rm SC} \lambda_a(0)^2}{\phi_0^2 \xi_a(0)}\right)^2 \sim 3\times 10^{-4}, \tag{2.10}$$

where $\lambda_a(0)$ and $\xi_a(0)$ are penetration and coherence lengths in the basal plane at $T = 0$ K and $\epsilon \equiv (m_c/m_{ab})^{1/2}$ is the anisotropy parameter [74]. Using Ginzburg number,the melting temperature is calculated by Larkin and Varlamov [75]. They determined T_m by the equality of the free energies of lattice and liquid phases as

$$T_m - T_{\rm SC}(H) = 2y\left(\frac{H}{H_{c2}(0)}\right)^{2/3}\left(\frac{G_i}{\epsilon^2}\right)^{1/3} T_{\rm SC}(H), \tag{2.11}$$

where $y \sim -7$ for the 3D case and $y \sim -10$ for the 2D case.

In conventional low-T_{SC} superconductors, G_i ranges from 10^{-11} to 10^{-7}, while in $YBa_2Cu_3O_7$ G_i is as large as $\sim 10^{-2}$ [74]. Large G_i leads to the reduction of T_m, extending a vortex liquid region. These results indicate that the exceptionally large thermal fluctuations due to unique electronic state, i.e. very small number of carriers with large effective mass in URu_2Si_2, play an important role even at very low temperatures.

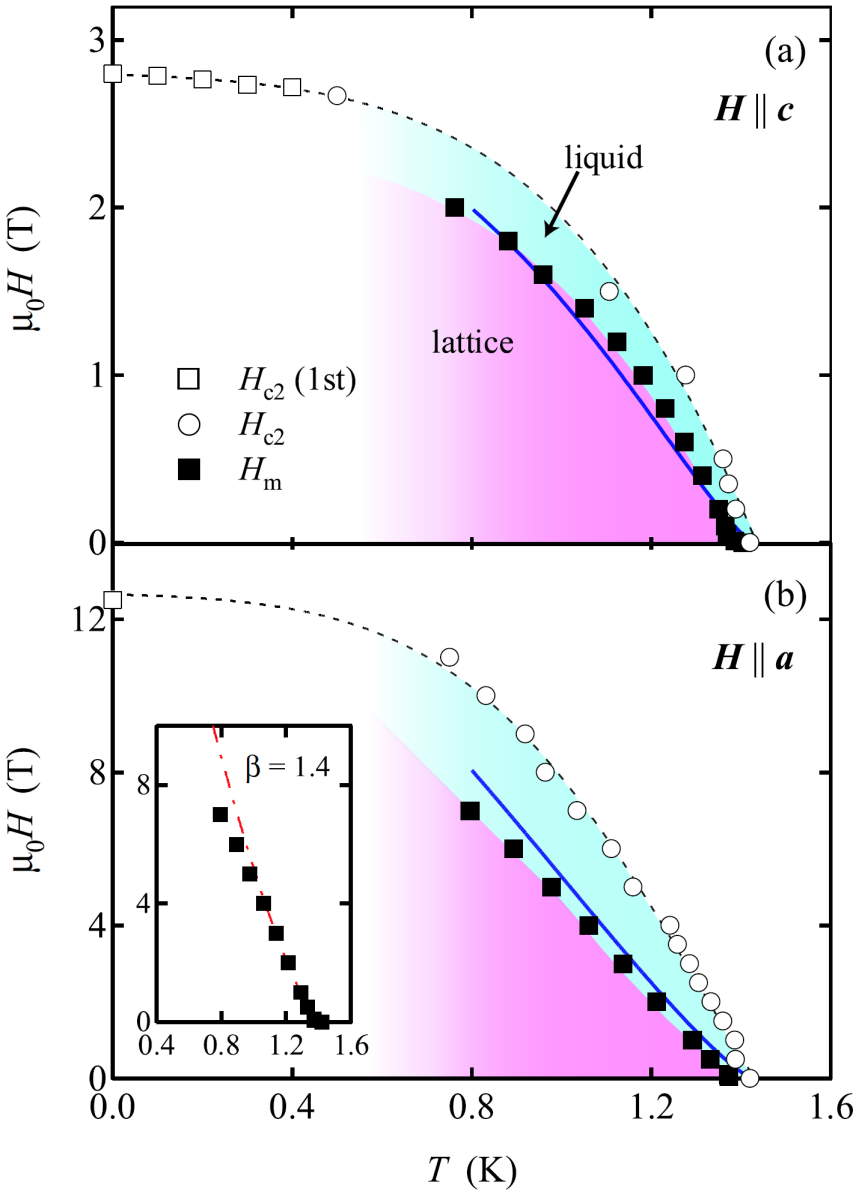

Figure 2.22: H-T phase diagram of URu_2Si_2 for (a) $H \parallel c$ and (b) $H \parallel a$. The inset of (b) shows an expanded view of $H_m(T)$ near $T_{SC}(0)$ for $H \parallel a$. The dash-dotted line is a fit to $H_m(T) \propto (T_{SC} - T)^{\beta}$ with $\beta = 1.4$ which is consistent with that in $YBa_2Cu_3O_7$ [73].

2.5.3 dHvA in superconducting state

Abrikosov vortex lattice below the mean field H_{c2}, dramatically enhance the scattering of quasiparticles by the fluctuating pair potential, thus leading to damping of the dHvA oscillations in the liquid mixed state. However, the dHvA oscillations have been reported even in the SC mixed state for $NbSe_2$ and the high-T_{SC} cuprates $YBa_2Cu_3O_{7-\delta}$ [76] and the f electron superconductors $CeRu_2$ [77] and UPd_2Al_3 [78] *etc.*

Fig. 2.23(a) shows the quantum oscillation in the mixed state for URu_2Si_2 at $T = 35$ mK [33]. The only observed branch α of the dHvA frequency does not change in magnitude between the HO and SC state. On the other hand, the effective mass decreases and the Dingle time (defined as $T_D = \hbar/2\pi k_B\tau$, where $\hbar$ is Plank constant, k_B is Boltzmann constant and τ is quasiparticle scattering time) increases at the superconducting transition as shown in Fig. 2.23(c),(d) respectively. In Maki's theory [79], the change in the mass and Dingle temperature can be explained by the quasiparticle correlation due to the pair breaking.

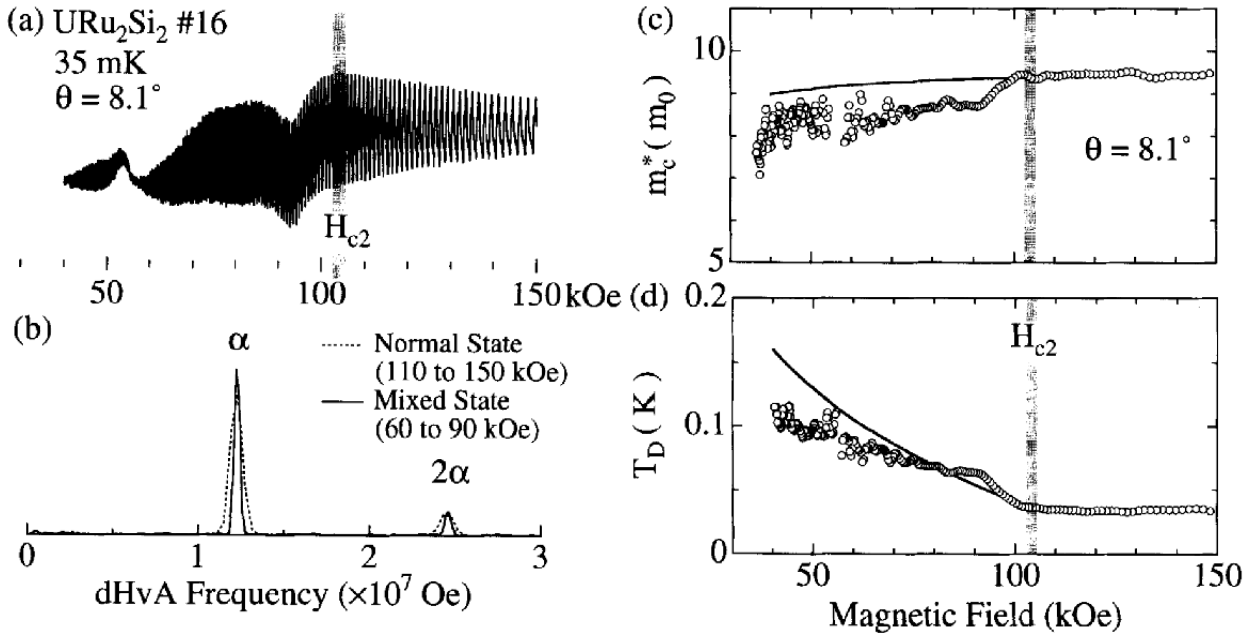

Figure 2.23: dHvA experiments in the mixed state for URu_2Si_2 [33]. (a) dHvA oscillation at 35 mK for $\theta = 8.5°$, where θ is a tilted angle from [100] to [001]. (b) The FFT spectra for branch α in the normal and mixed state. (c) Field dependence of the effective mass. (d) Field dependence of the Dingle temperature.

Chapter 3

Direct observation of lattice symmetry breaking at the hidden-order transition

3.1 Introduction

In this chapter, we show the high resolution X-ray study on the hidden order phase of URu_2Si_2. X-ray diffraction yield a wealth of structural information of a crystal, including atomic arrangement, crystallite size, and imperfections. The X-ray scattering, that is to say, interaction between charge density of electrons in materials and X-ray is explained by Bragg's law. Bragg's law is summarized in the relation $n\lambda = 2d\sin\theta$ where n is an integer, λ is the wavelength of X-ray, d is the interplanar distance, θ is the scattering angle. When a material undergoes a structural change under a condition of temperature change, pressure change, *etc*, the structural symmetry of a material is lowered. As a result of lowering symmetry, the interplanar distance d changes and domains are formed in the material due to the orientation degeneracy of the distortion. This domain formation results in changes in different or new peaks, or Bragg reflections. In this case, observing the appearance of additional peaks and/or shifts of peaks at/to new scattering angles, one realizes a structural change in a material. High resolution X-ray diffraction measurements is one of the most direct ways of observing lattice symmetry breaking.

3.1.1 Bragg equation

We consider a crystal having a set of atomic planes of spacing d and a X-ray wave falling on it, as shown by Fig. 3.1. In view of the assumption of elastic scattering, the wavevector $\boldsymbol{k}_i$ of an incident X-ray and the wavevector $\boldsymbol{k}_f$ of an scattered X-ray will be identical shown by

$$|\boldsymbol{k}_i| = |\boldsymbol{k}_f| = \frac{2\pi}{\lambda}, \tag{3.1}$$

where λ is the wavelength of the X-ray. For the most part, the waves reflected from neighboring planes will cancel each other out due to the phase difference. If, however, the phase difference thorough the all the reflected waves is zero, the maximum constructive interference of the scattered X-ray occurs. To clarify this condition, it is sufficient to consider two microscopic scatterers related by translation through a lattice vector $\boldsymbol{R} = u\boldsymbol{a} + v\boldsymbol{b} + w\boldsymbol{c}$ because of the periodicity of the crystal lattice.

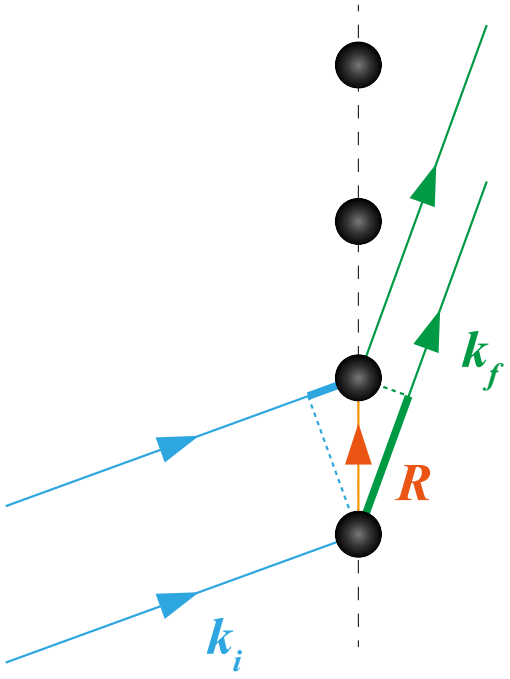

Figure 3.1: A schematic picture of X-ray reflection. The wavevector of the incident beam is $\boldsymbol{k}_i$ and the wavevector of the scattered beam is $\boldsymbol{k}_f$. The atomic length is related by translation vector $\boldsymbol{R} = u\boldsymbol{a} + v\boldsymbol{b} + w\boldsymbol{c}$.

The difference of optical path between the incident and the diffracted beam is given by

$$\begin{aligned} \text{Path difference} &= \boldsymbol{R} \cdot \frac{\boldsymbol{k_f}}{|\boldsymbol{k_f}|} - \boldsymbol{R} \cdot \frac{\boldsymbol{k_i}}{|\boldsymbol{k_i}|} \\ &= \frac{\lambda}{2\pi} \boldsymbol{R} \cdot (\boldsymbol{k_f} - \boldsymbol{k_i}) \\ &= \frac{\lambda}{2\pi} \boldsymbol{R} \cdot \boldsymbol{Q} \end{aligned} \tag{3.2}$$

where $\boldsymbol{Q} \equiv \boldsymbol{k_f} - \boldsymbol{k_i}$ is called the diffraction vector. The maximum constructive interference happens if the difference of optical path is an integer multiple of λ;

$$2\pi n = \boldsymbol{R} \cdot \boldsymbol{Q}, \tag{3.3}$$

where n is integer. This condition can be rewritten as

$$e^{i\boldsymbol{R}\cdot\boldsymbol{Q}} = 1. \tag{3.4}$$

The definition of reciprocal lattice vector $\boldsymbol{g}$ is given by

$$e^{i\boldsymbol{R}\cdot\boldsymbol{g}} = 1 \tag{3.5}$$

$$g = 2\pi h \frac{\boldsymbol{b} \times \boldsymbol{c}}{V} + 2\pi k \frac{\boldsymbol{c} \times \boldsymbol{a}}{V} + 2\pi l \frac{\boldsymbol{a} \times \boldsymbol{b}}{V}, \tag{3.6}$$

where V is the volume of the unit cell and h, k, l are the Miller indices for planes and directions. By comparing between eqn (3.4) and eqn (3.5), we find that the diffraction condition is satisfied when the scattering vector equals a reciprocal lattice vector,

$$\boldsymbol{Q} = \boldsymbol{g}. \tag{3.7}$$

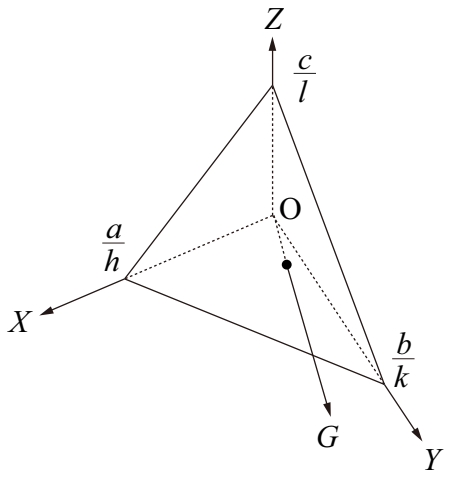

Figure 3.2: The reciprocal lattice vector $\boldsymbol{g}$ and the interplanar distance d.

If we now denote the angle between $\boldsymbol{k_i}$ and $\boldsymbol{k_f}$ by 2θ, and construct the isosceles triangle such that $|\boldsymbol{k_i}| = |\boldsymbol{k_f}|$ and $\boldsymbol{g} = \boldsymbol{k_f} - \boldsymbol{k_i}$, we have

$$\begin{aligned} |\boldsymbol{g}| &= |\boldsymbol{k_f}| \sin\theta + |\boldsymbol{k_i}| \sin\theta \\ &= 2\pi \frac{2\sin\theta}{\lambda}. \end{aligned} \tag{3.8}$$

From the definition of the reciprocal lattice vector $\boldsymbol{g}$, the interplanar distance d is shown by

$$\frac{1}{d} \equiv \frac{|\boldsymbol{g}|}{2\pi} = \sqrt{\left(\frac{h}{a}\right)^2 + \left(\frac{k}{b}\right)^2 + \left(\frac{l}{c}\right)^2}, \tag{3.9}$$

where $|\boldsymbol{a}| = a$, $|\boldsymbol{b}| = b$ and $|\boldsymbol{c}| = c$. From eqns (3.8) and (3.9), we have

$$2d\sin\theta = \lambda. \tag{3.10}$$

If h, k, l are of the form nh', nk', nl', where h', k', l' are relatively prime and $d' = nd$, we have

$$2d'\sin\theta = n\lambda. \tag{3.11}$$

This equation is the original version of the Bragg equation which gives the angles for coherent scattering from a crystal lattice and eqn (3.10) is the version most often encountered in practical applications. In conclusion, the maximum amplitude of the reflected wave is obtained for angles θ such that

$$2\sin\theta = \lambda\sqrt{\left(\frac{h}{a}\right)^2 + \left(\frac{k}{b}\right)^2 + \left(\frac{l}{c}\right)^2}. \tag{3.12}$$

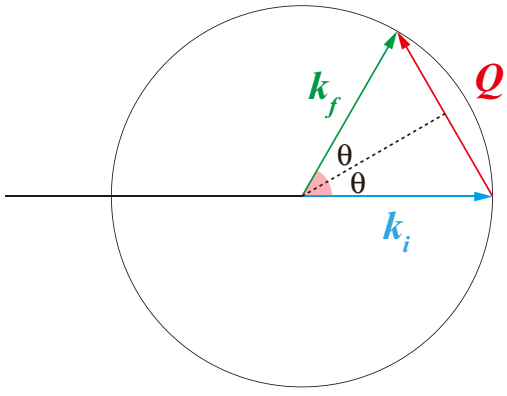

Figure 3.3: Geometrical interpretation of the Bragg equation.

3.1.2 The energy of the X-ray

When an photon has the energy E, the highest frequency or its lowest wavelength is given by

$$E = h\nu_{\max} = \frac{hc}{\lambda_{\min}}, \tag{3.13}$$

where h is Planck's constant, ν is the photon's frequency and λ is the photon's wave length. This also can be rewritten by

$$\lambda\,(\text{Å}) = \frac{hc}{E} = \frac{12.3984}{E\,(\text{keV})}. \tag{3.14}$$

3.1.3 Imaging plate camera

There are various kinds of X-ray detectors. We used the image-plate camera to select the high quality sample and studied whether the lattice distortion occurs in the hidden order state by the four-circle diffractometer. The former is described in this section and the latter is explained in the next section.

The image-plate camera is an wide area detector, qualitatively similar to the photographic film but operating on entirely different principles. When a photon strikes the imaging plate, the "detached" electrons are raised to the conduction band. The excited electrons are trapped at the vacancies of the emulsion coating the imaging plate and thereby produce temporary color centers. Hence, the imaging plate changes color at the sites on which scattered radiation is falling. When the exposure has been completed, the diffraction pattern has been temporarily recorded on the imaging plate. The plate is then scanned by a laser and the trapped electrons are released, fall down to the valence a band. This transition is accompanied by a release of energy, which corresponds to the emission of light. The intensity of this luminescence, measured with a photomultiplier, is proportional to the intensity of the X-rays which gave rise to the color centers. The coordinates of the diffraction spots and the intensity of the luminescence are recorded in a computer. When the scanning process has been completed, the imaging plate is exposed to visible light, which erases all the remaining traces of color centers and the plate is suitable for future use.

The imaging plate camera has a very large linearity range by which you can observe the wide area with high angle 2θ by one scan. Therefore the imaging plate camera is known to a convenient and very fast detector of X-ray diffraction patterns.

3.1.4 Four-circle diffractometer

Geometrical consideration

Different from other area detecotor, the four circle diffractometer allows us to detect a specific Bragg peak. This instrument is equipped with a mechanical system which can bring the sample into an orientation in which the wavevector of the incident X-ray forms the Bragg angle θ with the desired hkl plane, and bring the slit of detector to a proper position to detect the scattered radiation. A schematic drawing of a four-circle diffractometer is shown in Fig. 3.4 [80].

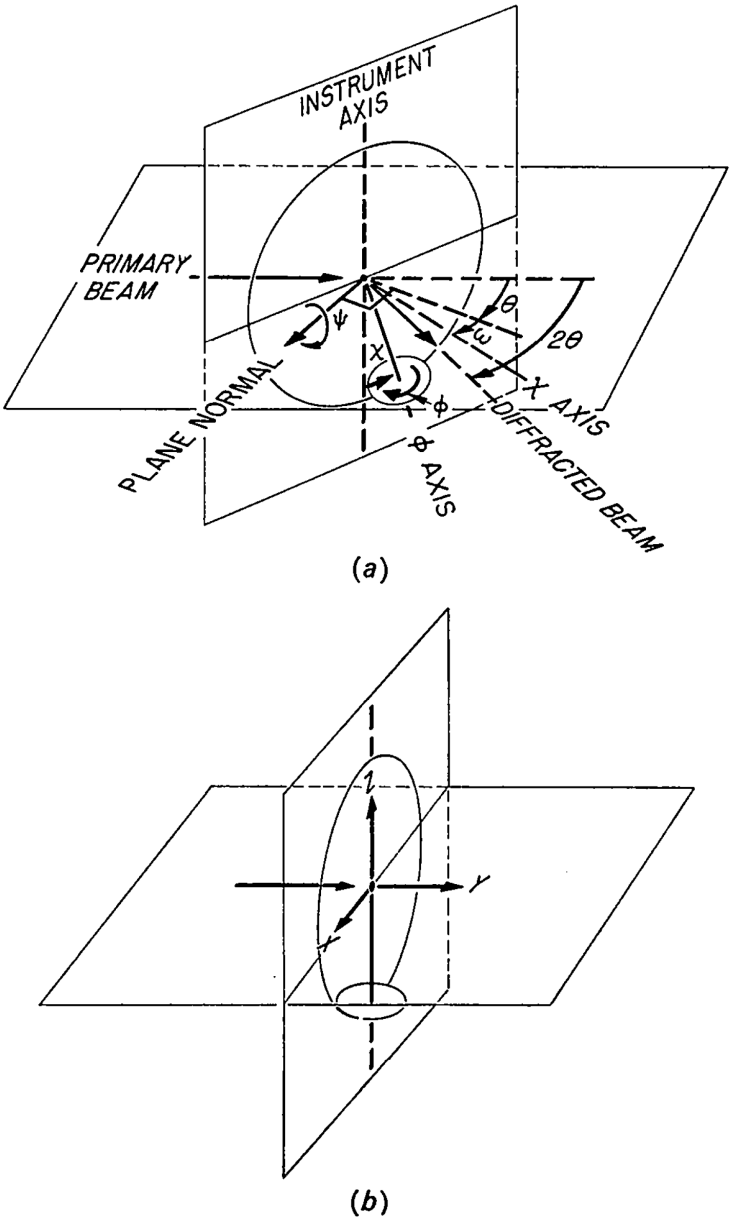

Figure 3.4: A schematic picture of four-circle diffractometer [80].(a) The definition of each axis and angle. (b) The instrument with all angles set to zero.

For the X-ray analysis by four-circle diffractometer, it is the most important to control the geometrical configuration. The diffraction plane is defined by three points: (i) the center of the source of the radiation (I), (ii) the center of the crystal (O), and (iii) the center of the receiving slit of the detector (F). The axis passing through the crystal and perpendicular to the diffraction plane is called the principal axis of the instrument. Its direction remains fixed throughout the experiments, so the detector is constrained to rotate about the principal axis only. The angle IOF equals $180° - 2\theta$, where 2θ is the angle between the incident and the diffracted beam. The diffraction vector corresponding to the Bragg angle θ is parallel to the bisector of the angle IOF. The detail of the other axes of rotation is below.

(A) χ-axis

This is an axis passing through the crystal and lying in the diffraction plane. In a conventional diffractometer, this is the symmetry axis of a ring on whose internal cylindrical surface of the device to which the crystal is rigidly attached can be displaced by a predetermined angle, called the χ angle. The center of the crystal must coincide with the center of the χ ring. The plane of the χ ring is perpendicular to the diffraction plane throughout the experiment.

(B) ϕ-axis

This is an axis about which the crystal, together with the device to which the crystal is rigidly attached, can be rotated through a predetermined angel, called the ϕ angle. During the rotation about ϕ-axis the center of the crystal must remain at the center of the χ ring and the orientation of the axis of rotation of the crystal within the plane of the ring is determined by the χ angle.

(C) Ω-axis

This axis passes through the crystal and through the plane of the χ ring, and is perpendicular to the diffraction plane. By definition, the Ω-axis coincides with the principal axis of the instrument. Physically, however, there are two independent rotations associated with this axis: the Ω motor rotates the χ ring (with everything it carries) and does not affect the position of the detector, and the 2θ motor rotates the detector without affecting the orientation of the crystal with respect to the incident beam.

Geometric coordinate transformation

The equations necessary to calculate the diffractometer setting angles for a expected reflection were presented by Busing and Levy (1967). In a diffraction experiments performed by a four circle diffractometer, the diffraction vector is represented in terms of several sets of basis vectors.

(i) The reciprocal lattice basis.
The reciprocal lattice vector can be written as

$$\boldsymbol{g} = h\boldsymbol{a}^* + k\boldsymbol{b}^* + l\boldsymbol{c}^* \equiv \boldsymbol{h}\boldsymbol{r}^*, \tag{3.15}$$

where $\boldsymbol{h} = (h\ k\ l)$ are Miller indices and $\boldsymbol{r}^* = (\boldsymbol{a}^*\ \boldsymbol{b}^*\ \boldsymbol{c}^*)$ are reciprocal lattice basis vectors.

(ii) The crystal Cartesian basis.
$\boldsymbol{g}_c$ is defined as the description in terms of the crystal Cartesian axes. In this system, if we choose the x axis parallel to $\boldsymbol{a}^*$, the y-axis in the plane of $\boldsymbol{a}^*$ and $\boldsymbol{b}^*$, and the z-axis perpendicular to that plane, then

$$\boldsymbol{g}_c = B\boldsymbol{g} \tag{3.16}$$

where the B matrix is calculated from the unit-cell parameter of the crystal:

$$B = \begin{pmatrix} \boldsymbol{a}^* & \boldsymbol{b}^* \cos\gamma^* & c^* \cos\beta^* \\ 0 & \boldsymbol{b}^* \sin\gamma^* & -c^* \sin\beta^* \cos\alpha \\ 0 & 0 & 1/c \end{pmatrix}. \tag{3.17}$$

Here the a, b, c and α, β, γ are the direct lattice parameters respectively and the asterisked parameters are reciprocal-space quantities. Note that the B matrix depends on the choice of a Cartesian reference system for the unit-cell and the choice is arbitrary.

(iii) The ϕ-axis Cartesian coordinate system.
The U matrix defines the orientation of the crystal axes with respect to the ϕ-axis Cartesian coordinate system so that

$$\boldsymbol{g}_\phi = U\boldsymbol{g}_c. \tag{3.18}$$

U depends on the way in which the crystal has been mounted on the goniometer head. If we define that the basis vectors $\boldsymbol{e}_\phi = (\boldsymbol{e}_{1\phi}\, \boldsymbol{e}_{2\phi}\, \boldsymbol{e}_{3\phi})$ form a right-handed set of orthonormal unit vectors, the vector $\boldsymbol{e}_{3\phi}$ coincides with the ϕ axis (the axis about which the goniometer head rotates).

(iv) The 2θ-axis Cartesian coordinate system.
An orthonormal basis attached to the diffraction vector and the diffractometer. Such a basis is needed for the construction of the laboratory working system. Here, the basis vectors

$\boldsymbol{e}_\theta = (\boldsymbol{e}_{1\theta}\, \boldsymbol{e}_{2\theta}\, \boldsymbol{e}_{3\theta})$ form a right-handed set of orthonormal unit vectors. The vector $\boldsymbol{e}_{2\theta}$ is parallel to the diffraction vector and therefore bisects the complementary angle $180° - 2\theta$ between the incident and diffracted beams. The vector $\boldsymbol{e}_{1\theta}$ lies in the diffraction plane, is perpendicular to $\boldsymbol{e}_{2\theta}$ and points to the source of radiation when $\theta = 0$. The vector $\boldsymbol{e}_{3\theta}$ coincides with the principal axis of the instrument and is directed so as to make the system of basis vectors right handed. For any values of the angles χ, ϕ and Ω, the 2θ-axis and ϕ-axis Cartesian coordinate system are related by a rotation matrix depending on these three angles. This rotation matrix is obtained as a product of three rotation matrices about the corresponding axes as shown by

$$\boldsymbol{g}_\theta = R\boldsymbol{g}_\phi \tag{3.19}$$

$$\begin{aligned} R &= \boldsymbol{\Phi\chi\Omega} \\ &= \begin{pmatrix} \cos\phi & \sin\phi & 0 \\ -\sin\phi & \cos\phi & 0 \\ 0 & 0 & 0 \end{pmatrix} \begin{pmatrix} 1 & 0 & 0 \\ 0 & \cos\chi & \sin\chi \\ 0 & -\sin\chi & \cos\chi \end{pmatrix} \begin{pmatrix} \cos\Omega & \sin\Omega & 0 \\ -\sin\Omega & \cos\Omega & 0 \\ 0 & 0 & 0 \end{pmatrix} \\ &= \begin{pmatrix} \cos\phi\cos\Omega - \sin\phi\sin\Omega\cos\chi & \cos\phi\sin\Omega - \sin\phi\cos\Omega\cos\chi & \sin\phi\sin\chi \\ -\sin\phi\cos\Omega - \cos\phi\sin\Omega\cos\chi & -\sin\phi\sin\omega + \cos\phi\cos\Omega\cos\chi & \cos\phi\sin\chi \\ \sin\chi\sin\Omega & -\sin\chi\cos\Omega & \cos\chi \end{pmatrix} \end{aligned} \tag{3.20}$$

Note that when $\chi = \phi = \Omega = 0$, $\boldsymbol{g}_\theta = \boldsymbol{g}_\phi$.

Basic diffractometer equations

To observe a reflection in the ideal diffractometer setting it is necessary for θ to satisfy the Bragg equation and for the plane normal to lie along the y-axis of the 2θ-axis coordinate system. If h, k, and l are the indices of the reflecting plane then the corresponding column vector in the reciprocal lattice system is

$$\boldsymbol{h} = \begin{pmatrix} h \\ k \\ l \end{pmatrix} \tag{3.21}$$

The length q of this vector which is the reciprocal of the interplanar spacing is readily found from its components in any one of our Cartesian systems. The plane normal will have the desired direction if

$$\boldsymbol{h}_\theta = RUB\boldsymbol{h} \tag{3.22}$$

has the form

$$\boldsymbol{h}_\theta = \begin{pmatrix} 0 \\ q \\ 0 \end{pmatrix}. \tag{3.23}$$

The Bragg equation is then

$$2\sin\theta = \lambda q \tag{3.24}$$

Evaluating the orientation matrix

Angular calculations on a diffractometer use the UB matrix which is called orientation matrix. The UB matrix transforms a set of reflection indices $\boldsymbol{h} = (h\ k\ l)$ to a set of diffractometer coordinates denoted as the vector $\boldsymbol{h}_\phi$. The components of the vector $\boldsymbol{h}_\phi$ contain the positions of the diffractometer axes by which the plane normal $\boldsymbol{h}$ is brought into coincidence with the diffraction vector:

$$\begin{aligned}
\boldsymbol{h}_\phi &= UB\boldsymbol{h} = UB \begin{pmatrix} h \\ k \\ l \end{pmatrix} \\
\boldsymbol{h}_\phi &= R^{-1}\boldsymbol{h}_\theta = R^{-1} \begin{pmatrix} 0 \\ q \\ 0 \end{pmatrix} = \frac{2\sin\theta}{\lambda} \begin{pmatrix} \sin\phi\cos\Omega\cos\chi + \cos\phi\sin\Omega \\ \cos\phi\cos\Omega\cos\chi - \sin\Omega\sin\phi \\ -\sin\phi\cos\Omega \end{pmatrix}
\end{aligned}$$

In principal, we can calculate the orientation matrix from three non-coplanar indices of the Bragg reflection or two Bragg peaks and lattice constant using the below equation,

$$UB \begin{pmatrix} h \\ k \\ l \end{pmatrix} = \frac{2\sin\theta}{\lambda} \begin{pmatrix} \sin\phi\cos\Omega\cos\chi + \cos\phi\sin\Omega \\ \cos\phi\cos\Omega\cos\chi - \sin\Omega\sin\phi \\ -\sin\phi\cos\Omega \end{pmatrix} \tag{3.25}$$

3.2 Purpose of the X-ray study in the hidden order phase

Interactions of electrons in solids can cause a variety of second-order phase transitions, the nature of which is most fundamentally characterised by spontaneous symmetry breaking. Since the 1985 discovery [9–11] of the phase transition at $T_{\mathrm{HO}} = 17.5\,\mathrm{K}$ in a heavy-fermion metal URu_2Si_2, tremendous efforts have been made to understand its properties [81], but the nature of this "hidden order" has been a central enigma in condensed-matter physics. Neither symmetry change in the crystal structure [18, 82, 83] nor magnetic ordering [32, 84, 85] had been clarified experimentally, which leads to dozens of theoretical proposals of different order parameters [81]. Quite recently, rotational symmetry breaking has been newly suggested by several experiments [27, 28, 86, 87], but these measurements have been done under in-plane magnetic fields, which may induce a different order from the original (hidden) order at the ground state. On the other hand, the X-ray experiment provides a stringent test of whether the four-fold symmetry is broken in the hidden order state under no magnetic field. In this study we have performed high-accuracy X-ray experiments by the four-circle diffraction which has specify geometrical setting with the higher resolution than previous experiments.

3.3 Experiments

3.3.1 Samples

High-quality single crystals of URu_2Si_2 were provided by Prof. Yoshinori Haga, Prof. Tatsuma Matsuda, and Prof. Yoshichika Onuki at Advanced Research Center, Japan Atomic Energy Agency (JAEA). The single crystals grown by the Czochralski method in a tetra-arc furnace under argon gas atmosphere and subsequently purified by using the solid state electro-transport method under ultrahigh vacuum [12, 13]. The URu_2Si_2 ingot was also subsequently annealed using the electro-transport method under ultrahigh vacuum. The quality of the sample depends on the position in the ingot.

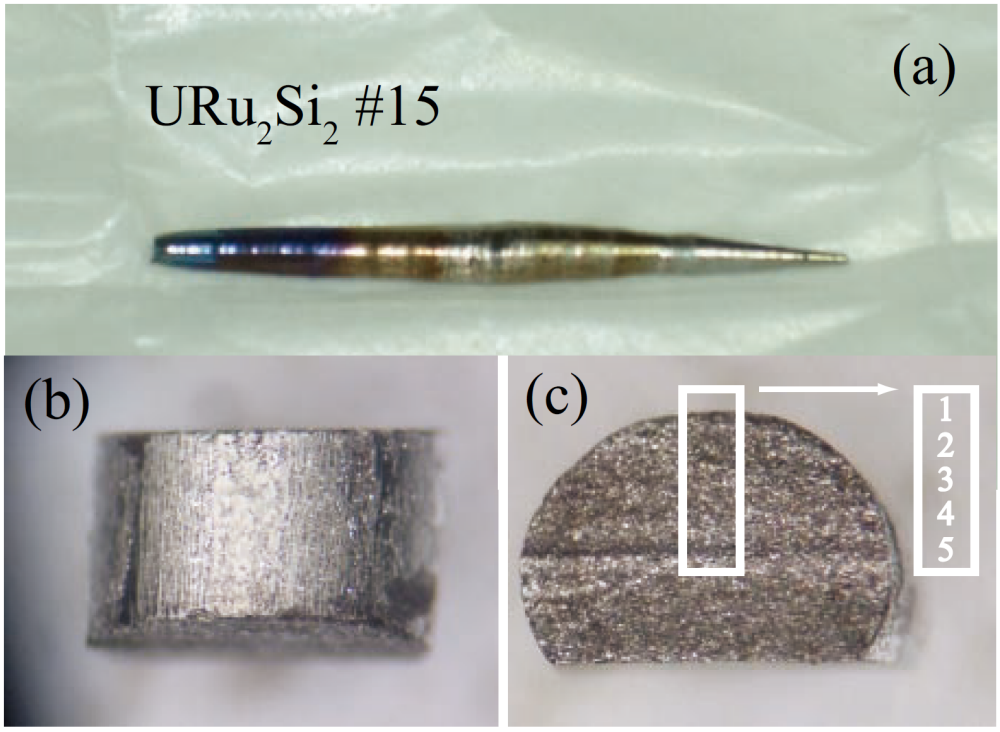

Figure 3.5: (a) URu_2Si_2 ingot annealed using the electro transport method and (b), (c) a part of the ingot [13].

Figure 3.6(a),(b) show the temperature dependence of the electrical resistivity for five samples cut from URu_2Si_2 ingot [13]. The electrical resistivity ρ is normalized by the resistivity at room temperature ρ_{RT}, namely ρ/ρ_{RT}. The resistivity of five kinds of samples behave in similar temperature dependence in the high-temperature region, but low-temperature behavior strongly depends on the position in the ingot. The sample No.1 which is cut from the surface region in the ingot has a very small residual resistivity. The residual resistivity ratio RRR reach up to 1000. The superconducting transition temperature T_{SC} also depends on the the position in the ingot. The highest T_{SC}= 1.45 K is shown by the No.1 sample.

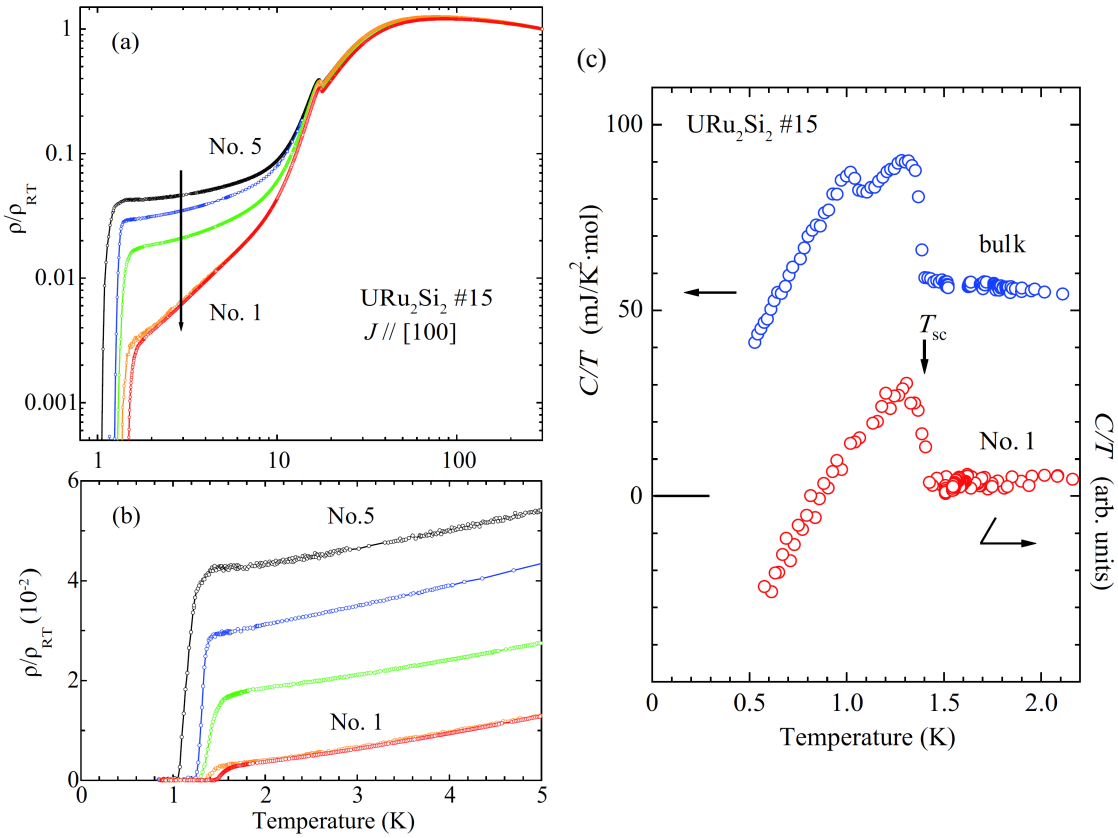

Figure 3.6: (a) Temperature dependence of the electrical resistivity ρ normalized by the value obtained at room temperature ρ_{RT}. (b) Expanded view in the low-temperature region. The five kinds of the sample is cut from the different region of URu_2Si_2 ingot. (c) Temperature dependence of the specific heat C/T. Upper data is a specific heat of single crystal after the annealing before cutting. Lower one is a specific heat of single crystal after taking a small piece of the crystal after taking a small piece of the crystal by cutting the annealed ingot [13].

Figure 3.6(c) shows the temperature dependence of the specific heat C/T measured with the single-crystal ingot named as "bulk"and a No.1 sample [13]. The specific heat of the bulk sample shows the double jump at the superconducting transition, which indicates the bulk sample has inhomogeneity of the sample quality. However, the sample No.1 exhibits a single transition jump at $T_{\mathrm{SC}} = 1.45$ K.

The de Haas-van Alphen(dHvA) measurements were also carried out in the sample No.1. A single oscillation of α branch is observed in the field range from 4.5 to 8 T at 69 mK. The dHvA frequency $F = 1.21 \times 10^7$ Oe coincides with the previous dHvA and SdH results. On the other hand, the Dingle plot analysis show the large scattering time $\tau = 2.4 \times 10^{-14}$. This large τ value is equivalent to the very large mean free path $l = 11000$ Å, which is larger than the previous value of $l = 5500$ Å for the $RRR = 256$ sample. The electrical resistivity, specific heat and dHvA measurements show the sample cut from the surface region in the ingot has high quality.

Sample quality in this study

We use two single crystals from two different batches evaluated by residual resistivity ratios RRR. One is an ordinary crystal with a typical value of $RRR \sim 10$ and the other is a new-generation ultraclean crystal with $RRR \sim 670$. Figure 3.7 shows the temperature dependence of the resistivity ρ along the a-axis in zero magnetic field with $RRR \sim 670$. ρ exhibits a tiny peak following a kink at T_{HO}, as previously reported. A well-defined superconducting transition at $T_{\mathrm{SC}} \sim 1.4$ K was observed, which was confirmed by the specific heat measurements.

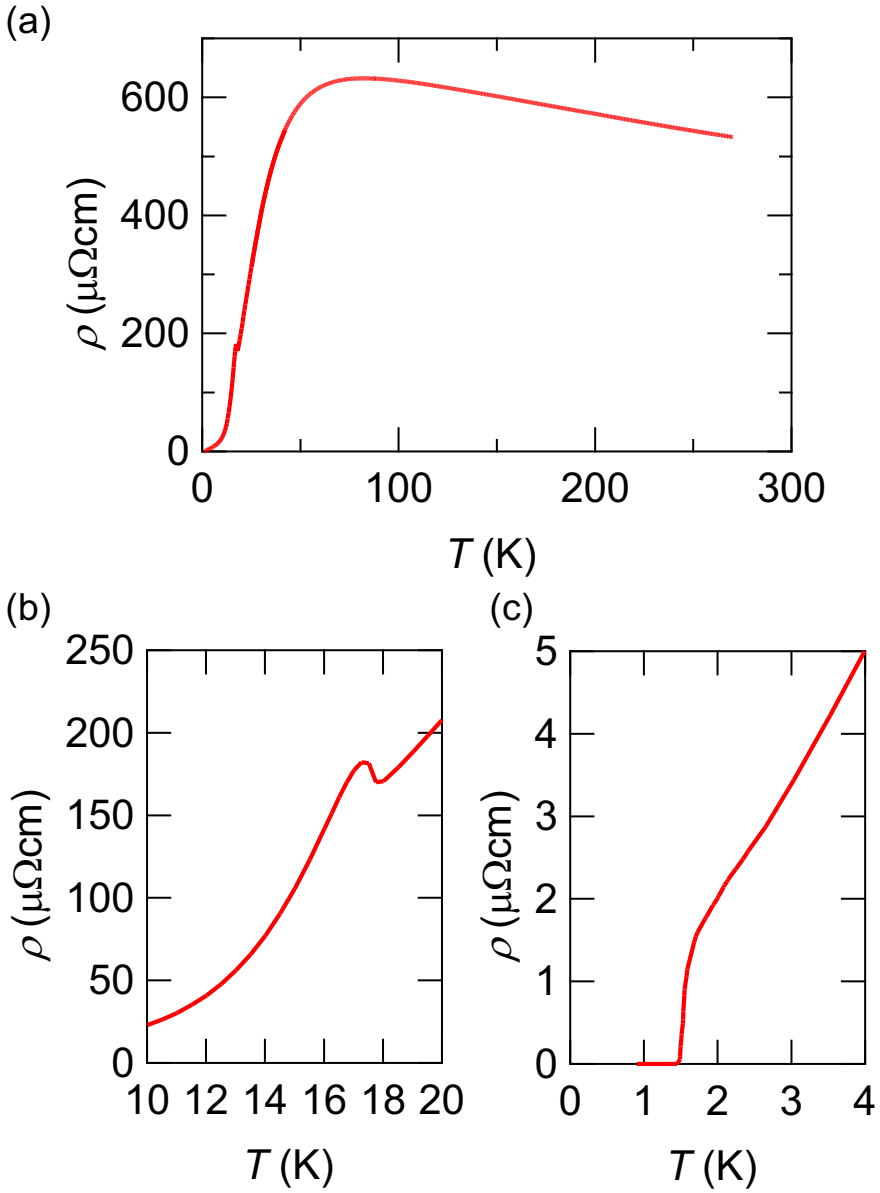

Figure 3.7: (a) Resistivity ρ as a function of T. (b) Expanded view of the resistivity ρ near the hidden order transition. (c) Magnified view of the resistivity ρ near the superconducting transition.

3.3.2 Methods

Guide for higher resolution

The condition for maximum intensity of X-ray diffraction is given by Bragg's law;

$$2d\sin\theta = \lambda, \tag{3.26}$$

where

$$\frac{1}{d} = \sqrt{\left(\frac{h}{a}\right)^2 + \left(\frac{k}{b}\right)^2 + \left(\frac{l}{c}\right)^2}. \tag{3.27}$$

At room temperature URu_2Si_2 has a body-centered tetragonal crystal structure which has unit cell vectors $a = b \neq c$ and interaxial angles $\alpha = \beta = \gamma = 90°$. Here, our purpose is to determine whether the distortion along the $[1\,1\,0]_{\mathrm{T}}$ direction occurs in the hidden order, so we need to obtain Bragg diffraction spot at the tetragonal $(h\,h\,0)_{\mathrm{T}}$. In this case, we rewrite the above Bragg condition:

$$\sqrt{2}a\sin\theta = \lambda h. \tag{3.28}$$

The uncertainty of the measured lattice spacing is given by the total derivative Δa, which leads to

$$\frac{\Delta a}{a} = -\frac{\Delta\theta}{\tan\theta} + \frac{\Delta\lambda}{\lambda}. \tag{3.29}$$

When a crystal has inhomogeneity or crack, the macroscopic strain occurs in the crystal which gives a distribution of lattice length δa. If the resolution Δa is smaller than the distribution of lattice length δa, we can't detect the Bragg peaks profile accurately. The resolution of the X-ray diffraction is affected by two factors: (i) the diffraction angle term and (ii) the finite spread wavelength of the incident beam.

The finite spread wavelength of the incident beam is determined by the Bragg reflection monochromators for synchrotron X-radiation:

$$\frac{\Delta\lambda}{\lambda} = -\frac{\Delta E}{E} = \frac{\Delta\theta_c}{\tan\theta_c}, \tag{3.30}$$

where θ_c is the diffraction angle of the analyzer crystal. The distribution $\delta\theta_c$ is given by

$$\Delta\theta_c = \sqrt{(\Delta\omega)^2 + (\Delta\tau)^2}, \tag{3.31}$$

where $\delta\omega$ is intrinsic angular width of diffraction and $\delta\tau$ angular divergence of X-ray beam. The intrinsic angular range over which total reflection occurs in a perfect crystal such as Si and Ge when absorption effects are neglected is given by

$$\Delta\omega = \frac{-2e^2}{\pi mc^2}\frac{\lambda^2}{V}\frac{|F_{hkl}|}{\sin 2\theta_B}, \tag{3.32}$$

where V is the volume of the unit cell of the crystal and $|F_{hkl}|$ is structure factor. If we

assume $\delta\tau = 0$ simply, the resolution of incident beam is shown by

$$\frac{\Delta\lambda}{\lambda} = \frac{-4e^2}{\pi mc^2}\frac{d^2}{V}|F_{hkl}|. \tag{3.33}$$

For the Si(311) reflection which we use in this study the energy resolution calculated using above equation is 1.9 $\times 10^{-5}$.

The diffraction angle width $\Delta\theta$ depends on the receiving slit in front of the detector. To achieve $\Delta\theta/\tan\theta$ is small, we use narrow slit (0.1 mm$\times$ 0.1 mm) and set the diffraction angle as high as possible without interference between machines. Figure 3.8 show the estimated lattice constant resolution for the imaging plate and the four-axis diffractometer. Here, we set the energy of the incident beam $E = 18.8$ keV ($\lambda = 0.659$ Å) for imaging plate and $E = 17.15$ keV ($\lambda = 0.723$ Å) for four-axis diffractometer. The imaging plate is an X-ray area detector, so the diffraction angle is limited by the edge of imaging plate ($2\theta \leq 138°$). On the other hand, four-axis diffractometer sets the diffraction angle as high as possible unless the machines interfere with each other. The resolution of the lattice constant $\Delta a/a$ is expected to be higher for higher 2θ (Fig. 3.8), so we focus on the high angle Bragg peak.

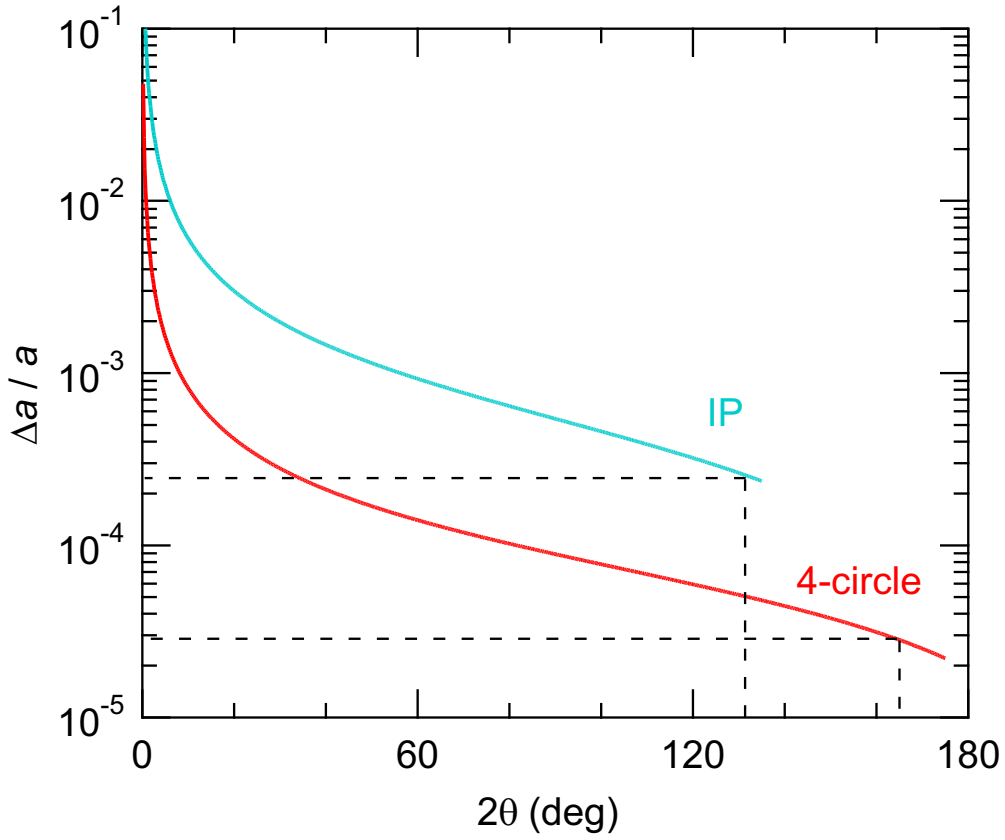

Figure 3.8: Comparison between the estimated lattice constant resolutions $\Delta a/a$ for the imaging plate and the four-axis diffractometer (with the scattering angle resolutions $\Delta 2\theta$ of 0.03° and 0.0008°, respectively). Dashed lines mark the limits for the available 2θ angle spaces for each experimental apparatus.

Determination of X-ray energy

Figure 3.9 shows the temperature dependence of X-ray attenuation length. X-ray can penetrate much deeper into the sample below the absorption edge nearly at 17 keV or 20 keV. Energy dependences of the scattering angle 2θ for $(6\,6\,0)_{\mathrm{T}}$, $(8\,8\,0)_{\mathrm{T}}$, $(10\,10\,0)_{\mathrm{T}}$ and $(12\,12\,0)_{\mathrm{T}}$ are also displayed in the Fig. 3.9. To get bulk information and higher angle as possible, we tune the synchrotron X-ray energy to the peak position associated with the uranium L-edge absorption at 17.15 keV. At this energy 2θ for $(8\,8\,0)_{\mathrm{T}}$ can be as large as 165° at which we can reach the lattice constant resolution is about 2×10^{-5} which is ten times higher than imaging plate value (Fig. 3.8).

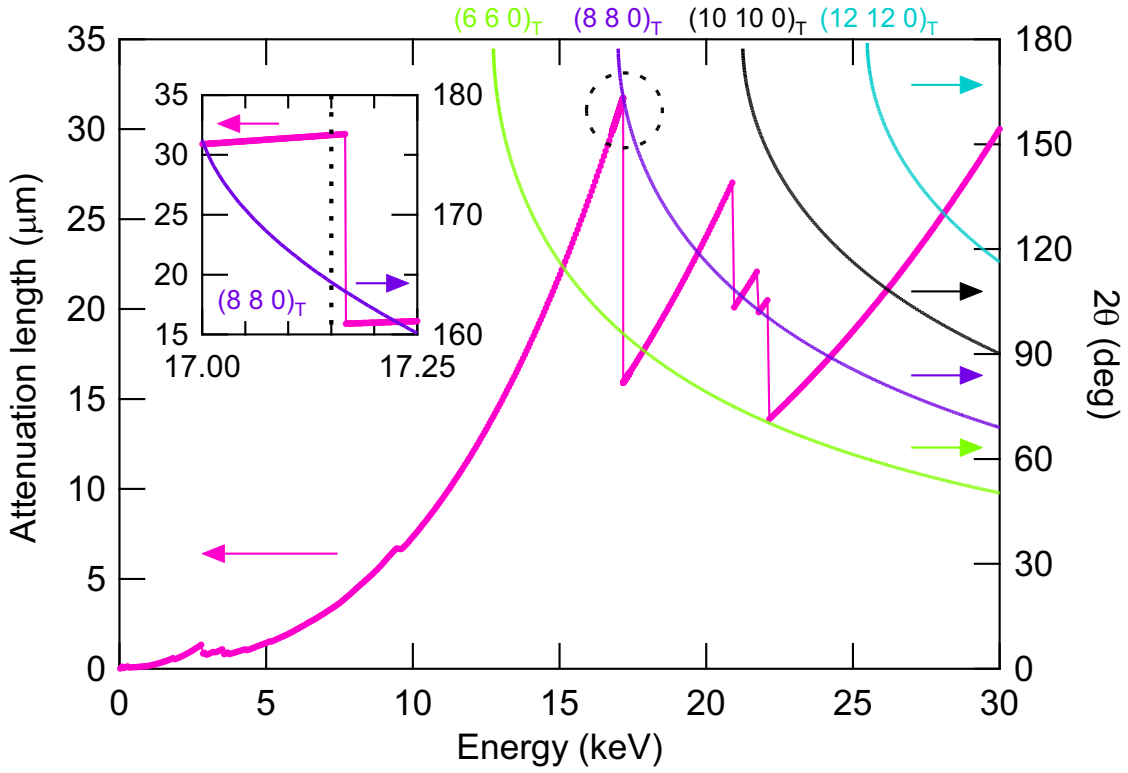

Figure 3.9: Energy dependence of X-ray attenuation length (black) and the scattering angle 2θ (red) for several $(hh0)$ peaks of URu_2Si_2. Inset is an expanded view near the peak in the attenuation length around 17.15 keV.

Setup for four-circle diffractometer

The crystal structure analysis was performed by synchrotron X-ray at SPring-8 (BL02B1). There is four-circle diffractometer produced by HUBER at downstream side in experimental hatch. This diffractometer is operated by SPEC software (Certified Scientific Software), therefore, it is possible for resonant scattering experiment to collect X-ray energy scan on constant Q-value, which almost keep the position of X-ray beam during X-ray energy scan. NaI scintillation detector is equipped for this multi-axis diffractometer. The temperature of the sample is controlled between room temperature and 10 K by the closed-cycle cryocooler equipped in the four-axis diffractometer.

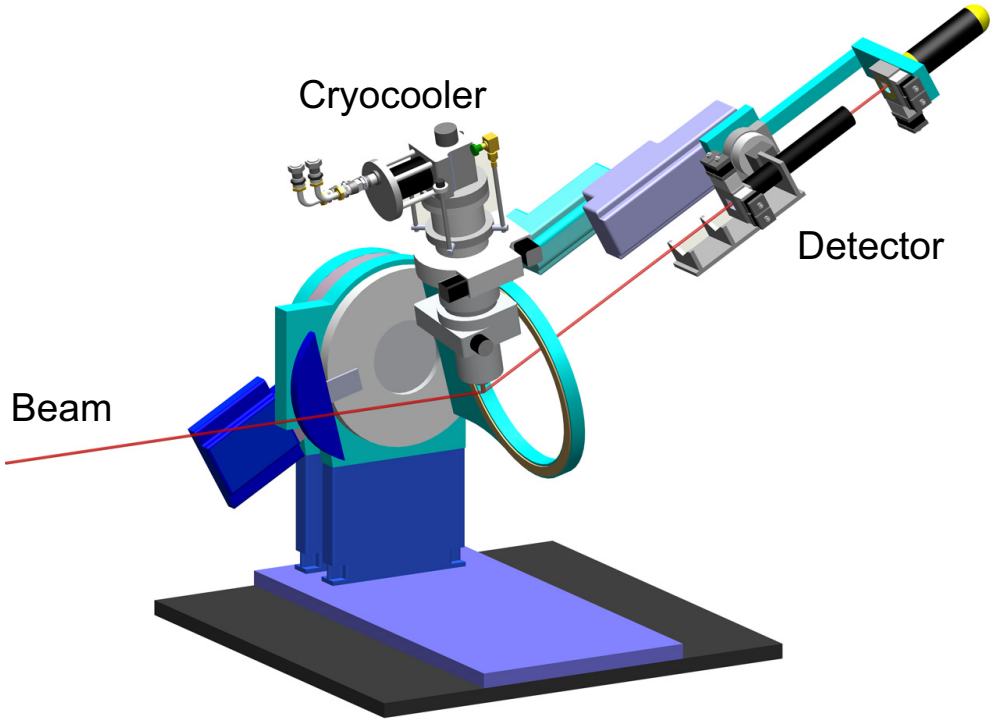

Figure 3.10: A schematic picture of the four-circle diffractometer for the setup $(2\,2\,0)_{\mathrm{T}}$.

To calculate the orientation matrix, we detected some low-angle Bragg diffractions such as $(2\,2\,0)_{\mathrm{T}}$, $(0\,0\,2)_{\mathrm{T}}$ and $(1\,0\,3)_{\mathrm{T}}$, *etc.* Figure 3.10 and 3.11(a) show the schematic picture of the four-circle diffractometer for the setup $(2\,2\,0)_{\mathrm{T}}$ and $(8\,8\,0)_{\mathrm{T}}$, respectively. When we measure $(8\,8\,0)_{\mathrm{T}}$ Bragg peak, we need to lay the detector sideways. In that case we extended the top of the cryostat by thin Ag wire and put the sample on its edge for fear that the copper rod cut off the beam(Fig. 3.11(b)). To improve thermal contact, Apiezon Grease is used between the sample and Ag wire and the thermal grease is used between the Ag wire and cold finger of a cryotstat.

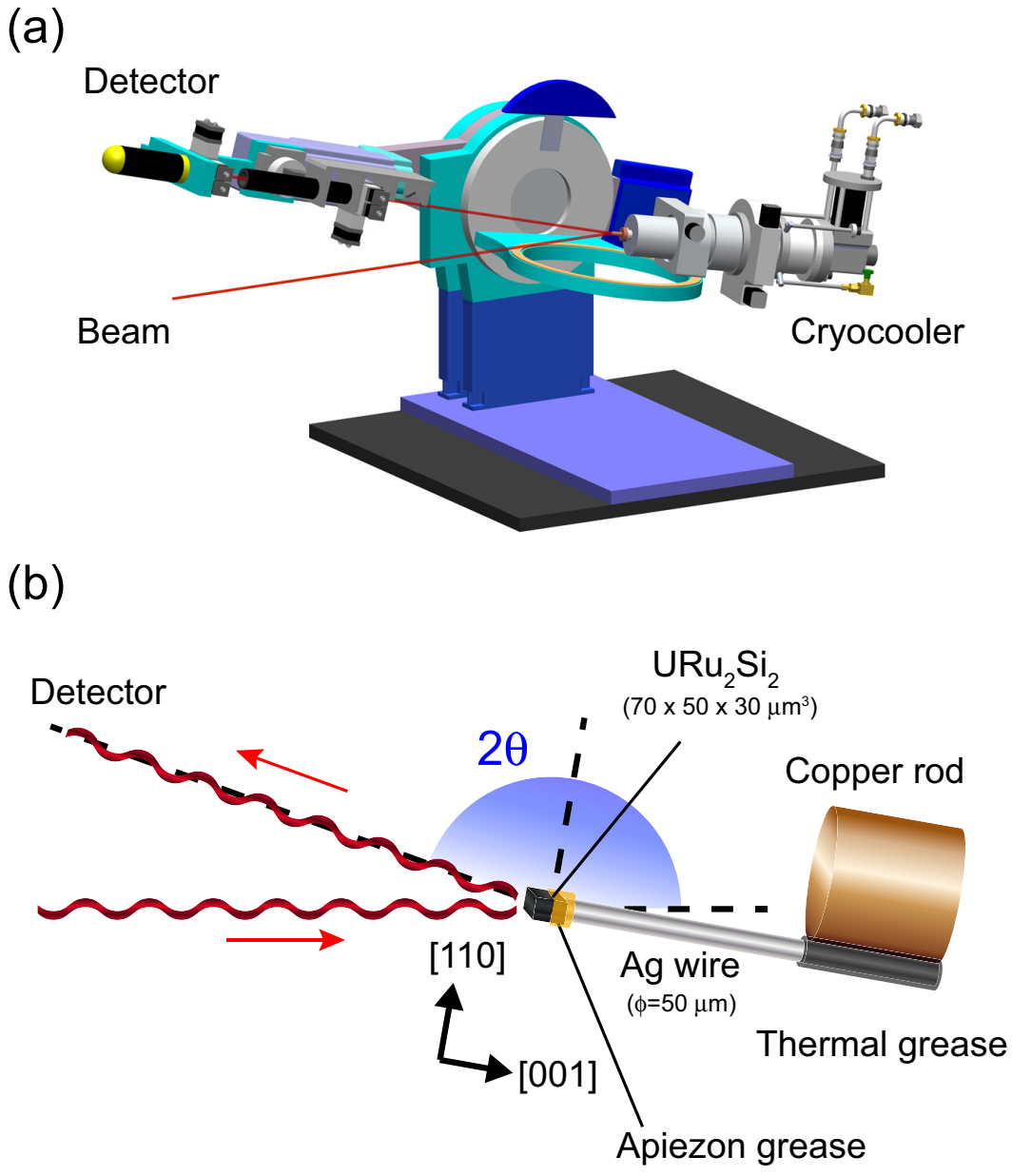

Figure 3.11: (a) A schematic picture of the four-circle diffractometer for the setup $(8\,8\,0)_{\mathrm{T}}$. (b) Expanded view of the top of the cryostat.

3.4 Results

3.4.1 The best sample selected by Imaging plate experiments

The sample was cut or crushed into small pieces and the crystal quality was checked by using the imaging plate. Figure 3.12 show the $(8\,8\,0)_{\rm T}$ Bragg peak profile at $E = 18.8$ keV and $T = 300$ K. We have selected a crystal with the sharpest Bragg peaks out of more than ~ 30 ultraclean crystals (with the residual resistivity ratio close to 670) [12, 13, 29]. This is extremely important to resolve tiny distortion associated with the hidden-order transition. The selected best crystal used in this study has dimensions of $\sim 70 \times 50 \times 30\,\mu\mathrm{m}^3$.

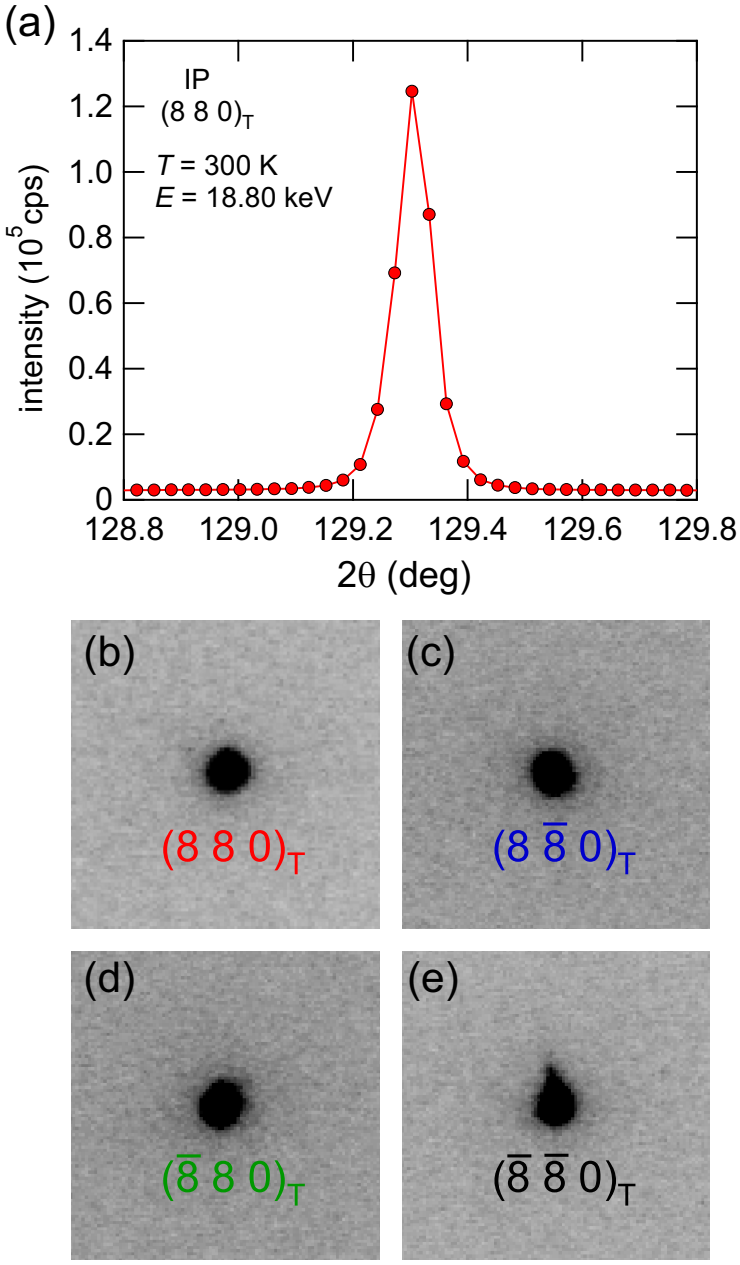

Figure 3.12: (a) Bragg peak profile at $(8\,8\,0)_{\rm T}$. (b)-(e) for $(8\,8\,0)_{\rm T}$, $(8\,\bar{8}\,0)_{\rm T}$, $(\bar{8}\,8\,0)_{\rm T}$ and $(\bar{8}\,\bar{8}\,0)_{\rm T}$.

3.4.2 Precise structural investigation by 4-circle diffractometer

High angle X-ray diffraction experiments for $(8\,8\,0)_{\mathrm{T}}$ Bragg peak were performed at $E = 17.15$ keV and $T = 300$ K (Fig. 3.13a). Fig. 3.13b shows the tetragonal crystal structure of URu_2Si_2 (space group I4/mmm) above $T_{\mathrm{HO}} = 17.5$ K. When $a_{\mathrm{T}} = b_{\mathrm{T}}$, the lattice length a_{T} is calculated by eqn (3.28):

$$a_{\mathrm{T}}(300\,\mathrm{K}) = \frac{4\sqrt{2}}{\sin\theta}\frac{12.3984}{E\,(\mathrm{keV})} \sim 4.127\,\text{Å}. \tag{3.34}$$

The diffraction angle deviation $\Delta 2\theta \sim 0.1$ deg corresponds to the lattice length deviation $\Delta a_{\mathrm{T}} \sim 0.0005$ Å. This value is about four times smaller than the deviation $\Delta a_{\mathrm{T}} \sim 0.002$ Å estimated from IP experiments.

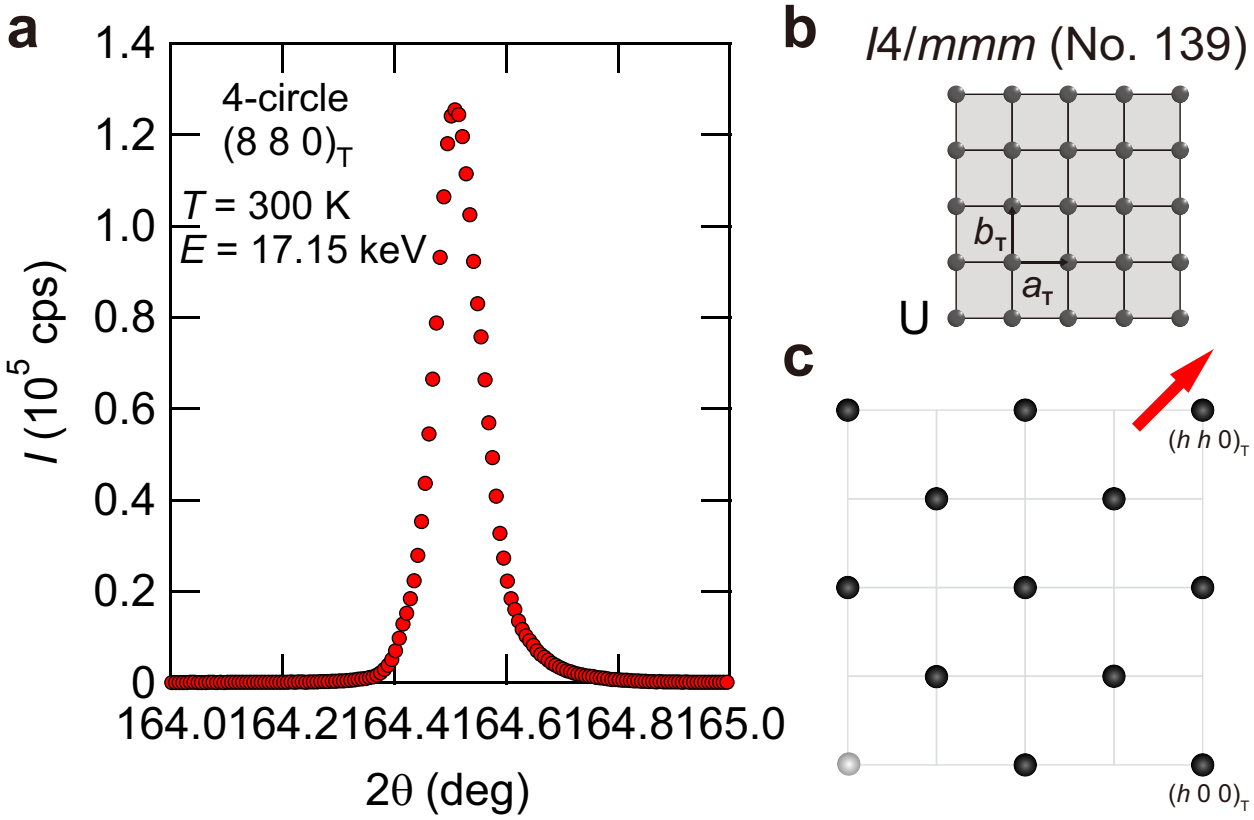

Figure 3.13: **a**. (880) Bragg peak of a high-quality crystal measured with 17.15 keV X-ray (0.723 Å wave length) by a four-axis diffractometer at room temperature. **b**. Schematic U atom arrangements in the basal plane for the tetragonal $I4/mmm$. This system has a single domain. **c**. Bragg points in the $l = 0$ plane for $h, k \geq 0$.

Figure 3.13c shows the X-ray diffraction pattern for $I4/mmm$ symmetry. In the Bravais lattice with $I4/mmm$ symmetry, the diffraction from a plane where the sum of $h + k + l$ is odd gives rise to destructive interference, which is called extinction rule. For instance, the diffractions from $(1\,0\,0)_{\mathrm{T}}$ and $(2\,1\,0)_{\mathrm{T}}$ plane are forbidden and of zero intensity. The arrow in Fig. 3.13c shows the direction for $2\theta/\theta$ scan.

3.4.3 The orthorhombic lattice distortion in the hidden order phase

In Fig. 3.14, we show the temperature dependence of the $(8\,8\,0)_{\mathrm{T}}$ Bragg intensity plotted against the scattering vector $\boldsymbol{q}$, which is measured by the $2\theta/\theta$ mode corresponding to scans along the radial direction from the origin in the reciprocal space. At high temperatures above T_{HO}, in both crystals we have a single peak with a narrow width. From the full width at half maximum, the distribution of lattice constant is estimated as $\Delta a/a \sim 1.3 \times 10^{-4}$, which is more than a factor of 3 smaller than that in the previous studies [18, 83, 88], indicating very high crystal quality of our samples. Upon entering the hidden ordered state below T_{HO}, the data for $RRR \sim 10$ sample shows no significant change in its shape, but for much cleaner sample with $RRR \sim 670$ the single peak above T_{HO} suddenly splits at 17 K. We will discuss the implications of the crystal-purity dependence later, and now we focus on the data of the ultraclean sample. With decreasing temperature the peak position shifts to the higher angle. At 10.5 K and 9.5 K, broadened peak shows clear splitting. The fact that the peak is split below T_{HO} means that the domains are formed in the low-temperature phase.

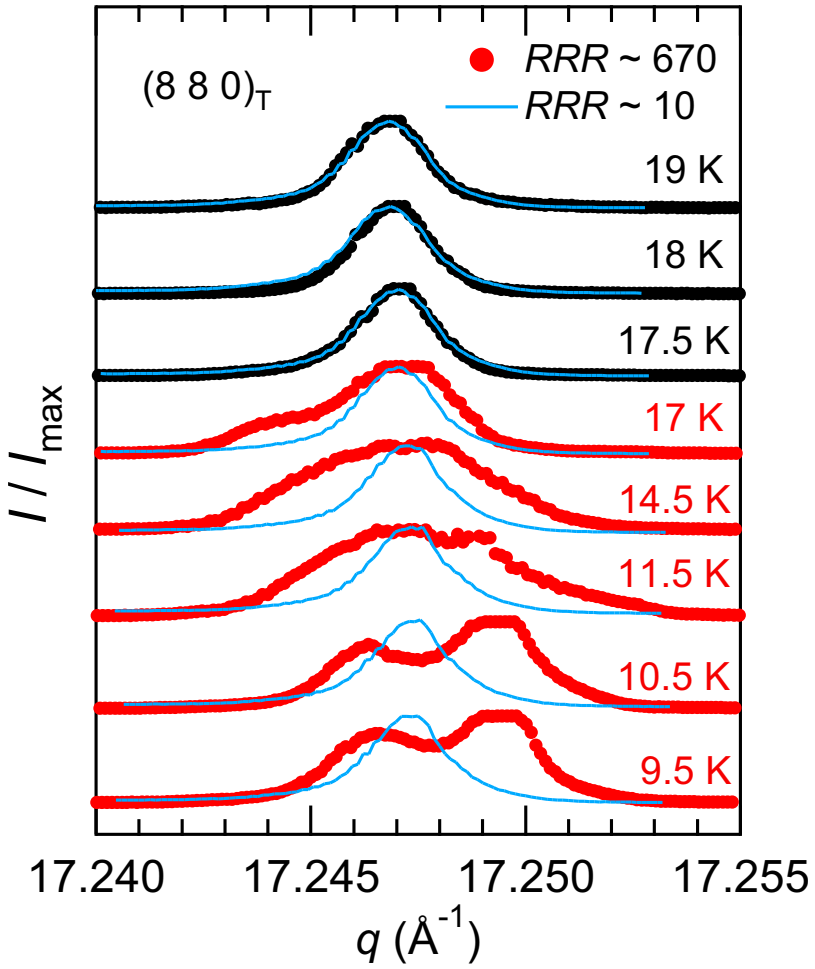

Figure 3.14: Normalized intensity as a function of scattering angle 2θ at several temperatures above (black) and below T_{HO} (red). Each curve is shifted vertically for clarity. The angle resolution roughly corresponds to each data point (circles).

The symmetry of the low-temperature ordered phase should be lower than but belong to a subgroup of the symmetry above the transition temperature. In the high-temperature disordered phase the system has a body-centered tetragonal crystal structure belonging to the $I4/mmm$ symmetry group, which has 15 maximal non-isomorphic subgroups. The only two $Immm$ and $Fmmm$ space groups break the in-plane rotational symmetry in these subgroups (Fig. 2.3). As schematically shown in Fig 3.15a,b, four types of domains are formed in the both $Immm$ and $Fmmm$ structures due to orientational degeneracy of the direction of orthorhombic distortion [89, 90]. Figure 3.15c,d show the expected transformation of the X-ray Diffraction pattern as a consequence of the existence of four domains for $Immm$ and $Fmmm$, respectively. $Immm$-type diffraction patterns indicates that the $2\theta/\theta$ scan along $[110]_{\mathrm{T}}$ direction shows the single peak integrated four signal. On the other hand, four spots split two Bragg peaks for the the $2\theta/\theta$ scan along $[110]_{\mathrm{T}}$ direction in the $Fmmm$-type structure. Our experiments show the two splitting below T_{HO}, which indicates the $Fmmm$-type orthorhombic lattice distortion occurs in the hidden order phase.

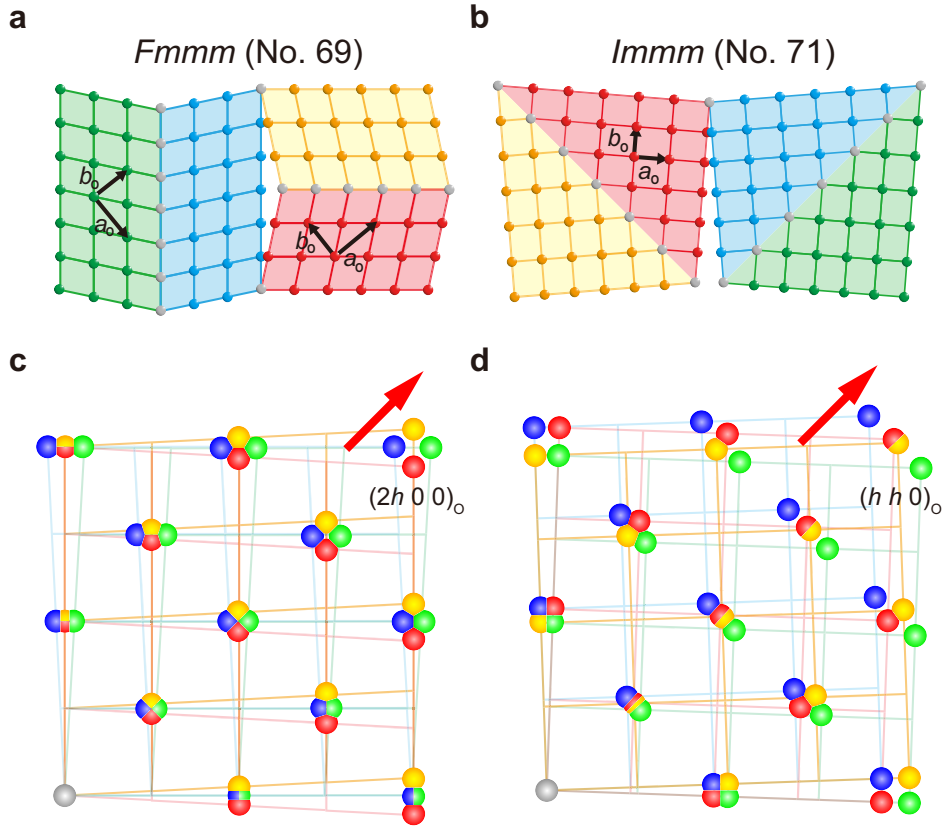

Figure 3.15: **a,b**, Schematic U atom arrangements in the basal plane for orthorhombic $Fmmm$ structure and orthorhombic $Immm$ structure, respectively. **c,d**, The orthorhombic structure forms degenerate domains for $Fmmm$ structure and $Immm$ structure, respectively. $Fmmm$ domains split the Bragg $(h\,h\,0)_{\mathrm{T}}$ points into four $(2h\,0\,0)_{\mathrm{O}}$ points [89, 90].

3.4.4 Temperature dependence of the orthorhombicity

The split peak can be reasonably fitted to two Gaussian peaks (Fig. 3.16), from which orthorhombicity δ is estimated, where $2\theta_1$ and $2\theta_2$ are the two peak angles.

$$\delta = \frac{a_O - b_O}{a_O + b_O} = \frac{\sin\theta_2 - \sin\theta_1}{\sin\theta_2 + \sin\theta_1} \tag{3.35}$$

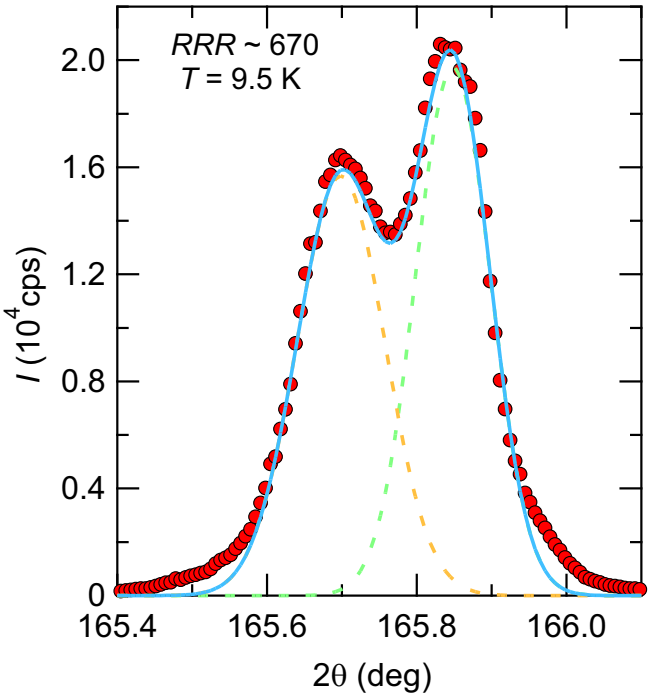

Figure 3.16: The data at 9.5 K below T_{HO} (circles) can be fitted to a sum (solid line) of two Gaussian functions with different lattice constants $a_O \sim 5.8290$ Åand $b_O \sim 5.8281$ Å(dashed lines).

The change in the lattice constant a for $RRR \sim 10$ sample is consistent with the previous high-resolution Larmor diffraction measurements of $(400)_T$ Bragg peak for a similar $RRR \sim 10$ sample [18] at ambient pressure (Fig. 3.17a). In sharp contrast, our new data on the ultraclean sample clearly shows a splitting into two different lattice constants a_O and b_O below T_{HO}, evidencing the transition to the orthorhombic state. We note that these lattice constants do not track the data for the antiferromagnetic phase under pressure and rather show an opposite trend that the averaged constant increases just below T_{HO}. This clearly indicates that our splitting cannot be explained by some inclusion of impurity phase having antiferromagnetism.

The temperature dependence of the orthorhombicity δ is demonstrated in Fig. 3.17b. The orthorhombicity sets in just below T_{HO}, indicating that the lattice symmetry change is clearly associated with the hidden-order transition. Remarkably, unlike the continuous change expected in the usual order parameter at a second-order phase transition, $\delta(T)$ shows a sudden jump at T_{HO} followed by a gradual decrease at lower temperatures, which rather

mimics a first-order transition. The fact that the latent heat has not been reported [9–12] indicates that the first-order nature is very weak; at T_{HO} the discontinuity of the order parameter that characterises the low-temperature phase may be too small to be detected thermodynamically. These results lead us to conclude that the hidden order transition is a weakly first-order phase transition accompanied by lattice symmetry breaking from tetragonal to orthorhombic structure. We note that the present result is consistent with the ^{29}Si NMR width measured under in-plane magnetic fields [28], which shows very similar temperature dependence with a clear jump at T_{HO} (Fig. 3.17b). It has been suggested in a recent theory that the hyperfine fields at the Si site for an antiferroic E^{-}-type order, which has an in-plane anisotropy, can lead to the NMR broadening below the transition [44]. Thus this naturally implies a close correspondence between the orthorhombicity and NMR broadening as found in experiments. The first order behavior cant' be explained by domain scenario, because volume imbalance of the domains only varies with the intensity ratio of the Bragg peaks. In addition, domain boundaries which is not periodical along [110] direction are not responsible for sudden jump of the orthorhombicity. The first order behavior of the orthorhombicity may be directly related to the order parameter of the hidden order phase, but demands for further experimental studies.

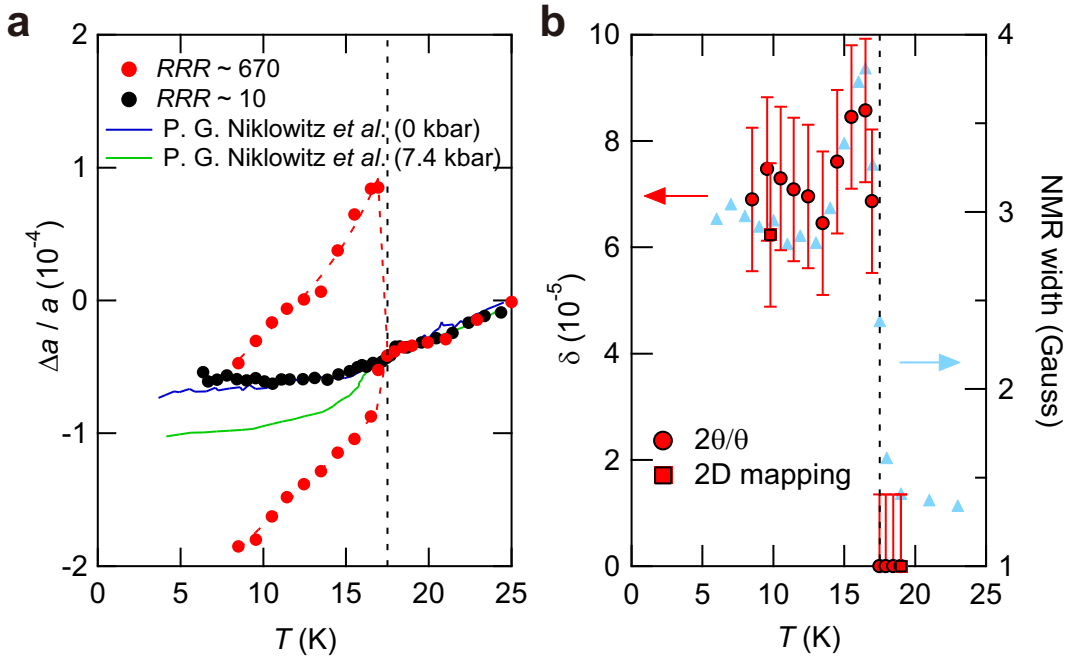

Figure 3.17: **a**, Temperature dependence of lattice constants $\Delta a(T) = a(T) - a(25\,\mathrm{K})$ (circles) compared with the previous report at ambient pressure (hidden order phase) and at high pressure (antiferromagnetic phase) [18]. Dashed lines are guides for the eyes. **b**, The orthorhombicity $\delta = (a_{\mathrm{O}} - b_{\mathrm{O}})/(a_{\mathrm{O}} + b_{\mathrm{O}})$ estimated from the two-peak fitting as a function of temperature (red circles). The orthorhombicity estimated from the two-dimensional mapping at 10 K (see Fig. 4) is also plotted (red square). The temperature dependence of the NMR line width for in-plane field [28] is plotted for comparison (blue triangles, right axis). The dashed line marks the transition temperature $T_{\mathrm{HO}} = 17.5\,\mathrm{K}$.

3.4.5 Two-dimensional $(h\,k\,0)$ scans near the $(8\,8\,0)_{\mathrm{T}}$ Bragg peak

To verify that the peak split originates from the lattice symmetry change to orthorhombic $Fmmm$ structure, we performed the two-dimensional (2D) $(h\,k\,0)$ scans near the $(8\,8\,0)_{\mathrm{T}}$ Bragg peak (Fig. 3.18). At 10 K below T_{HO}, the data reveals a twin-peak structure (Fig. 3.18b) in clear contrast to the single peak above T_{HO} (Fig. 3.18a). Here the integrated intensity keeps the same above and below the transition, demonstrating unambiguously that the twin peaks originate from splitting of the $(8\,8\,0)_{\mathrm{T}}$ Bragg peak.

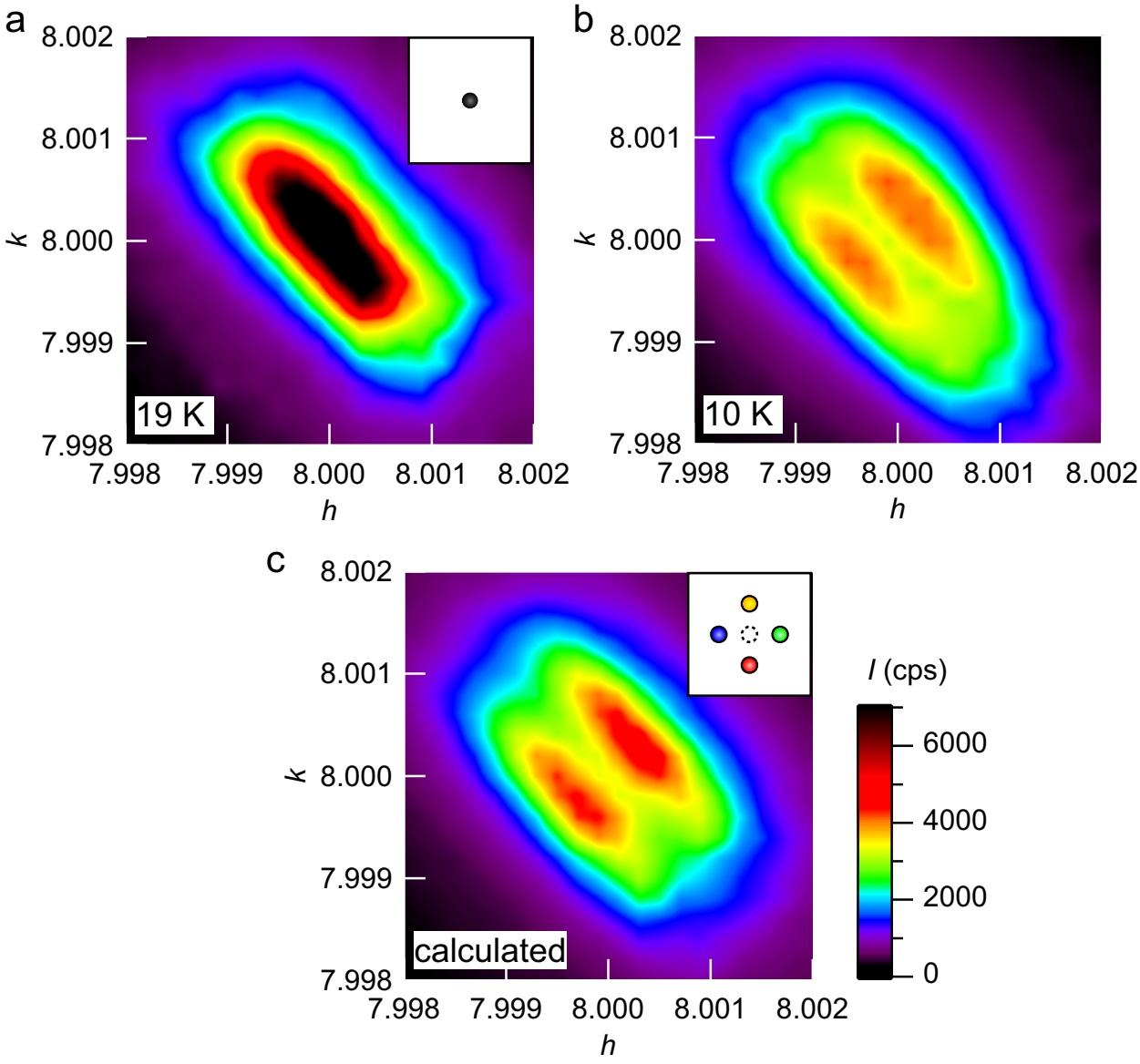

Figure 3.18: Two-dimensional mapping of the $(880))_{\mathrm{T}}$ **Bragg peak. a**, Data of $(hk0)$ scan for $7.998 \leq h, k \leq 8.002$ at 10 K below T_{HO}. **b**, Data taken for the same range at 19 K above T_{HO}. **c**, Calculated results by using the 19-K data for the orthorhombic $Fmmm$ structure with assumptions of $\delta = 6.2 \times 10^{-5}$ and equal volumes of four domains. The color bar indicates the intensity.

The elongated deformation along $[h\,\bar{h}\,0]$ direction is due to the finite mosaicness inevitably present in the crystal. However, the peak split along $[h\,h\,0]$ direction only found below $T_{\rm HO}$ (Fig. 3.19a) cannot come from the mosaicness, but from two distinct lattice-plane spacings inside the crystal (reflecting the domain formation). We also find that along $[h\,\bar{h}\,0]$ direction the peak does not show a clear split but does exhibit some broadening (Fig. 3.19b), which indicates that the split occurs on two directions in the $(h\,k\,0)$ plane. To demonstrate the consistency with the split into four peaks expected in the orthorhombic $Fmmm$ structure [89,90] (Fig. 3.15c), we shift the high-temperature data at 19 K to four directions as sketched in the inset of Fig. 3.18c and add them with the same weight. The calculated result shown in Fig. 3.18c is remarkably consistent with the measured data at 10 K (Fig. 3.18b). The line cuts of this result also reproduce the salient features of the 10 K data; the clear split along $[h\,h\,0]$ and broadened peak along $[h\,\bar{h}\,0]$. The amount of the shifts in the calculation corresponds to the orthorhombicity $\delta = 6.2 \times 10^{-5}$, which is quantitatively consistent with the $2\theta/\theta$ scan data in Fig. 3.17b within experimental errors. These results provide direct evidence that the lattice symmetry is lowered from the tetragonal $I4/mmm$ to orthorhombic F/mmm, and the fourfold rotational symmetry is broken at the hidden order transition.

The in-plane electronic anisotropy elongated along the [110] direction reported in the in-plane field rotation experiments [27, 28, 86, 87] is fully compatible with this symmetry. It should be emphasized that the present results are obtained at zero field, demonstrating that such electronic nematicity is not field induced. The formation of micro-domains evident from the multi-peak structure is also consistent with the above reports. We note that the intensity ratio of the two peaks is temperature dependent (Fig. 3.14) with the integrated intensity unchanged (Figs. 3.18a,b). This suggests that the domain size and the position of domain walls change with temperature in the very clean crystal. This opens the possibility of 'detwinning' by an external force, which may be related to the recent report that the thermal expansion anomaly at $T_{\rm HO}$ increases rapidly with application of extremely small in-plane uniaxial pressure [91].

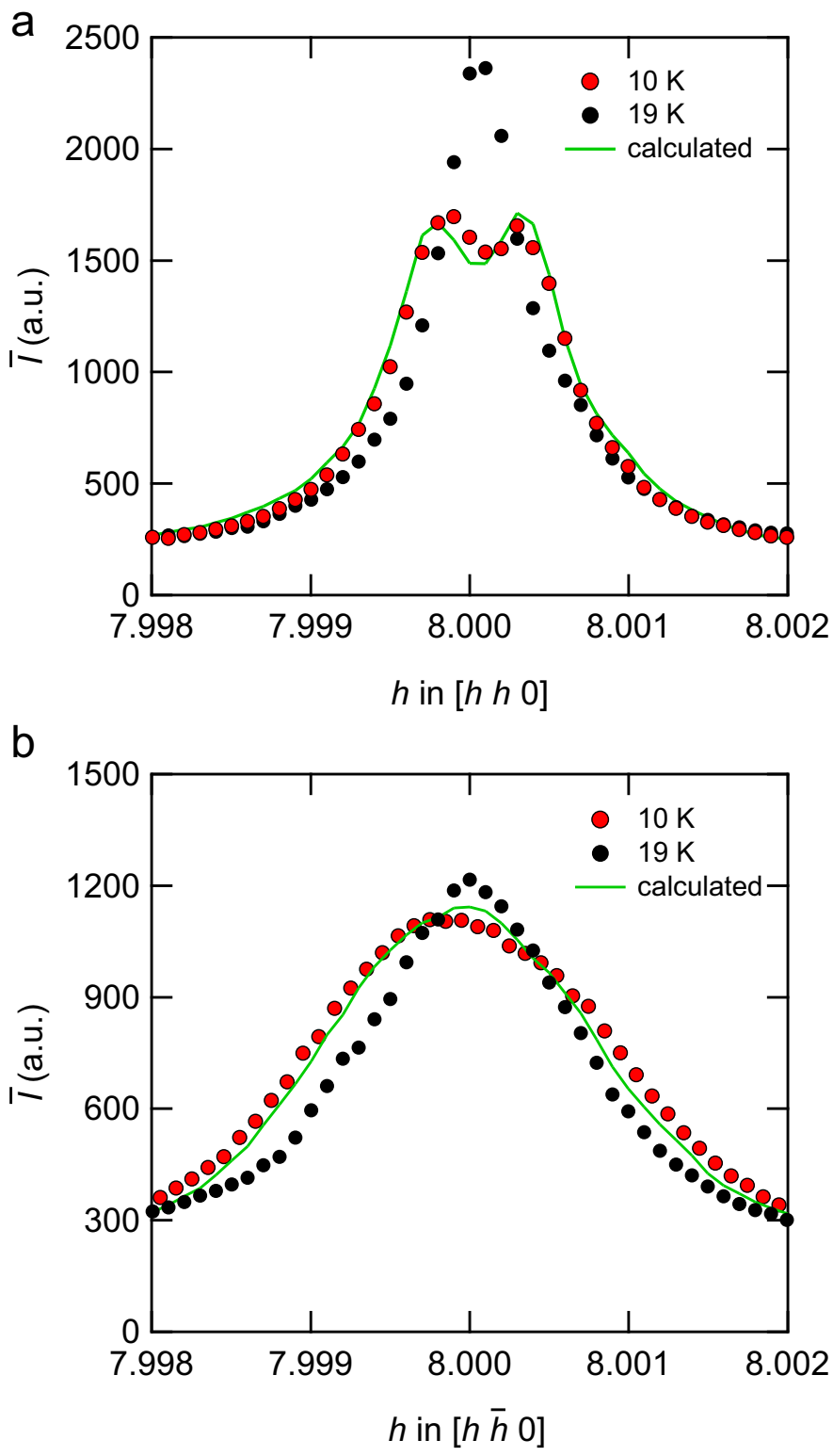

Figure 3.19: **a**, Line cuts along the $[h\,h\,0]$ direction at 10 (red circles) and 19 K (blue circles), which are compared with the calculated one in Fig 3.18**c** (green line). The intensity is averaged over a finite width along $[h\,\bar{h}\,0]$. **b**, The same plot as in **a** but along the orthogonal $[h\,\bar{h}\,0]$ direction. Here the average is taken along $[h\,h\,0]$.

3.4.6 The symmetry of the hidden order in URu_2Si_2

The present results clarify the space symmetry of the hidden order phase, which breaks four-fold rotational symmetry. This, along with the first-order nature revealed in this study, places very tight constraints on the genuine hidden order parameter. Among the allowed irreducible representations for the hidden order (four non-degenerate A_1, A_2, B_1, B_2, and degenerate E symmetries) [66], the orthorhombic $Fmmm$-type space group symmetry pins down that the hidden order belongs to the E-type, more specifically $E(\eta_a, \eta_b)$ with $\eta_a, \eta_b = \pm 1$, in which the sign of $\eta_a \eta_b$ determines the nematic direction of the domain [66]. This establishes a solid base for the recently proposed nematic/hastatic order with in-plane anisotropy [35, 44, 63–67].

The magnitude of orthorhombicity δ is of the order of 10^{-5}, which is two orders of magnitude smaller than that of similar structural transitions from tetragonal $I4/mmm$ to orthorhombic $Fmmm$ phase in isomorphic $BaFe_2As_2$-based iron-pnictide superconductors [90, 92]. This smallness of the lattice change implies that the hidden-order transition is driven by an electronic ordering, and small but finite electron-lattice coupling gives rise to the lattice distortion. It should be noted that several experiments on the electronic structure provide strong evidence of the band folding over the wave vector $\boldsymbol{Q} = (001)$ [21–23,34,86,87]. Such an antiferro-type ordering is expected to couple weakly to the "ferro-type" ($\boldsymbol{Q} = 0$) orthorhombic distortion. We also note that the elastic constants, which are also $\boldsymbol{Q} = 0$ quantities, exhibit only small changes at T_{HO} [82], and it has been pointed out that these are consistent with several different symmetries including the $E(1, 1)$-type state, which is compatible with our results [66].

3.4.7 Sample quality dependence

Another remarkable finding is that the symmetry-breaking orthorhombic lattice distortion is quite sensitive to disorder (Fig. 3.14). The fact that even the low RRR samples exhibit clear signatures of the transition in the specific heat measurements [9–12] indicates that the $\boldsymbol{Q} = (0\,0\,1)$ band folding is a robust feature against disorder. However, the transition temperature T_{HO} shows a discernible decrease with lowering RRR [12], which implies that impurities can perturb the hidden order. These may be related to the rotational degree of freedom of the nematic direction inside the ab plane in the degenerate E-type orders. Indeed the choice of the [1 1 0] direction can be made by the spin-orbit coupling, and impurities can induce disorder in the nematic direction which may prevent the long-range lattice distortion through nontrivial different-$\boldsymbol{Q}$ coupling. We also note that similar high sensitivity to disorder has been found in the electronic nematic phase in $Sr_3Ru_2O_7$ where the nematic anisotropy is found only in very clean samples [93]. Such unusual impurity effects of nematic orders in strongly correlated electron systems deserve further studies.

3.4.8 Comparisons with other experiments

We note that the found structure is consistent with previous results. The $(h\,0\,0)$ peaks do not show any split along the $[h\,0\,0]$ direction [18, 83] (Fig. 3.15c), and the thermal expansion experiment in a large crystal [82] may be insensitive because of the formation of domains whose size should be smaller than $\sim 50\,\mu$m. The expanded unit cell (Fig. 2.3a) leads to the folding of Brillouin zone in the hidden-order phase, and the reconstructed Fermi surface is expected to be similar to the one with antiferromagnetic order of wave vector $\boldsymbol{q} = (1, 0, 0) = (0, 0, 1)$ [35]. This is consistent with recent experiments showing similarities of Fermi surface between the hidden-order and antiferromagnetic phases [23, 34]. Furthermore, the small in-plane anisotropy of cyclotron mass has been reported [86], in agreement with the orthorhombicity along the $[hh0]$ direction. Finally we comment that the softening of elastic constant at low temperatures has been found in $(C_{11} - C_{12})/2$ but not in C_{66}, which at first glance seems to prefer $Immm$ orthorhombicity along $[h\,0\,0]$ direction [82], 45° different from the present results. However, judging from the anomalies found in recent ultrasound measurements at high magnetic fields [94] we point out that this $(C_{11} - C_{12})/2$ softening may rather be associated with fluctuations of an incommensurate $\boldsymbol{q} = (2/3, 0, 0)$ spin density wave order, which has been suggested to be responsible for the high-field phase above the critical field of hidden order (Kuwahara, K. *et al.* unpublished results). It has also been pointed out that the small slope changes observed in $C_{66}(T)$ and $(C_{11} - C_{12})/2$ at T_{HO} can be consistent with several symmetries, and these elastic anomalies may not be very useful for discrimination between the possible symmetries of hidden order [66].

3.5 Summary

Since the discovery of the hidden order transition at $T_{\mathrm{HO}} = 17.5\,\mathrm{K}$ in URu_2Si_2 about 30 years ago, neither structural distortion and nor magnetic ordering have been observed. The magnetic torque [27] and NMR [28] experiments suggested electronic nematicity which breaks fourfold rotational symmetry, but direct evidence is lacking for its ground state at zero field. We report the observation of lattice symmetry breaking from fourfold tetragonal $I4/mmm$ to twofold orthorhombic F/mmm structure by high-resolution synchrotron X-ray diffraction, which clarifies the space symmetry of the order. The estimated difference between a_{O} and b_{O} is tiny (less than 100 fm) and the magnitude of orthorhombicity δ is of the order of 10^{-5}. The smallness of the lattice change implies that the transition is driven by the electronic ordering which distorts the lattice owing to a small electron-lattice coupling. It also makes the detection quite difficult without high-resolution experiments, which explains why the broken symmetry has been hidden for so long. Small orthorhombic symmetry-breaking distortion sets in at T_{HO} with a jump, uncovering the weakly first-order nature of the hidden-order transition. This distortion is observed only in ultrapure sample, implying highly unusual coupling nature between electronic nematicity and underlying lattice.

The present results clarify the symmetry of the hidden order, which breaks fourfold rotational symmetry. This gives the most stringent constraint on the genuine hidden order parameter. The orthorhombic F/mmm point group is consistent with the recently proposed nematic/hastatic order with in-plane anisotropy [35, 44, 63, 65–67]. The next important step toward the final solution is to establish whether the time reversal symmetry is broken or not [95, 96], which deserves further studies.

Chapter 4

Cyclotron resonance in the hidden order phase

4.1 Introduction

In this chapter, we show the cyclotron resonance study on the hidden order phase of URu_2Si_2. Cyclotron resonance is one of the most useful tools to probe of the detailed Fermi surface structure, which is a complementary technique to the quantum oscillation experiments. The cyclotron resonance stems from the transition between Landau levels formed by the quantized cyclotron motion of the conduction electrons. It quantifies directly the effective mass of quasiparticles moving along extremal orbits on Fermi surface sheets through the simple relation

$$m^*_{\mathrm{CR}} = eH_{\mathrm{CR}}/\omega, \tag{4.1}$$

where $\omega = 2\pi f$ is the microwave angular frequency and H_{CR} is the resonance field. It should be noted that in one-component translationally invariant system m^*_{CR} is not renormalized by the electron-electron interaction (Kohn's theorem), but in solids this theorem can be violated especially for the heavy-fermion systems with interacting conduction and f electrons and for multiband systems. Therefore, the momentum dependence of m^*_{CR} in each Fermi surface should contain important information on the electron correlations, which sometimes are a source of emergent novel phases. Although there are several studies on cyclotron resonance in strongly correlated materials, no observations of cyclotron resonance in heavy-fermion compounds have been reported so far.

4.1.1 Cyclotron resonance in the normal metal

In the magnetic field applied along the z-axis perpendicular to the conducting plane (i.e. $\boldsymbol{B}_0 = (0, 0, B)$), a quasiparticle undergoes the circular motion due to the Lorentz force with the angular frequency,

$$\omega_{\mathrm{CR}} = qB/m^*_{\mathrm{CR}}, \tag{4.2}$$

where q is the electric charge carried by a single electron and m^* is the effective mass renormalized by electronic correlation. The equation of the quasiparticle of motion by Drude model is given by

$$\frac{d\boldsymbol{v}}{dt} + \frac{1}{\tau}\boldsymbol{v} = \frac{q}{m^*_{\mathrm{CR}}}(\boldsymbol{E} + \boldsymbol{v} \times \boldsymbol{B}), \tag{4.3}$$

where τ is the scattering time of the quasiparticle, $\boldsymbol{E} = \boldsymbol{E}_0 e^{i\omega t}$ and $\boldsymbol{B} = \boldsymbol{B}_0 e^{i\omega t}$ is the electrical magnetic field with radio frequency ω and $\boldsymbol{v}$ is the velocity of the quasiparticle difined as

$$\boldsymbol{v} = \frac{1}{\hbar}\frac{\partial E}{\partial \boldsymbol{k}}, \tag{4.4}$$

where E is the energy of the quasiparticle and $\boldsymbol{k}$ is the wavevector of the quasiparticle. By solving the eqn (4.3) about $\boldsymbol{v}$, current density $\boldsymbol{J} = nq\boldsymbol{v}$ is given by

$$J_x = \sigma_0 \frac{(i\omega\tau + 1)E_x + \omega_c\tau E_y}{(i\omega\tau + 1)^2 + (\omega_c\tau)^2}, \tag{4.5}$$

$$J_y = \sigma_0 \frac{(i\omega\tau + 1)E_y - \omega_c\tau E_x}{(i\omega\tau + 1)^2 + (\omega_c\tau)^2}, \tag{4.6}$$

$$\sigma_0 = \frac{nq^2\tau}{m^*_{\mathrm{CR}}}, \tag{4.7}$$

where n is carrier number of the quasiparticle. The absorption power for right-hand circular polarized(+) wave and left-hand circular polarized(-) wave $E_\pm = E_x \pm iE_y$ is shown by

$$P = \frac{1}{2}Re(J \cdot E^*) = \sigma_0|E_0|^2 \times \frac{1}{1 + (\omega \pm \omega_{\mathrm{CR}})^2\tau^2}. \tag{4.8}$$

This is the sum of two Lorentzian functions that have two peaks at $\omega = \pm\,\omega_c$ with the width determined by $1/\tau$.

We now consider a k-space electron orbit when $\boldsymbol{E} = 0$ and $\tau \to \infty$. In this simple model, eqn (4.3) is rewritten by

$$\hbar \frac{d\boldsymbol{k}}{dt} = q(\boldsymbol{v} \times \boldsymbol{B}). \tag{4.9}$$

Eqn (4.4) and (4.9) implies that $d\boldsymbol{k}/dt$ is perpendicular to $\partial E/\partial \boldsymbol{k}$. This relation means

$$\frac{d\boldsymbol{k}}{dt} \cdot \frac{\partial E}{\partial \boldsymbol{k}} = \sum_{i=x,y,z} \frac{\partial k_i}{\partial t} \frac{\partial E}{\partial k_i} = \frac{dE}{dt} = 0 \tag{4.10}$$

from chain rule. It follows immediately from this equation that the component of $\boldsymbol{k}$ along the magnetic field and the electronic energy E are both constants of the motion. In other words, this equation determine the electron orbits in k-space: electrons move along curves given by the intersection of surfaces of constant energy with planes perpendicular to the magnetic field. The sign of $\partial E/\partial \boldsymbol{k}$ to identifies a section of Fermi surface as hole-like or electron-like and the direction of the cyclotron motion. In a uniform magnetic field along z-axis, electrons rotate clockwise and holes rotate anti-clockwise for a closed k-space orbits.

The cyclotron motion in the real space reflects the cyclotron orbit in the k-space. For the ellipsoidal hole Fermi surface, there are two kinds of the cyclotron orbits: one is the belly orbit (B) and the other orbit deviated from the belly orbit (L) as shown in Fig 4.1. The cyclotron orbit on the belly (B) of the Fermi surface leads to a closed loop motion in the real space. On the other hand, the cyclotron motion deviated from the belly orbit (L) includes the component of the Fermi velocity parallel to the magnetic field, so the electron moves along a helical path in which the rotation center drifts along the z-axis (parallel to the magnetic field) in the real space. Orbits in k-space which enclose extremal area (corresponding orbit (B) for the ellipsoidal Fermi surface) are especially important because the number of states per frequency interval is particularly high at these points due to no drift effects.

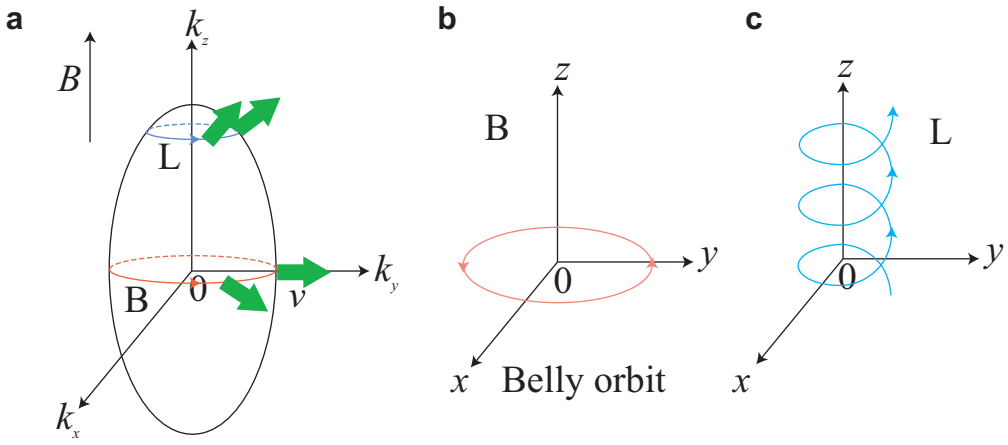

Figure 4.1: **a**. The cyclotron orbit on the belly of the ellipsoidal Fermi surface (red line) and the cyclotron orbit deviated on the berry orbit (brue line). **b**. The real space cyclotron orbit corresponding to the belly orbit. **c**. The real space orbit for the cyclotron motion deviated from the belly orbit.

4.1.2 TE-mode of the microwave cavity

Generally, the cavity resonator can be constructed from circular waveguide shorted at both ends or built by a cylindrical metal box, i.e. cylindrical cavity resonator. Inside the cavity resonator, the electric and magnetic fields exist, the total energies of the electric and magnetic field are stored within the cavity, and the power can be dissipated in the metal wall of the cavity resonator as well as the filled dielectric material. Beside, the filled dielectric material will affect the resonant frequency and Q-value. The transverse modes used in the cavity resonators are the TE and TM mode, which will provide the different dimensions, resonant frequencies and Q-values. TE-mode is used in our study and The equations for the TE_{lmn}-mode are described in formula [98],

$$\begin{aligned}
E_r &= -l\frac{J_l'(k_1 r)}{k_1 r}\cdot\sin l\theta\cdot\sin k_3 z,\\
E_\theta &= -J_l'(k_1 r)\cdot\cos l\theta\cdot\sin k_3 z,\\
E_z &= 0,\\
H_r &= \frac{k_3}{k}J_l'(k_1 r)\cdot\cos l\theta\cdot\cos k_3 z,\\
H_\theta &= -l\frac{k_3}{k}\frac{J_l'(k_1 r)}{k_1 r}\cdot\sin l\theta\cdot\cos k_3 z,\\
H_z &= \frac{k_1}{k}J_l'(k_1 r)\cdot\cos l\theta\cdot\sin k_3 z,
\end{aligned} \tag{4.11}$$

where J_l is the Bessel function of the first kind of order l defined as

$$J_l(z) = \left(\frac{z}{2}\right)^l \sum_{k=0}^{\infty} \frac{\left(-\frac{z^2}{4}\right)^k}{k!\Gamma(l+k+1)}. \tag{4.12}$$

Here Γ is the gamma function, the prime of J_l' means the differentiation. The wavenumber is given by

$$\begin{aligned}
k_1 &= 2x_{lm}/D,\\
k_3 &= n\pi/l,\\
k^2 &= k_1^2 + k_3^2,
\end{aligned}$$

and x_{lm} is the m-th solution for $J_l' = 0$.

The microwave magnetic field in the cylindrical cavity can be obtained from eqn (4.11) and TE_{011}-mode and TE_{012}-mode are shown in the Fig. 4.2. In the TE-mode, tangential electric fields must be zero at cavity walls. In the TE_{011}-mode, the sample is located at the center of the cavity and in the TE_{012}-mode, the sample is located at the $(3D/4, L/4)$, where D is the diameter of the resonant cavity and L is the hight of the resonant cavity. Both samples are placed in a position of maximum magnetic field and minimum electric field. The relation between resonant frequency f and the volume of the cavity is given by

$$(fD)^2 = \left(\frac{cx_{lm}}{\pi}\right) + \left(\frac{cn}{2}\right)^2 \cdot \left(\frac{D}{L}\right)^2, \tag{4.13}$$

This equation indicates the cavity volume (hight or diameter) should be smaller as the microwave frequency is higher.

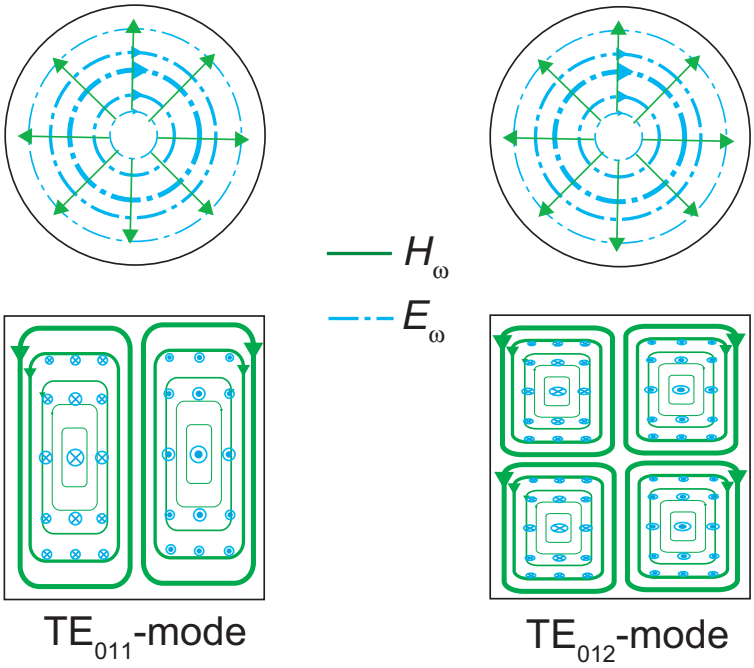

Figure 4.2: The electromagnetic field distribution in the cylindrical cavity: TE-mode:TE_{011}-mode and TE_{011}-mode.

4.1.3 Cavity perturbation method

Cavity perturbation method is analyzed in detail by O. Klein *et al* [99, 100]. Above a lower cut-off frequency, a resonant cavity can sustain many standing wave modes, and near each resonant frequency, the power absorption spectrum estimated from eqn (4.8) has a Lorentzian shape

$$P \propto \frac{1}{4(\omega - \omega_0)^2 + (2\pi\Gamma)^2}, \tag{4.14}$$

where $f_0 = \omega_0/2\pi$ is the center frequency and Γ is the full frequency width at half maximum. f_0 and Γ are the two characteristics of the resonator and their ratio gives the quality factor Q of the cavity, which is defined as

$$Q \equiv \frac{f_0}{\Gamma} = \frac{\omega_0 \langle W \rangle}{L}, \tag{4.15}$$

where $\langle W \rangle$ is the time-averaged energy stored in the cavity and L is the energy loss per cycle.

Here we introduce a complex frequency notation:

$$\hat{\omega} \equiv \omega_0 - i\frac{\omega_0}{2Q}. \tag{4.16}$$

The principle of the cavity perturbation technique is to measure separately the cavity characteristics both before and after a small sample has been inserted. The change in the complex frequency is given by

$$\Delta\hat{\omega} = \hat{\omega}_s - \hat{\omega}_0, \tag{4.17}$$

where the subscripts ' 0 ' and ' s ' denote before and after the insertion of the sample, respectively. If the change $\Delta\hat{\omega}$ is adiabatic, then the product of the period and the time-averaged energy stored is invariant [101],

$$\frac{\langle W \rangle}{\omega_0} = \text{constant}. \tag{4.18}$$

This implies that

$$\frac{\Delta\langle W \rangle}{\langle W \rangle} = \frac{\Delta\hat{\omega}}{\hat{\omega}} \sim \frac{\Delta f}{f_0} - \frac{i}{2}\left(\frac{1}{Q}\right), \tag{4.19}$$

where $\Delta f = f_s - f_0$ is the frequency shift and $\Delta\Gamma = \Delta(1/Q) = 1/Q_s - 1/Q_0$ is the change in the width of the resonance.

For ellipsoidal sample, $\langle W \rangle$ and the change $\Delta\langle W \rangle$ are given by the external electric and magnetic fields $\boldsymbol{E}_0$, $\boldsymbol{H}_0$, and the polarization and magnetization of the sample $\boldsymbol{P}$, $\boldsymbol{M}$, as

follows:

$$\langle W\rangle = \frac{1}{16\pi}\int_{V_c}(|\boldsymbol{E_0}(\boldsymbol{r})|^2+|\boldsymbol{H_0}(\boldsymbol{r})|^2)d^3\boldsymbol{r}, \tag{4.20}$$

$$\Delta\langle W\rangle = -\frac{1}{4}\int_{V_s}(\boldsymbol{P}\cdot\boldsymbol{E_0}(\boldsymbol{r})^*+\boldsymbol{M}\cdot\boldsymbol{H}_0(\boldsymbol{r})^*)d^3\boldsymbol{r}, \tag{4.21}$$

where V_c and V_s are the volume of the cavity and sample, respectively. The internal electric and magnetic fields of the sample $\boldsymbol{E}$, $\boldsymbol{H}$ are obtained by solving the Helmholtz differential equations [98],

$$\Delta^2\boldsymbol{E}(\boldsymbol{r})+\hat{k}\boldsymbol{E}(\boldsymbol{r})=0, \tag{4.22}$$

$$\Delta^2\boldsymbol{H}(\boldsymbol{r})+\hat{k}\boldsymbol{H}(\boldsymbol{r})=0, \tag{4.23}$$

where $\hat{k}$ is the complex wavevector of the microwave. Since outside the sample, $\hat{k}=0$, the differential equation is so-called the Laplace equation.

In the case of spherical sample, we can solve the equations rigorously,

$$\Delta\frac{\langle W\rangle}{\langle W\rangle} = -\frac{\gamma}{n}\frac{\hat{\epsilon}_{\text{eff}}-1}{\hat{\epsilon}_{\text{eff}}+2} \tag{4.24}$$

where $n=1/3$ (the depolarization factor of a sphere), and also

$$\gamma = \frac{V_c|\boldsymbol{E}_0|^2}{2\int_{V_c}|\boldsymbol{E}_0|^2d^3\boldsymbol{r}}, \tag{4.25}$$

$$\hat{\epsilon}_{\text{eff}} = \hat{\beta}\hat{\epsilon}, \tag{4.26}$$

$$\hat{\beta} = -2\left(\frac{-(\hat{k}a)\cos(\hat{k}a)+\sin(\hat{k}a)}{(\hat{k}a)\cos(\hat{k}a)+\sin(\hat{k}a)-(\hat{k}a)^2\sin(\hat{k}a)}\right). \tag{4.27}$$

Here, $\hat{\epsilon}_{\text{eff}}$ is the effective permittivity and a is the radius of the sphere. Depending on the ratio of the skin depth δ to sample size a, we can distinguish two limiting case.

Depolarization Regime

$\hat{k}a \ll 1$ In this limit the fields penetrate uniformly throughout the sample and we can effectively neglect the second term in eqn (4.22). Therefore, it is only necessary to solve the Laplace ' s equation. Under this condition the sample is in the so-called depolarization regime.

Skin depth Regime

$\hat{k}a \gg 1$ In the skin depth regime where the sample size is much larger than the skin depth, $\hat{k}$ cannot be neglected, and we must solve the full set of Helmholtz equations. As shown in eqn (4.19), the energy dissipated in the sample is responsible for the variation of the complex

frequency of the resonator. If we refer to the perturbation $\Delta\hat{\omega}$ (the variation caused by the introduction of the sample in the empty cavity), we have to include a real additive constant, $\lim_{|\hat{\sigma}|\to\infty} |\Delta\hat{\omega}/\omega_0$, that represents the shift of the resonance frequency caused by the excluded volume of the field as the body tends to the perfect conductor limit. This offset is called the metallic shift and it depends on the volume, geometry and position (within the resonator) of the sample. For a sample in the skin depth regime, $\Delta\hat{\omega}$ is simply related to the surface impedance

$$\frac{\Delta\hat{\omega}}{\omega_0} = \xi\hat{Z}_s + \lim_{|\hat{\sigma}|\to\infty} \frac{\Delta\hat{\omega}}{\omega_0}, \tag{4.28}$$

where ξ is the so-called resonator constant. In general, ξ and $\lim_{|\hat{\sigma}|\to\infty} \Delta\hat{\omega}/\omega_0$ depends on the detailed size and shape of the sample under investigation, and we must await an appropriate solution of eqn (4.22) for the $\hat{k} = 0$ in order to determine them. However, from very general arguments, we have been able to determine the appropriate form of an equation which relates an experimentally measurable quantity $\Delta\hat{\omega}/\omega_0$ to an intrinsic quantity $\hat{Z}_s$. In fact, provided one knows certain properties of the material under investigation, eqn (4.28) is enough to determine normalized values of $\hat{Z}_s$.

To simplify the notation, we define a new variation

$$\frac{\Delta'\hat{\omega}}{\omega_0} \equiv \xi\hat{Z}_s = \frac{\Delta\hat{\omega}}{\omega_0} - \lim_{|\hat{\sigma}|\to\infty} \frac{\Delta\hat{\omega}}{\omega_0}, \tag{4.29}$$

where $\Delta'\hat{\omega}/\omega_0$ is the complex frequency shift from a perfectly conducting body of the same size and shape as the sample. The solutions of the real and imaginary parts of eqn (4.29) give

$$\Delta'\frac{1}{Q} = \Delta\frac{1}{Q} \tag{4.30}$$

$$\Delta' f = \Delta f - \lim_{|\hat{\sigma}|\to\infty} \Delta f. \tag{4.31}$$

$\Delta' f/f_0$ will be hereafter referred to as the shift from a perfect conductor.

4.1.4 Surface Impedance

The surface impedance Z_s is given by the surface resistance R_s and the surface reactance X_s,

$$Z_s = R_s + iX_s \tag{4.32}$$

The surface impedance is defined as the ratio of the electric and magnetic field at the surface of the metal [102]

$$\hat{Z}_s \equiv \frac{\boldsymbol{E}_\parallel}{\boldsymbol{H}_\parallel} \tag{4.33}$$

where the $\parallel$ sign indicates the field component in the plane of the surface. This definition is unitless and independent of the surface geometry and normalized by the impedance of the vacuum $Z_0 = 4\pi/c_0$. In the preceding subsection, we described how the change in the complex frequency is related to the surface impedance. As shown in eqn (4.19), (4.30), (4.31), the surface impedance R_s and the surface reactance X_s are given by

$$R_s = \frac{G}{2}\left(\frac{1}{Q_s} - \frac{1}{Q_0}\right), \tag{4.34}$$

$$X_s = G\left(-\frac{f_s - f_0}{f_0}\right) + C, \tag{4.35}$$

where G is the geometric factor and C is the metallic shift. The energy loss of the microwave cavity L (eqn (4.15)) corresponds to the absorption power P (eqn (4.8)), so the peak in $\Delta 1/Q(H)$ can be approximated by the simple Lorentzian

$$\Delta 1/Q(H) \propto \frac{1}{(H - H_{CR})^2 + (\Delta H/2)^2}, \tag{4.36}$$

where the normalized full width at half maximum (FWHM) $\Delta H/H_{CR}$ is given by $2/\omega_c\tau$.

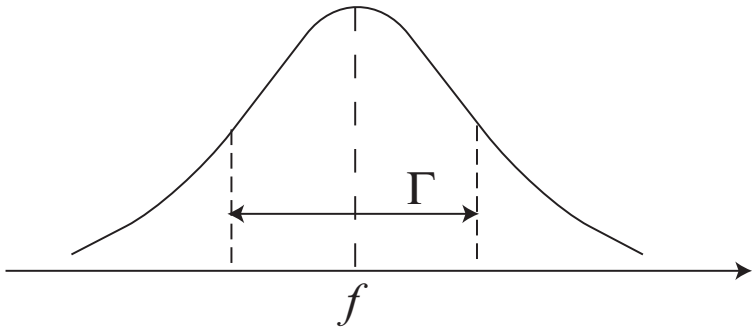

Figure 4.3: The energy loss spectrum of the microwave cavity.

4.1.5 Kohn's theorem

Landau's Fermi liquid theory postulates that an interacting system behaves like a Fermi gas with renormalized parameters. In Galilean invariant systems, there is a simple relation between the thermodynamic mass m^*, the band mass m and the Landau Fermi liquid parameter F_1^s, given by

$$m^* = \left(1 + \frac{F_1^s}{3}\right) m_b. \tag{4.37}$$

Here, the thermodynamic effective mass can be determined experimentally by measuring the specific heat. We emphasize that the effective mass estimated by the cyclotron resonance experiments is not the same as the thermodynamic effective mass. According to the Kohn's theorem [103, 104], the effective mass observed in cyclotron resonance doesn't depend on electron-electron interaction, as the cyclotron resonance sees just the center-of-mass motion, in which the internal force of electron-electron interaction doesn't have any effect. in fact, in organic conductors, it was found that the effective mass measured by cyclotron resonance is much lee than that measured by the Shubunikov-de Haas effect, as the latter is affected by electron-electron interaction whereas the former is independent of it.

In the normal metal with Galilean invariance, the cyclotron mass $m_{\rm CR}$ coincides with the band mass m_b. However, Legget *et al* insisted this is not true for a mutually interacting two-component Fermi liquid even if translationally invariant [105]. Furthermore, C. M. Varma *et al* suggests that this relation is also violated in the heavy-fermion system and the cyclotron mass is given by [106]

$$m_{\rm CR} = m_d \equiv \frac{m^*}{1 + F_1^s/3} > m_b \tag{4.38}$$

where m_d is the dynamical effective mass defined as the thermodynamic mass divided by the renormalization factor.

4.2 Purpose of the cyclotron resonance study in the hidden order state

The nature of the hidden order in the heavy-electron metal URu_2Si_2 is a long-standing mystery [81] since the discovery of the phase transition at $T_{HO} = 17.5\,K$ [9–11]. There are several unique features that appear to be clues for understanding the hidden order phase. Below T_{HO}, an electronic excitation gap is formed on a large portion of the Fermi surface and most of the carriers disappear [29, 107]. Closely related to this, the gap formation also occurs in the magnetic excitation spectra, as revealed by the neutron inelastic scattering [30]. The hidden order ground state with no large moment [32, 84, 85] changes to the large-moment antiferromagnetic state upon applying hydrostatic pressure [16], but the resolved part of the Fermi surface [21, 24–26, 33, 34, 108–110] has a striking similarity between these different phases [34, 108], implying that the hidden order is nearly degenerate with the antiferromagnetic order. The magnetic torque measurements reveal the in-plane anisotropy of magnetic susceptibility [27], which suggests some hidden mechanism causing that the magnetic properties of the hidden order phase show a twofold symmetry in the tetragonal *ab* plane.

Despite the above peculiar signatures, however, the fundamental question "what is the nature of the order parameter in the hidden order phase?" remains open, mainly because a detailed knowledge of the Fermi surface topology in the hidden order is lacking. In fact, quantum oscillation experiments [33, 34, 108] have revealed the existence of small pockets in the hidden order phase similar to those in the antiferromagnetic phase, but the total density of states of these pockets is significantly smaller than the estimate from the electronic specific heat, indicating that there must be some missing Fermi surface sheets with heavy mass in the hidden order phase.

4.3 Experiments

4.3.1 Samples

We used high-quality single crystals of URu_2Si_2 with a large residual resistivity ratio of $RRR = 670$, which were grown by the Czochralski pulling method in a tetra-arc furnace as described in previous chapter. The well defined superconducting transition was confirmed by the specific heat measurements. Experiments have been performed on a single crystal with the dimension of $2.1 \times 0.58 \times 0.10\,\mathrm{mm}^3$.

4.3.2 Methods

We put the crystal on the sapphire rod and rotate the sample to change the direction of applied magnetic field(Fig. 4.4 (e)). When we rotate the sample within [100]-[001] plane, the angle between a-axis and magnetic field is defined as the polar angle θ. The azimuthal angle ϕ is defined by the angle between a-axis and magnetic field as the sample rotating within the [100]-[010] plane. Schematic configuration of the microwave measurements is displayed in Fig. 4.11. The crystal is placed inside the cavity, where the microwave field component H_ω has an antinode for the TE_{011} and TE_{012} modes. The dc field H is applied parallel to H_ω, which excites the microwave current J_ω near the sample surface in the region characterized by the skin depth δ. When the frequency of the cyclotron motion with a radius r_c coincides with the microwave frequency f, the cyclotron resonance occurs.

In the cavity perturbation technique, to get a high-quality factor the resonator must be surrounded by materials with extremely low microwave absorption and low-loss dielectrics. In this study we use a cavity resonator made of OFHC copper which have quality factors Q in excess of 10^4. The microwave input is carried through the coupling hole via the waveguide or coaxial cable, and confined inside the cavity. The field distributions for the TE_{011} mode used in this study are shown in Fig. 4.2. At the center of the cavity, the magnetic field is maximum and the electric field is nearly zero. When the crystal is placed in the antinode of the microwave magnetic field $\boldsymbol{H}_\omega$ ($\parallel$ c axis), the shielding current $\boldsymbol{I}_\omega$ is excited in the ab planes of the sample as shown in the expanded picture of Fig. 4.7. Microwave system has been used by surface impedance experiments at Matsuda laboratory. We applied this system to cyclotron resonance measurements.

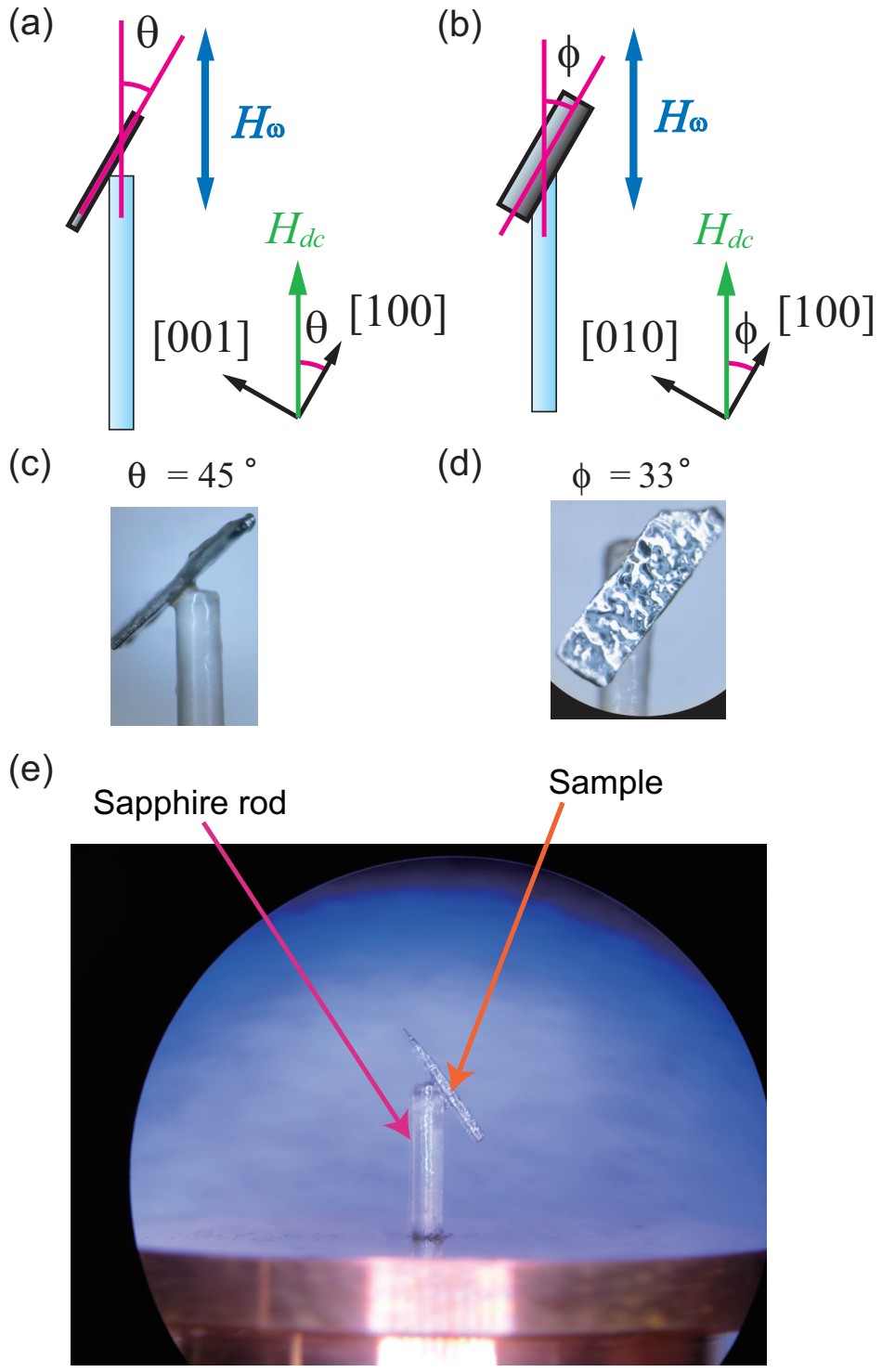

Figure 4.4: Schematic figure of the sample setting in the cyclotron resonance measurements. (a) θ rotation set up. (b) ϕ rotation set up. (c)-(d) Actual setting of the sample. (c) $\theta = 45°$ and (d) $\phi = 33°$ set up.

A schematic diagram of the room-temperature setup is shown in Fig. 4.5. We used Hewlett-Packard 83640A synthesized sweeper as a microwave generator. The input signal is carried to the cavity through the coaxial cable or waveguide, and the output is read by Agilent 8757D scalar network analyzer, where the difference between the output and the reference signals is picked up. We can extract the resonance frequency f and the quality factor Q from the full frequency width at half-maximum Γ. Lakeshore model 340 were used to control each temperature of the sample and cavity. In this study, we performed all the measurements at zero dc magnetic field.

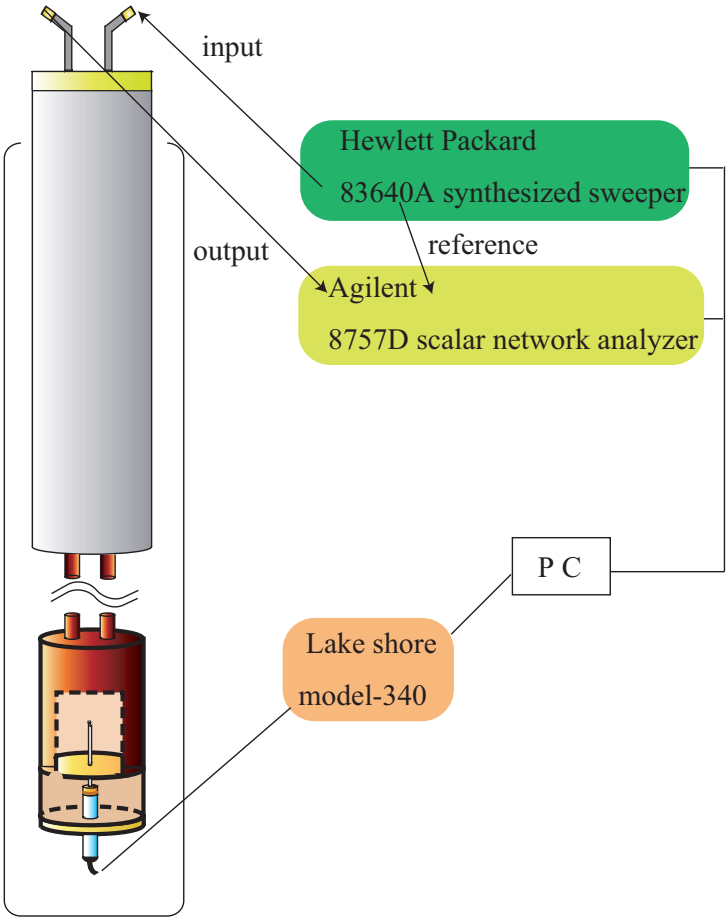

Figure 4.5: Schematic diagram of the microwave surface impedance measurement.

28 GHz cavity

Figure 4.6 shows the schematic picture of the 28 GHz Cu cavity and its sample holder. The 28 GHz cavity is designed by Yuji Matsuda. The superconducting resonator is soaked in the superfluid ^{4}He at 1.6 K, so the resonator functions as the superconducting cavity. For the TE_{011} mode, the resonant frequency and the quality factor of the superconducting cavity are operated with $f \sim 28$ GHz and $Q \sim 20000$, respectively, in the absence of samples. The sample is placed at the center of the cavity and mounted on a sapphire rod with a tiny dot of Apiezon N grease. The sapphire rod is thermally disconnected with the cavity, but in contact with the block of copper which is thermally weakly coupled to the superfluid ^{4}He. The thermometer and heater are installed on the block of copper and we can control the temperature of the sample within ± 1 mK. This is the so-called hot finger technique [111,112] and known to have high precision to measure the temperature dependence of both the surface resistance R_s and the surface reactance X_s even in small single crystals. The wires of the thermometer and heater pass through the stainless-steel pipe, whose one edge is covered with stycast 1266 for maintaining vacuum inside the cavity, and reach the room-temperature apparatus.

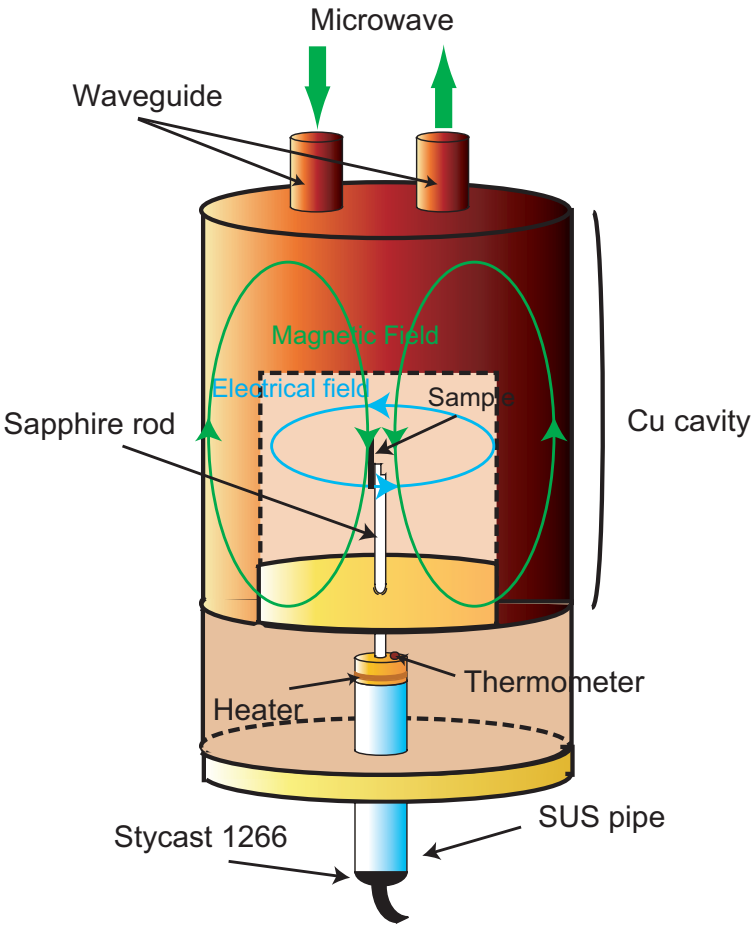

Figure 4.6: Schematic figure of the 28 GHz Cu cavity.

60 GHz cavity

Figure 4.7 shows the schematic picture of the 60 GHz Cu cavity and its sample holder. The 60 GHz cavity is also designed by Yuji Matsuda. The superconducting resonator is soaked in the superfluid ^{4}He at 1.6 K, so the resonator functions as the superconducting cavity. For the TE_{011} mode, the resonant frequency and the quality factor of the superconducting cavity are operated with $f \sim 60$ GHz and $Q \sim 40000$, respectively, in the absence of samples. The sample is placed at the center of the cavity and mounted on a sapphire rod with a tiny dot of Apiezon N grease.

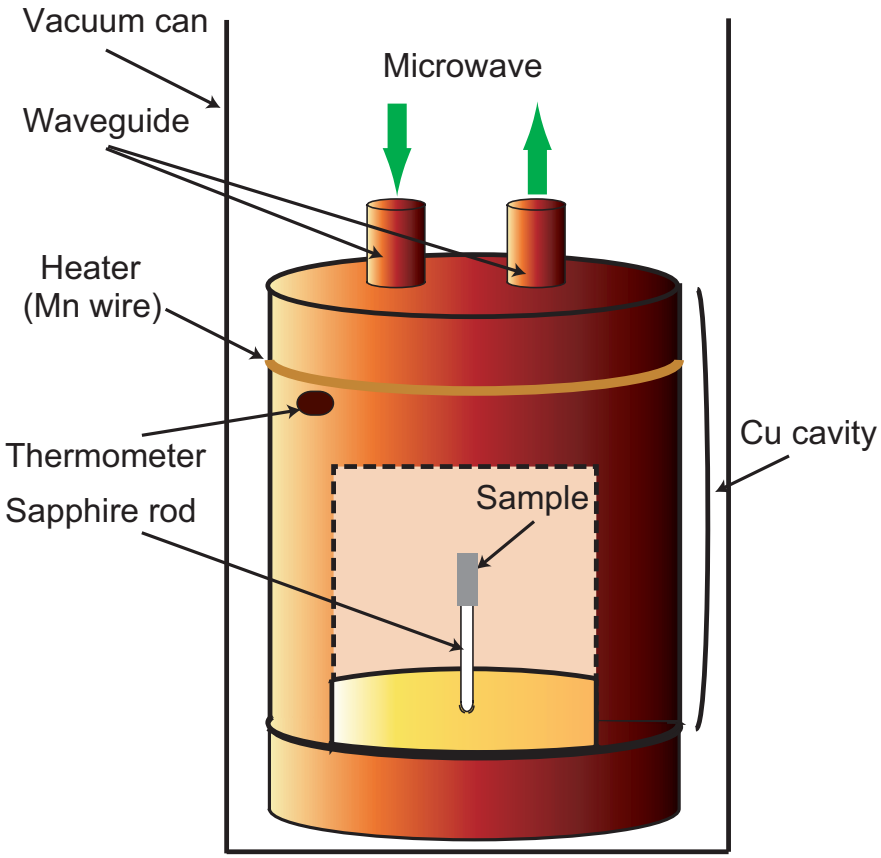

Figure 4.7: Schematic figure of the 60 GHz Cu cavity.

4.4 Results

4.4.1 First observation of the cyclotron resonance in the heavy fermion compounds

Figure 4.8 shows the microwave data for $\boldsymbol{H}//[100]$ at 1.7 K representing the observation of the cyclotron resonance(CR). The microwave power dissipation $\Delta 1/Q$ as a function of applied dc field shows several peaks and at the same fields the frequency shift Δf shows rapid changes, which are expected from the Kramers-Kronig relations between real and imaginary parts of the response functions. These results clearly indicate that the multiple resonances occur in this field range. These resonances show rapid broadening with increasing temperature (see Fig. 4.9), which rules out the electron paramagnetic resonance as the origin of anomalies. Measurements by using different cavities or different modes (see Fig. 4.10) clearly demonstrate that the resonance fields are proportional to the measurement frequency. All of these features establish that these anomalies are due to the CR. The observed seven CR lines are labeled as A to G in the order of corresponding m^*_{CR} from the heaviest (see Figs. 4.10 and 4.12).

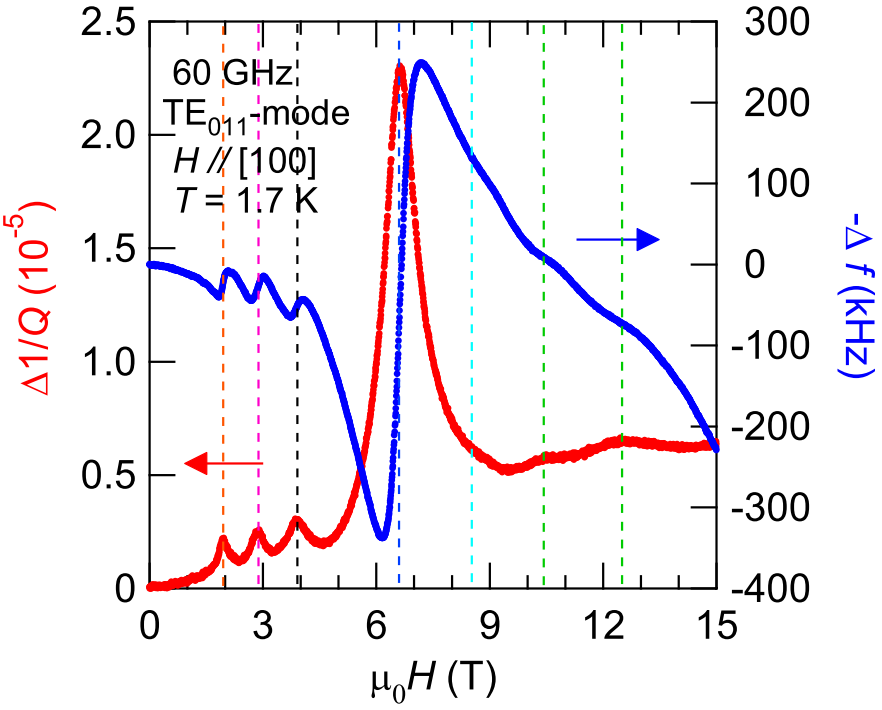

Figure 4.8: Magnetic-field dependence of the change in the microwave dissipation $\Delta 1/Q$ (red, left axis) and the frequency shift Δf (blue, right axis) of the 60-GHz cavity resonator containing a single crystal at 1.7 K. The dc field is along the [100] direction. The weak field dependence measured without the crystal has been subtracted. The dotted lines mark the resonance fields.

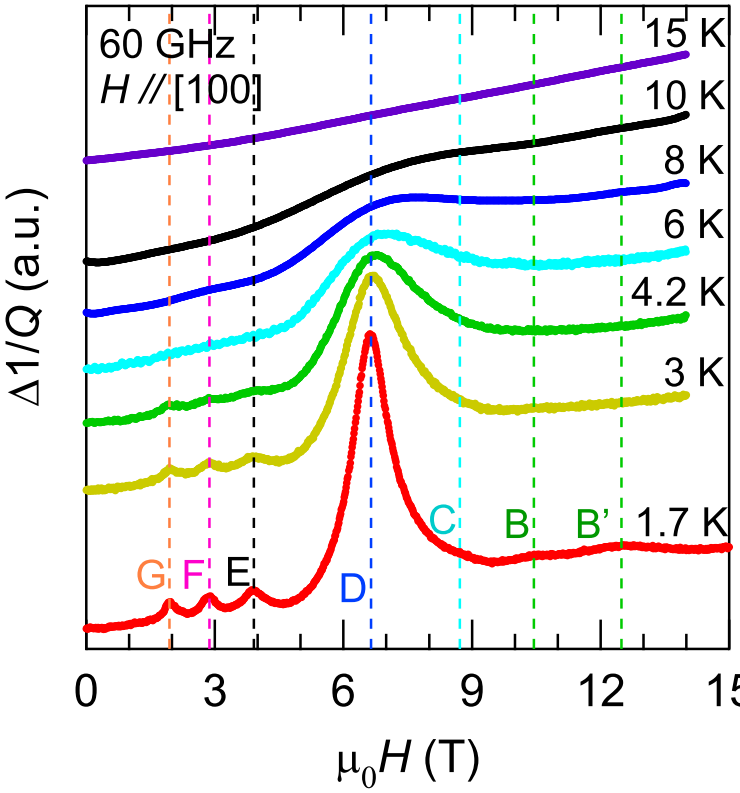

Figure 4.9: Field dependence of $\Delta 1/Q$ at several different temperatures. Each curve is shifted vertically for clarity.

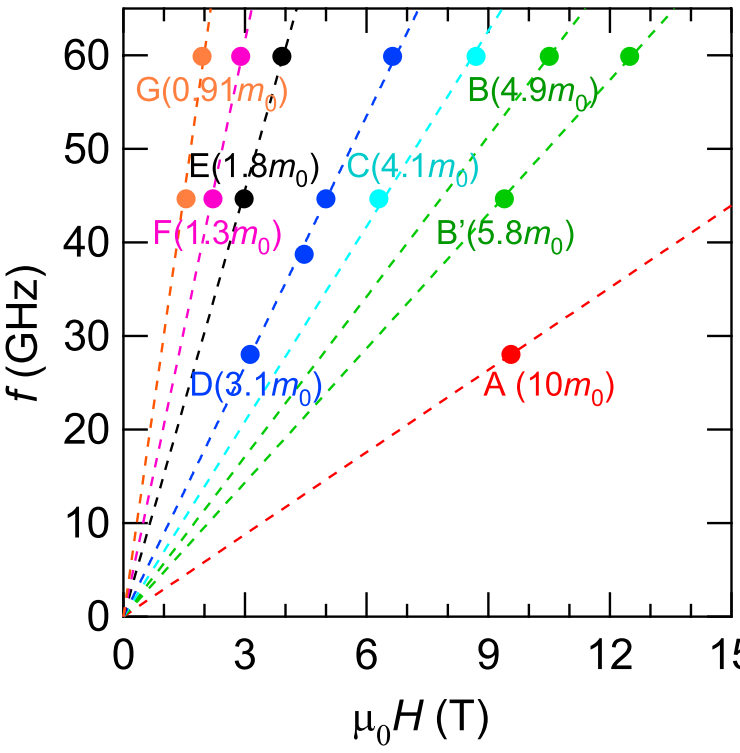

Figure 4.10: Relation between the measured frequencies and the resonance fields for $\boldsymbol{H} \parallel [100]$.

4.4.2 The reason for success of cyclotron resonance experiments

We report the first observation of the cyclotron resonance in URu_2Si_2. There are two reasons for success of cyclotron resonance experiments: (i) sample purity and (ii) the relation between the cyclotron radius r_c and skin depth δ, which are discussed below.

Sample's purity

The detectable condition of the cyclotron resonance demands $\omega_c\tau > 1$ (where ω_c is the cyclotron angular frequency and τ is the scattering time), which means at least one cyclotron motion must be performed during the scattering. From the Lorentzian fitting eqn (4.36), we estimate that $\omega_c\tau$ reaches ~ 20 at low temperatures for the sharpest line D. Our sample's purity with large $RRR = 670$ leads to such a large value of $\omega_c\tau$.

The relation between the cyclotron radius r_c and skin depth δ

For the skin effect, the cyclotron resonance occurs near the surface within the microwave skin depth $\delta = (2\rho/\mu_0\omega)^{1/2}$ ($\sim 0.3\,\mu$m for 28 GHz at 1.7 K where the dc resistivity ρ is $\sim 1\,\mu\Omega$cm in our crystal) when the frequency of the cyclotron motion coincides with the microwave frequency. We note that unlike conventional cyclotron resonance in metals [97], heavy mass and small carriers (namely, slow Fermi velocity v_F) in URu_2Si_2 result in that the cyclotron radius $r_c = v_F/\omega$ may become shorter than δ in our measurement frequency range. A schematic picture of our cyclotron resonance set up is shown in Fig. 4.11.

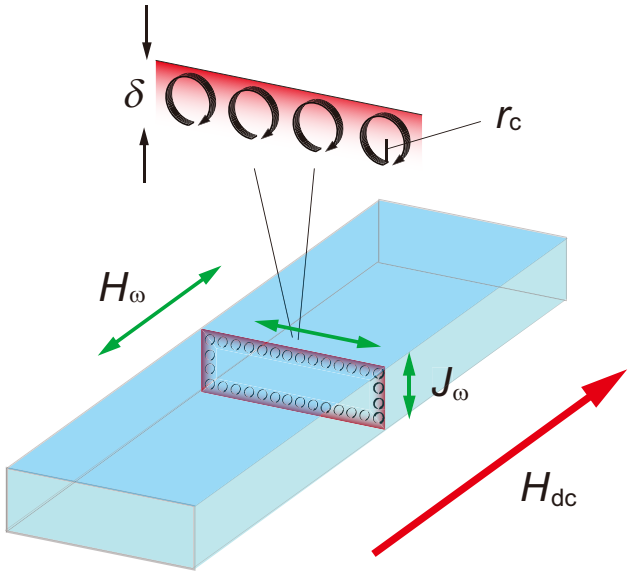

Figure 4.11: Schematic configuration of the microwave measurements.

4.4.3 Determination of the cyclotron mass

The cyclotron resonance data set measured at 28 and 60 GHz in the *ab*, [110]-[001], and *ac* planes are shown in Figs. 4.12(a)-(f). Here the sample temperature is ~ 1.7 K. The cyclotron resonance occurs when the relation $\omega = \omega_c (= eH_{CR}/m^*_{\rm CR})$ is satisfied, from which the angle dependence of $m^*_{\rm CR}$ can be extracted as shown in Fig. 4.13. From eqn (4.36), the microwave dissipation $\Delta 1/Q(H)$ has a peak at $H_{\rm CR}$,

$$\Delta 1/Q(H) \propto \frac{1}{(H - H_{CR})^2 + (\Delta H/2)^2}, \tag{4.39}$$

where the normalized full width at half maximum (FWHM) $\Delta H/H_{CR}$ is given by $2/\omega_c\tau$, ω_c is the cyclotron angular frequency and τ is the scattering time.

In addition to the resonance peaks, the field dependent surface resistance contributes to $\Delta 1/Q(H)$ as well. Since URu_2Si_2 is a compensated metal with equal volumes of electron and hole carries, the magnetoresistance is large at low temperatures for high-quality crystals with large τ [29]. This gives noticeable smooth background signals, as evident especially for 28 GHz. To resolve the cyclotron resonance lines at high fields, we therefore subtract this background field dependence by using polynomial functions (dashed lines in Fig. 4.12(a)). For the resonance line A, we fit the subtracted data by the two Lorentzian functions with different $H_{\rm CR}$ (see Fig. 4.12(b)).

Figures 4.12(a)-(c) display the resonance lines at two different frequencies when the field is inclined from [100] toward [110] direction in the *ab* plane. It is clear that the CR lines D and A gradually split into two peaks when the field direction is rotated from the [100] to [110] direction. For the line A, the FWHM for finite azimuth angles ϕ is significantly broader than that of $\boldsymbol{H} \parallel [100]$ ($\phi = 0°$), suggesting that the split occurs immediately after the field rotation from the *a* axis. On the other hand, the field split occurs at larger angles for the line D. Figure 4.12(f) shows the resonance lines at 60 GHz when the field is inclined from [110] toward [001] direction. The split in line D survives against the field tilt angle θ from the basal plane toward the *c* axis up to the largest tilt $\theta = 30°$ used in this study.

Figures 4.12(d) and (e) display the resonance lines at two different frequencies when the field is inclined from [100] toward [001] direction in the *ac* plane. The line D exhibits a gradual shift to higher fields with increasing tilt angle θ, whereas the lines B and B' merge into a single peak for large θ. We also note that for the *ac* plane rotation, due to the limit of the field range we cannot clearly identify the two-peak feature for the line A. Thus we have large error bars for the line A at finite θ (see Fig. 4.12).

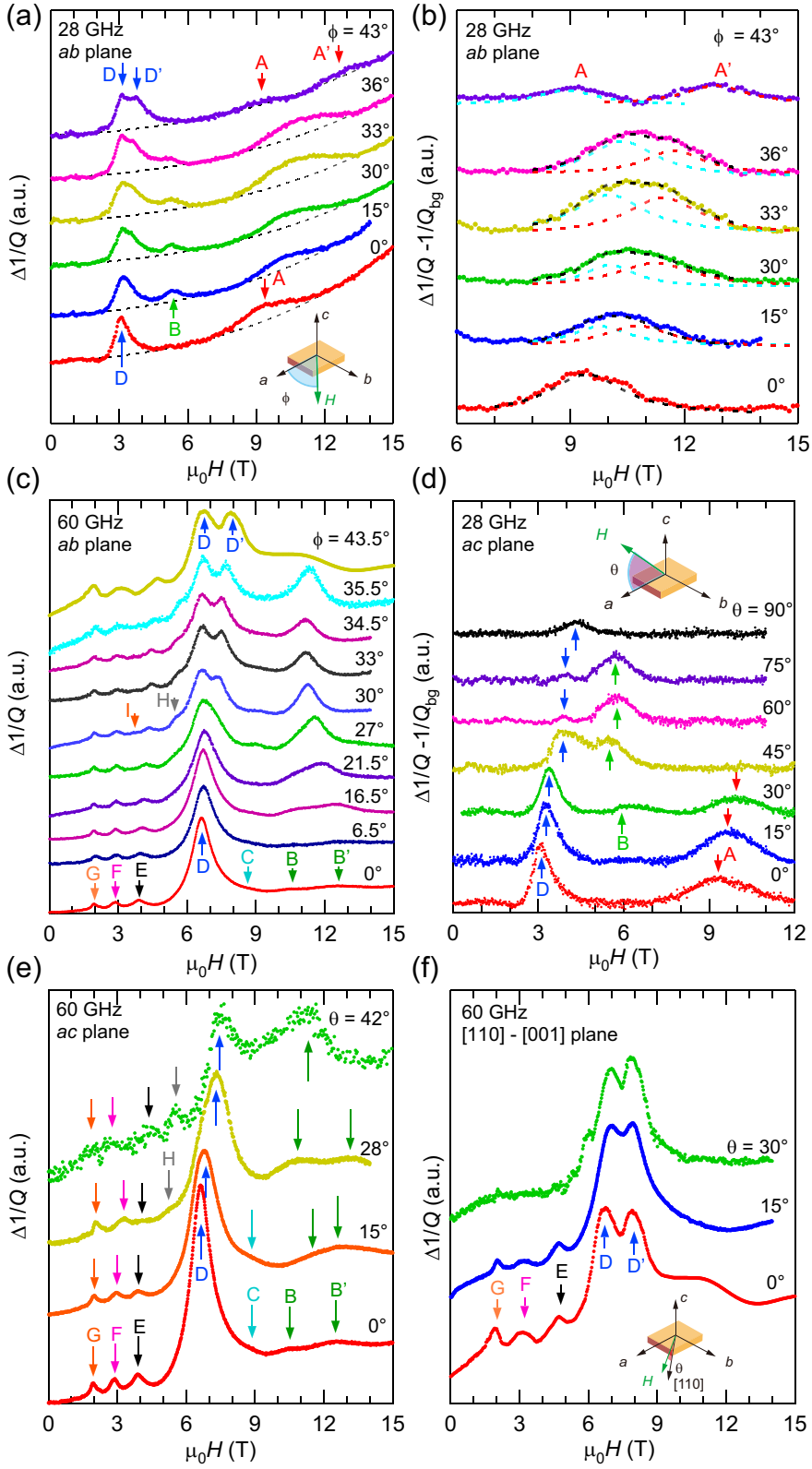

Figure 4.12: (a) $\Delta 1/Q$ under in-plane field rotation at 28 GHz. Here ϕ is the field angle from the [100] direction in the *ab* plane. (b) Smooth polynomial background field dependence $1/Q_{\rm bg}$ (dotted lines in (a)) has been subtracted. At finite angles, the line A shows a broadened shape, which can be fitted to two Lorentzian functions (dashed lines). (c) $\Delta 1/Q(H)$ at 60 GHz for several angles ϕ in the *ab* plane. (d) 60 GHz data in the *ac* plane. Here θ is the field angle from the *ab* plane. (e) 28 GHz data in the *ac* plane. (f) Similar data at 60 GHz but in the [110]-[001] plane.

4.4.4 Assignments of cyclotron mass branches

The field-angle dependence of the CR lines, which can be compared with the band-structure calculations, allows the determination of the angle-dependent electron masses on the FS sheets in the HO phase. The three-dimensional structure of FS mass in the hidden-order phase can be explored by the field-angle dependence of the CR lines, which is summarized in Fig. 4.13. The characteristic angle dependence of each CR line is important to assign the corresponding orbits in different FS pockets. Among the observed CR lines, three lines A (A'), B (B'), and D (D') exhibit strong intensities (solid symbols in Fig. 4.13), which should come from the main FS pockets with relatively large volume. Measurements of the strong lines B and D at two different frequencies provide quantitatively consistent masses, indicating that the mass is field independent at any angle within the measurement range of field.

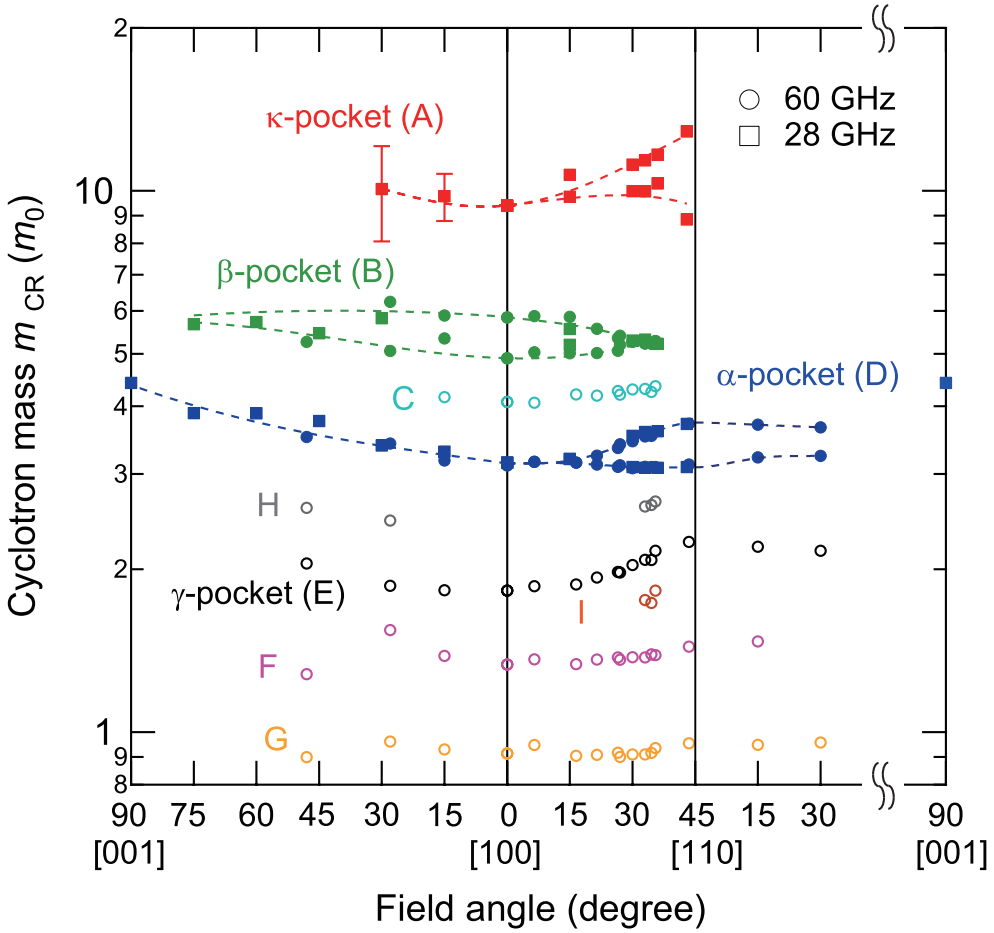

Figure 4.13: Structure of the cyclotron masses $m^*_{\rm CR}$ for each Fermi surface sheet in URu_2Si_2 as a function of field angle for the *ac*-plane (left), *ab*-plane (center) and [110] − [001] plane (right) rotations. The solid (open) symbols are for the resonance lines with large (small) intensities. The dashed lines are guides to the eyes for the main three bands.

The SdH results indicate that the FS in the hidden-order phase is similar to that in the antiferromagnetic state [34, 108]. Thus we compare our CR results with the band structure calculations assuming the antiferromagnetism [35, 38], and discuss the FS structure in the hidden-order phase. The FS structures calculated with several different values of effective field for antiferromagnetism are shown in Fig. 4.14. The results in Fig. 4.14(a) are obtained with the effective field of 40 meV, which corresponds to an antiferromagnetic gap of ~ 4 meV when the renormalization of $\sim 1/10$ is taken into account. In this case there exists the cage structure which is absent in the previous calculation [38], but this structure is sensitive to the gap size. Indeed we found that small energy shifts to this band (4, 8, and 12 meV for Figs. 4.14(b), (c), and (d), respectively) can diminish this cage structure. Thus our calculations are completely consistent with the previous case with a larger gap. In these calculations in the antiferromagnetic state, we always find main three non-equivalent FS pockets with relatively large volumes, labeled as α, β, and κ (see Figs. 4.14(a)-(d)), which have obviously different shapes. Below we show that the α, β, and κ bands correspond to the three strong CR lines D (D'), B (B') and A (A'), respectively. The other lines with weaker intensities (see open symbols in Fig. 4.13) are likely corresponding to the smaller pockets γ inside the α pocket and hourglass-like small pocket near the Z point (see Figs. 4.14(a)-(d) and 4.15(a)), as well as the possible remnant pockets of the cage which can be found in some parameter range of antiferromagnetic gap (see Figs. 4.14(b) and (c)).

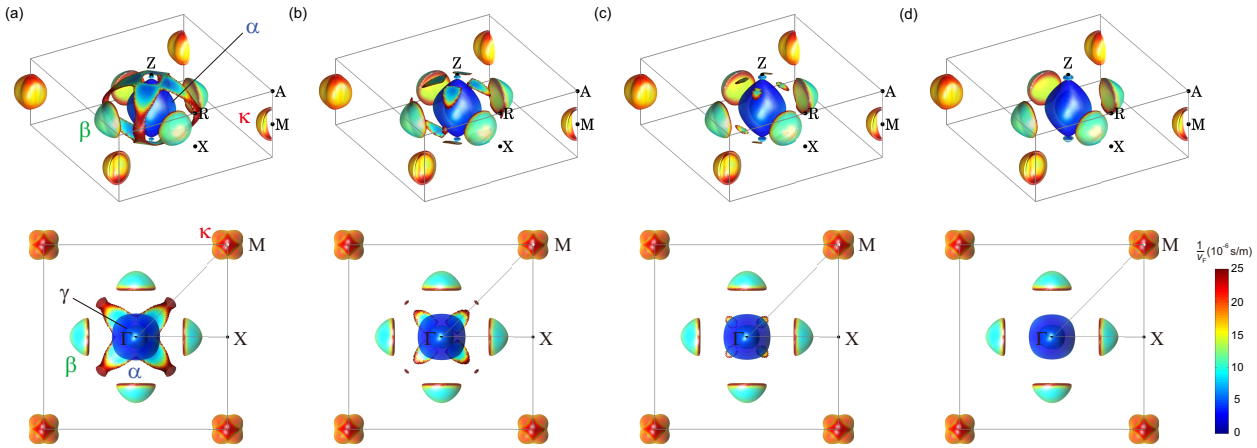

Figure 4.14: (a) Schematic views of FS obtained by the density functional band-structure calculations assuming the antiferromagnetic order. The color indicates the inverse of Fermi velocity $1/v_F$ on the FS sheets. The lower is schematic cross sectional view of FS in a plane including Γ (the centre), X, and M points. The effective field of 40 meV is used which corresponds to antiferromagnetic gap of ~ 4 meV considering the renormalization of $\sim 1/10$. (b)-(d) Similar calculations for larger effective fields. The energy shifts of 4 (b), 8 (c), and 12 meV (d) are used for the cage band. We checked that for these small changes of effective field, the main bands α, β and κ do not show any noticeable change.

$\cdot\,\alpha$ pocket

The α pocket with nearly isotropic shape, which locates around the center of the folded Brillouin zone (Γ point), has the largest volume and is the only hole bands among the main bands. According to the magneto-transport measurements, the Hall coefficient is positive in the hidden-order phase [29], which immediately indicates that this hole band α has much larger mobility than the electron bands in this compensated metal. This α pocket is therefore responsible for the line D having the strongest intensity and sharpest FWHM (with the largest $\omega_c\tau$).

$\cdot\,\beta$ pocket

There are four β electron pockets with hemispherical shape whose center is along the Γ-X line. These pockets yield two different extremal orbits for $\boldsymbol{H} \parallel [100]$, but these two become equivalent for $\boldsymbol{H} \parallel [110]$. This uniquely corresponds to the angle dependence of the line B. This line B also tends to merge towards $\boldsymbol{H} \parallel [001]$, which is fully consistent with the shape of β pockets as well.

$\cdot\,\kappa$ pocket

The κ pockets around M point have much heavier band mass with larger $1/v_F$ than the α pocket (see Figs. 4.14(a)-(d)), which naturally leads us to assign the heaviest line A to the κ pockets. Indeed, the κ FS consists of two crossing sheets, which should give two different orbits for in-plane fields except when the field is aligned exactly parallel to the [100] direction as observed for line A. As for the *ac* rotation from [100] to [001] one expects the branch splitting for the κ pockets, but the large errors of mass determination for line A at finite θ prevent us from observing this split clearly. We stress, however, that no splitting in our sharpest line D for the *ac* rotation toward [001] with much higher resolution is a clear indication that line D does not come from the κ band.

4.4.5 Comparisons with the quantum oscillations

Our assignments for the α and β bands are consistent with the quantum oscillation reports [33,34], in which the largest amplitude oscillation branch is assigned to α [33] and the merging branches for [100] $\rightarrow$ [001] to β [34]. We note that different band assignments to the quantum oscillation branches have been proposed [38], in which the largest Γ-centered hole band is assigned to the ϵ branch observed only at very high fields above $\sim 17\,\mathrm{T}$ [113]. However, such a high-field branch is most likely associated with field-induced transition [113] possibly due to the Lifshitz topology change by the Zeeman effect [114, 115]. It is rather reasonable to assign the most pronounced α branch to this largest hole band, which is consistent with our assignments of CR lines.

Our cyclotron resonance reveals three strong lines which correspond to the main FS pockets including the heaviest electron band κ that has been missing in the quantum oscillation measurements. The heaviest mass and small mean free path of the κ pocket as revealed by the large FWHM of line A are likely responsible for the difficulty in observing the corresponding oscillation frequency.

Evaluation of the electronic specific heat

The full determination of the main Fermi surface sheets enables us to evaluate the electronic specific heat coefficient (Sommerfeld constant) $\gamma = \sum_i \gamma_i$, where γ_i is the contribution from band i. For closed Fermi surface sheets with spheroidal shape, this can be given by

$$\gamma_i \approx N_i \frac{k_B^2 V}{3\hbar^2} \prod_{j=a,b,c} \left(m_j^* k_F^j\right)^{1/3}, \tag{4.40}$$

where N_i is the number of equivalent sheets within the Brillouin zone for band i, $V = 49\,\mathrm{cm}^3/\mathrm{mol}$ is the molar volume of URu_2Si_2, m_j^* is the thermodynamic effective mass and k_F^j is the Fermi wave number along j direction. In a spherical band, k_F is directly related to the quantum oscillation frequency F through the extremal cross sectional area $2\pi eF/\hbar = \pi k_F^2$. We approximate each sheet by spheroid with Fermi wave numbers k_F^j $(j = a, b, c)$, which are estimated by using the quantum oscillations results [33, 34] for $\boldsymbol{H} \parallel [100]$ and $\boldsymbol{H} \parallel [001]$. (For α and γ sheets we assume $k_F^a = k_F^b$.) The thermodynamic effective mass entered here can be replaced by the mass m_{QO}^* measured by the quantum oscillations for each band, which is different from m_{CR}^* determined by the cyclotron resonance [104]. Because the mass m_{QO}^* has been reported only in a limited field angle range, we simply use $\boldsymbol{H} \parallel [001]$ data for each band. We find that the ratio of m_{QO}^* to m_{CR}^* is in a range of 3-4 for the main bands of URu_2Si_2 (Table 4.1). For the heaviest κ band, no quantum oscillations have been observed, so we calculate m_{QO}^* by assuming the ratio $m_{\mathrm{QO}}^*/m_{\mathrm{CR}}^* = 4$.

Table 4.1: Estimation of the electronic specific heat coefficient γ from the comparisons with the quantum oscillation (QO) results [34]. Values marked with † are estimated by assuming the ratio $m^*_{\rm QO}/m^*_{\rm CR} = 4$.

band	$F^{\boldsymbol{H}\parallel[100]}$ (T)	$F^{\boldsymbol{H}\parallel[001]}$ (T)	$m^{*\,\boldsymbol{H}\parallel[001]}_{\rm QO}$	$m^{*\,\boldsymbol{H}\parallel[001]}_{\rm CR}$	$m^*_{\rm QO}/m^*_{\rm CR}$	$\gamma\,(\frac{\rm mJ}{\rm molK^2})$
α [h]	1230	1065	12.4	4.4 [D]	2.8	6.0
$\beta(\beta')$ [e]	219 (751)	422	23.8	6.1 [B]	3.9	27.3
γ [e]	73	195	10	2.4 [E]	4.2	1.4
κ [e]	–	–	$(60)^\dagger$	15 [A]	$(4)^\dagger$	$18.4^\dagger$
total						$53.1^\dagger$

To evaluate γ_i we need the number of sheets N_i for each band, which requires the band assignments. As discussed above, the bands α and β are assigned to the hole sheet centered at Γ point and the four electron sheets located between the Γ and X points (see Figs. 4.13 and 4.14). The band γ with small frequency F and light mass reported by the quantum oscillation experiments [34] can be assigned to the small electron pocket inside the α sheet, which we associate with the CR line E with light mass. We ignore the η band which has been observed only in a limited range of field angle [34], which likely comes from some extremal orbits on the remnant of the cage with small volume. We also do not consider other branches appeared only at very high fields named as δ [114], ϵ [113], and ζ [115], which may be associated with field-induced transitions. Because of the compensation condition, the volume of κ electron bands at the zone corner (which has effectively two pockets) can be estimated by the volumes of one α hole pocket, four β electron pockets, and one γ electron pocket. From this we can estimate the total Sommerfeld constant as large as $\sim 53\,\mathrm{mJ/mol\,K^2}$ (Table 4.1), accounting for more than 80% of the experimental value of $\gamma \approx 65\,\mathrm{mJ/mol\,K^2}$ [10]. Considering the assumptions we made, we infer that the agreement is reasonably good. We can make further improvement when we take into account the contributions from the cage with hole-like character, which further make the κ volume larger.

Fermi surface topology of the α hole band

The quantum oscillation experiments show that the oscillation frequency (F_α) of the α band changes only weakly with field rotation both within the ab and ac planes, indicating nearly spherical Fermi surface shape [33, 34]. It is intriguing that for the in-plane fields, the Fourier transfer spectrum of the oscillations above the upper critical field ($\sim 12\,\mathrm{T}$ for $\boldsymbol{H} \perp [001]$) shows multiple four-peak structure in a wide range of azimuth angle ϕ [33, 108]. The separation ΔF between these peak frequencies are nearly angle-independent ($\Delta F \sim 0.07\,\mathrm{kT}$), and the number of the oscillation frequencies for $\boldsymbol{H} \parallel [110]$ remains the same as that for $\boldsymbol{H} \parallel [100]$. This is completely different angle dependence from the branch splitting near the [110] direction found in our cyclotron mass for the line D.

Very recent Shubnikov-de Haas studies [108] indicate that the three frequencies of the four-peak structure are associated with α band and one lowest frequency comes from the β' orbit. We propose that such three frequencies for the α band with a constant separation ΔF observed only for in-plane fields originates from the field-induced magnetic breakdown effect. Near the Z point of the Brillouin zone, there is a very small electron pocket connected to the next zone (Figs. 4.14 and 4.15), which has an hourglass shape. The band-structure calculations show that a large electron sheet around the Γ point and a slightly smaller hole sheet around the Z point in the paramagnetic state [33, 38] undergo partial gapping by the $\boldsymbol{Q}_C = (0, 0, 1)$ zone folding, which results in divided small pockets; the four β pockets, the cage, and the 'hourglass' pocket [35, 38]. This small hourglass pocket is located very close to the [001] pole of the α hole sheet (Figs. 4.14 and 4.15). Recent theoretical calculations suggest that several multipole ordered states possible for URu_2Si_2 have overall similar FS topology as the antiferromagnetic case shown in Figs. 4.14 and 4.15 [35].

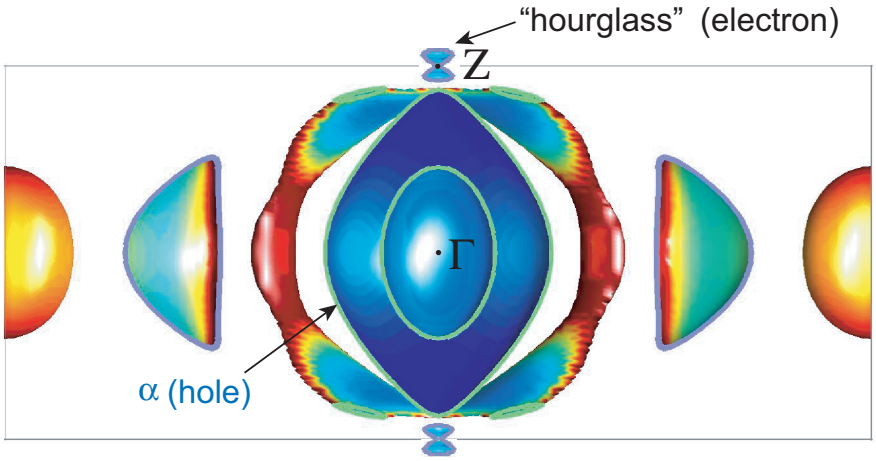

Figure 4.15: Fermi surface (the same as Fig. 4.14(a)) viewed along the [100] direction. Thin black lines define the Brillouin zone and the color shades depict the magnitude of $1/v_F$. Thick lines indicate the cross-sectional profile of the FS in a plane including Γ, Z and X points (see Fig. 4.14(a)).

When a high magnetic field is applied perpendicular to the [001] direction, electrons may tunnel through this small separation between the α hole sheet and the small hourglass electron pocket. The probability of the breakdown occurrence depends exponentially on the field strength, $p = \exp(-H_0/H)$, where the breakdown field H_0 depends on the size of the gap. At high enough fields $H \gtrsim H_0$, one can see several different orbits, as shown in Figs. 4.16(a)-(c), which provides a natural explanation for salient features observed in the quantum oscillation experiments. The breakdown near a [001] pole of the α sheet should decrease the effective oscillation frequency from F_α [Fig. 4.16(a)] to $F_\alpha - \Delta F$ (Fig. 4.16(b)). This is caused by the reduced effective area of the cyclotron orbit with 'figure-eight' topology, which is due to a combination of the α hole pocket and the hourglass electron pocket [116]. Another set of breakdown near the other pole leads to the third frequency $F_\alpha - 2\Delta F$ (Fig. 4.16(c)). Therefore the three-peak structure in the frequency spectrum with the ϕ-independent separation ΔF between the peaks can be understood by this mechanism. This also explains the fact that the reduced frequency branches $F_\alpha - \Delta F$ and $F_\alpha - 2\Delta F$ disappear once the field direction is inclined from the *ab* plane, because for such fields the orbits have large separation between the α and hourglass pockets. The breakdown probability of each orbit is $(1-p)^2$ for F_α (Fig. 4.16(a)), $2p^2(1-p)^2$ for $F_\alpha - \Delta F$ (Fig. 4.16(b)) and $p^4(1-p)^2$ for $F_\alpha - 2\Delta F$ (Fig. 4.16(c)). The normalized field dependence of the breakdown probability is shown in Fig. 4.16(d). From comparisons between these damping factors and quantum oscillation FFT amplitude in the field range from 8 to 15 T [108], we estimate the breakdown field H_0 of the order of $\sim 5\,\mathrm{T}$. Figure 4.16(d) also shows that in the high field range above $\sim 2H_0$, the damping factors of three orbits are of the same order and their ratios have no significant dependence of magnetic field, which also seems to be consistent with the quantum oscillation experiments.

The size of the hourglass pocket and hence the magnitude of ΔF may be sensitive to the details of band-structure calculations, but the present FS in Fig. 4.15 gives $\Delta F \sim 0.03\,\mathrm{kT}$, which is the same order as the experimental observations. Recent band-structure calculations suggest that the shape of the α sheet near the poles in the hidden-order phase are sensitive to the order parameters [35], which may affect the probability of the breakdown at the field range used in the quantum oscillation studies. We stress that our newly found branch splitting of the cyclotron resonance is not originated from this breakdown effect, because our field range ($\mu_0 H_{\mathrm{CR}} \sim 3\,\mathrm{T}$ for the α band at 28 GHz) should be lower than the breakdown field H_0. Moreover, the angle dependence of the cyclotron resonance is quite different from the three-peak behavior in the quantum oscillations. These results clearly indicate that the FS shape of the hole α band is nearly spherical, and that the CR mass split results from the peculiar in-plane mass anisotropy which is not directly related to the shape of FS. (In other words, the slope of the energy-momentum dispersion at the α FS is different for different directions while the size of Fermi momentum remains nearly the same (see Fig. 4.17(b)).) We also note that for the mass determination the cyclotron resonance in a high-quality crystal with large $\omega_c\tau$ (~ 20 in our case) can yield a much higher resolution than the quantum

oscillation measurements, which require the analysis of temperature dependent oscillation amplitude. This allows us to expose the anisotropic mass structure which has been hidden in the hidden-order phase of URu_2Si_2.

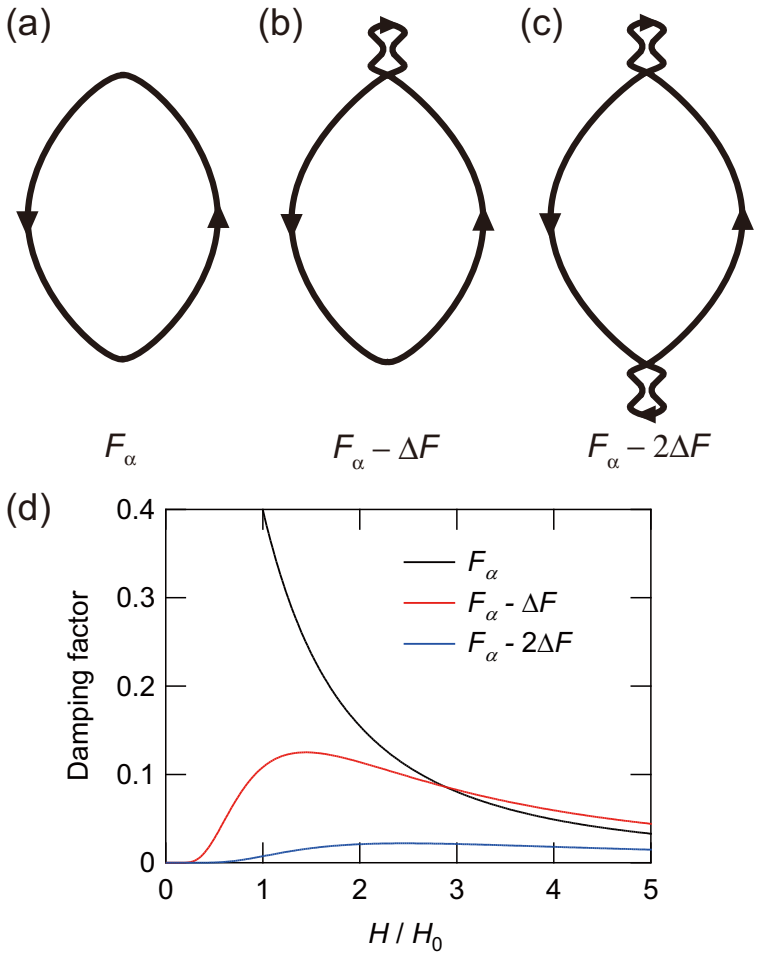

Figure 4.16: Possible magnetic breakdown at high magnetic fields for $\boldsymbol{H} \perp [001]$. (a) Cyclotron orbit for the α hole band without magnetic breakdown. Relative probability of performing this orbit is given by $(1-p)^2$, where $p = \exp(-H_0/H)$ is the breakdown probability. (b) 'Figure-eight' breakdown orbit through the α hole and 'hourglass' electron pockets. (c) Orbit with two sets of magnetic breakdown near the two poles of the α band. (d) Damping factors for these three orbits which are calculated from the breakdown probability are plotted against field normalized by the breakdown field H_0.

4.4.6 Nematic electronic structure inferred from cyclotron resonance

In-plane mass anisotropy of the α hole band

Now we focus on the signature of the FS that provides a key to understanding the HO. The most unexpected and important result is that the sharpest line D arising from the α hole pocket is clearly split into two lines with nearly equal intensities near the [110] direction (Figs. 4.12(a), (c), (f) and 4.13). This splitting in the α hole pocket is hardly explained from the calculated FS structure in the antiferromagnetic phase.

One may argue that some small warping of FS shape gives rise to the appearance of an additional extremal orbit for particular angles, which can result in the splitting. However, such a scenario is highly unlikely because of the following reasons. First, quantum oscillation measurements clearly indicate that the number of extremal orbits in the [110] direction remains the same as that in [100] direction [33, 108]. This argues against that the additional orbit appears only near the [110] direction. Second, the band-structure calculation indicates that α pocket is nearly spherical, which is supported by the quantum oscillations experiments [33, 34] that reveal almost angle-independent oscillation frequency for this band. Third, the fact that the integrated intensity of the split line D' is nearly equal to that of D line in a wide range of angle (Figs. 4.12(a), (c) and (f)) suggests that both CR lines arise from the orbits with nearly equal FS cross sections, which is at odds with the warping scenario. Therefore we infer that the observed splitting of the CR line D results from a peculiar mass structure in the HO phase.

The observed splitting of the sharpest CR line D near the [110] direction can be naturally explained by the emergence of the heavy spots in the α band along [110] as depicted in Fig. 4.17. One may consider such a twofold mass anisotropy if the system breaks the fourfold symmetry as suggested by the magnetic torque experiments [27]. The twofold symmetry also leads to the formation of domains with different nematic directions, which can be called as [110] and [1$\bar{1}$0] domains as shown in the insets of Fig. 4.17(a). In large crystals containing these two domains we expect to have two different orbits with different cyclotron masses near the [110] and equivalent directions. This can explain the observed splitting of the cyclotron mass near [110]. The robustness against field tilting can also be explained because the cyclotron orbit for one of the domains always goes through the heavy spots as shown by the red arrow in the inset of Fig. 4.17(a).

The fact that the quantum oscillation frequency for the α band does not show the corresponding splitting for tilted fields indicates that the FS shape does not show significant breaking of fourfold symmetry but only mass structure strongly breaks the rotational symmetry. This suggests that the twofold symmetry is related to the correlation effect, which modifies mainly the curvature of band dispersion near the Fermi energy (Fig. 4.17(b)).

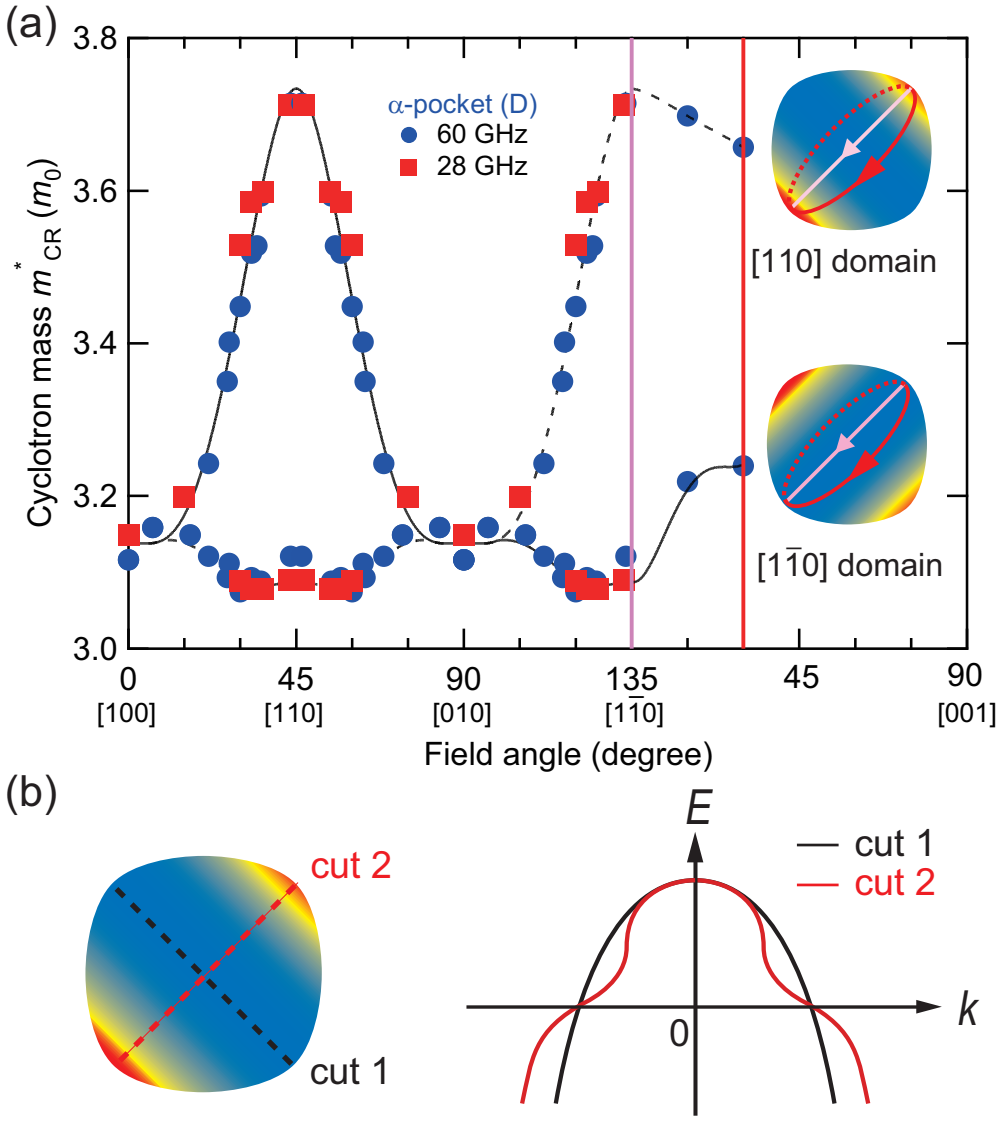

Figure 4.17: Structure of the cyclotron mass $m^*_{\rm CR}$ of the α band. (a) $m^*_{\rm CR}$ of the α band as a function of the field angle at 28 and 60 GHz. We use the data for $0 \leq \phi < 45°$ and $0 \leq \theta \leq 30°$ and symmetrize them for other angles. The solid and dotted lines are the guides for the eyes representing two domains. Insets illustrates the anisotropic mass distribution in the spherical α band for the two domains elongated along the [110] and [1$\bar{1}$0] directions. Red area represents heavy spots. For each domain, two orbits for $\phi = -45°$, $\theta = 0°$ (pink) and $\phi = -45°$, $\theta = 30°$ (red) are depicted. (b) For the [110] domain schematic dispersion curves are shown along the two directions.

Enhanced inelastic scattering rate at the heavy spots

A close look at the split resonance lines in Fig. 4.18 reveals that the FWHM for the heavier line (at higher field) is always larger than the lighter line in our measurement temperature range. We note that the integrated intensities for these two CR lines are almost identical, which is reproducible when the field direction is rotated by $\sim 90°$. This implies that the two domains have almost identical volumes in the large crystal used in this study. We also find that the data taken after the field cooling condition at 12 T remains unchanged, which is consistent with the previous torque experiments [27]. These results suggest that the domains are pinned by the underling lattice conditions.

An important result is that the magnitude of $\omega\tau$ estimated from the width of the Lorentzian fits is smaller for the heavier resonance line. It has been demonstrated [117] that the elastic impurity scattering time is longer for heavier band, because of the impurity limited mean free path at very low temperatures. In our case, however, the opposite trend has been observed, implying that the inelastic scattering rate $1/\tau$ is enhanced for the heavier cyclotron orbit. This is supported by the higher temperature data (Fig. 4.18(b)), where the FWHM of the heavier CR line shows more broadening, indicating stronger temperature dependence of inelastic scattering rate $1/\tau(T)$ near the heavy spots.

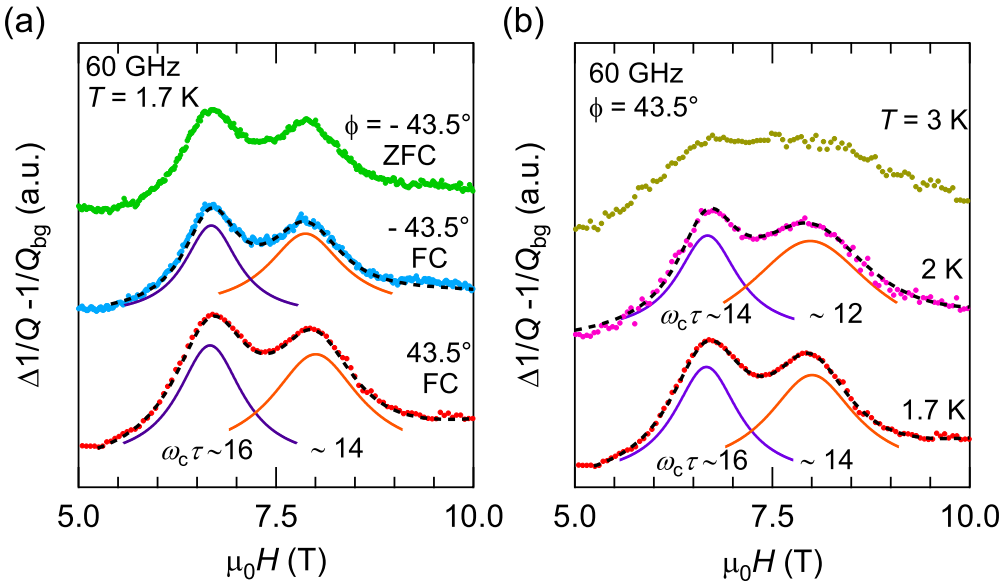

Figure 4.18: Split CR lines for the α band near the [110] direction. (a) Field dependence of $\Delta 1/Q - 1/Q_{\rm bg}$ near the resonance line D at 60 GHz for $\phi = \pm 43.5°$. The data taken after the zero-field cooling (ZFC) and field-cooling (FC) procedures are identical within experimental error. The FC data are fitted by the two Lorentzian functions (dashed lines) with different $\omega_c\tau$ values (solid lines). Each curve is shifted vertically for clarity. (b) The same plot for $\phi = 43.5°$ at three different temperatures.

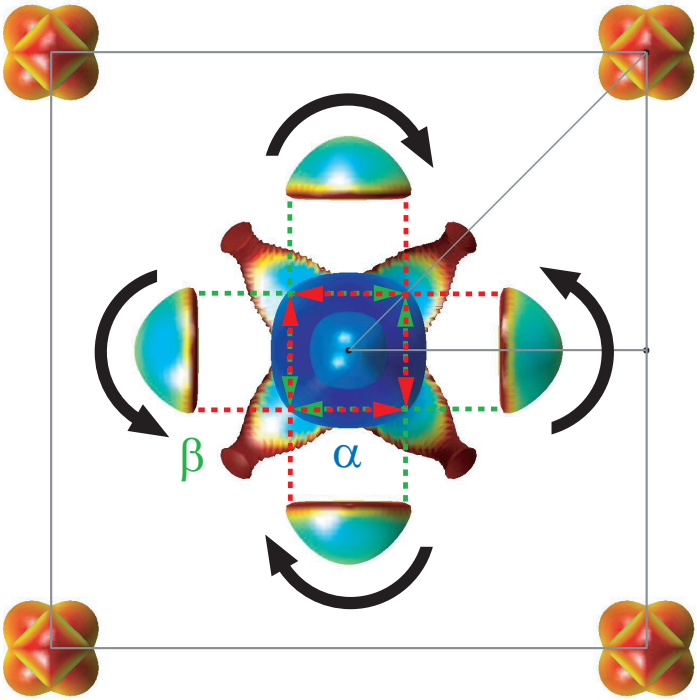

Figure 4.19: Schematic Fermi surface viewed along the [001] direction, showing possible changes due to the fourfold rotational symmetry breaking. In a [110] nematic state, the four hemispherical β pockets may rotate or elongate towards each directions indicated by the black arrows. This symmetry breaking changes the nesting conditions between the β and α pockets connected with the incommensurate wave vectors $(\pm 0.4, 0, 0)$ and $(0, \pm 0.4, 0)$ (dashed arrows), and the interband quasiparticle scattering rates shown by the green and red arrows become non-equivalent.

To discuss possible origins of the enhanced inelastic scattering at the heavy spots, it is important to consider the interband scattering between the Fermi surface points connected with particular wave vectors characteristic to the hidden-order phase. It has been shown from the neutron scattering experiments [30, 31] that the excitations at the commensurate $\boldsymbol{Q}_C = (1, 0, 0) = (0, 0, 1)$ and incommensurate $\boldsymbol{Q}_{IC} = (0.4, 0, 0)$ wave vectors are important in the hidden-order phase of URu_2Si_2. As schematically shown in Fig. 4.19, there are parts of α and β pockets connected approximately by $\boldsymbol{Q}_{IC}$ [38]. In the HO phase, the FS has twofold symmetry (rather than fourfold tetragonal symmetry) along the [110] direction, and the four β pockets can be slightly rotated (or elongated) along this direction. This leads to an imbalance in the interband interactions as depicted by the green and red dashed arrows in Fig. 4.19. This imbalance may enhance the inelastic scattering at the two of the four corners of the α hole pocket, generating the hot spots along the [110] (or $[\bar{1}10]$) direction in the α sheet as revealed in the present CR experiments.

4.5 Summary

We have shown that the observation of cyclotron resonance (CR) in the hidden order (HO) states of URu_2Si_2 provides useful information of the quasiparticle mass and scattering rate. We have determined the angle-dependent mass structure, which is compared with the band-structure calculations assuming the antiferromagnetic state. We were able to assign the three CR lines with strong intensities with the main Fermi surface pockets, from which a reasonable estimate of electronic specific heat coefficient can be obtained. In the sharpest CR line corresponding to the hole α pocket, we observed anomalous splitting near the [110] direction, which is not expected in the calculations for antiferromagnetic state. This splitting is found to be robust against the field tilting from the basal plane, which clearly indicates that the CR splitting has a different origin from the threefold splitting of the quantum oscillation frequency observed only near the in-plane direction. By considering the Fermi-surface structure we propose the magnetic breakdown at high fields as a possible origin of the quantum oscillation splitting. The CR splitting can be naturally explained if we consider the twofold in-plane anisotropy of the mass and the formation of micro-domains, which is consistent with the broken rotational fourfold symmetry suggested by the magnetic torque experiments [27]. Recent nuclear magnetic resonance (NMR) experiments have reported the peculiar in-plain anisotropy of the Si NMR line width, which also supports the twofold anisotropy elongated along the [110] direction [28]. Moreover, high-resolution synchrotron X-ray measurements discussed in previous chapter have revealed evidence for structural change from the tetragonal $I4/mmm$ to orthorhombic $Fmmm$-type symmetry [118], which is also consistent with the broken fourfold symmetry. From the scattering rate analysis, we find that the anisotropic in-plane mass structure involves the hot spots with heavy mass and large scattering rate, which suggests strong momentum dependence of electron correlations due to interband scattering.

Chapter 5

Cyclotron resonance in the superconducting state in URu_2Si_2

5.1 Introduction

Cyclotron resonance in the superconducting phase is currently an exciting area of investigation theoretically and experimentally. It is thought to be more difficult to observe cyclotron resonance in superconducting phase than in normal state. This is because the quasiparticles are scattered not only by static defects and impurities, but also by vortices. Recent development of high quality crystals of some samples including URu_2Si_2 leads the observation of the quantum oscillation in the superconducting state, where the amplitudes of the quantum oscillation actually show reduction at superconducting transition. On the other hand, the direct observation of cyclotron resonance in the mixed state scarcely have been observed. One of the reasons is that microwave energy absorbed by carrier (corresponding to $\sim$ 1.5 K) is very high, which becomes difficult to require the cyclotron condition: the Landau levels should be larger than the thermal broadening ($\hbar\omega_{\rm CR} > k_B T$). The other is microwave penetration depth is usually short. We therefore make ^{3}He microwave cavity, that can cool to $\sim$ 700 mK and study the cyclotron resonance study on the superconducting phase of URu_2Si_2.

5.1.1 Cyclotron motion in the mixed state

In the type-Ⅱ superconductors for a range of applied fields ($H_{c1} < H < H_{c2}$), the magnetic flux (vortex) penetrates the samples and form Abrikosov lattice. Ohkuni *et al* suggested quantum oscillation experiments can be explained by the quasiparticles which tunnel into the normal and superconducting region to perform the cyclotron orbit [33]. A schematic picture of Abrikosov lattice of vortices and the cyclotron orbit for branch α in URu_2Si_2 observed by dHvA experiments is shown Fig. 5.1. Quasiparticles are scattered at the boundary between the normal and superconducting regions, called Andreev reflection

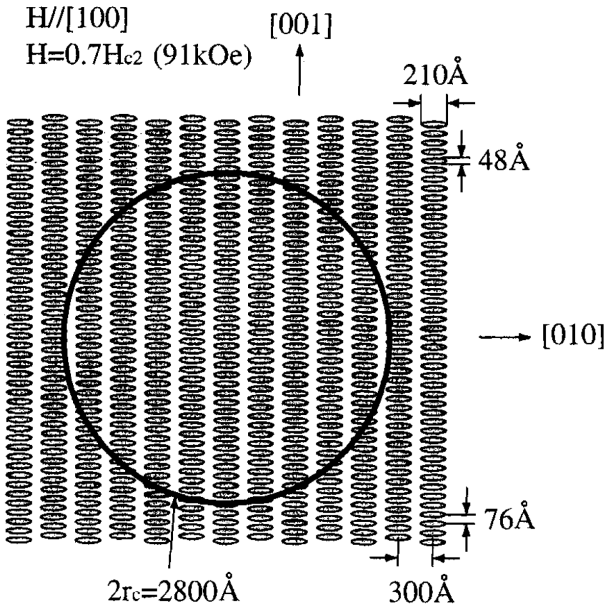

Figure 5.1: Abrikosov lattice and the cyclotron orbit for branch α for the field along [100] at $H = 0.7H_{c2}$ in URu_2Si_2 [33]. Vortices are elliptic due to the anisotropy of the coherence length.

5.1.2 Kohn's theorem in the superconducting state

Kohn theorem in normal state is shown in previous chapter, which states that the only resonance in the system of electrons should occur at the frequency ω_{CR} irrespective of their mutual interaction. It is still controversial whether the Kohn theorem works in the superconducting phase. H. D. Drew *et al* suggested the Kohn theorem can be applied to the type-I superconductors and type-Ⅱ superconductors at low fields ($H < H_{c1}$) [119]. On the other hand, in the mixed state N. B. Kopnin *et al* suggested the resonant frequency is not coincident exactly with ω_{CR} [120–122]. This Kohn theorem violation is due to that there are two different kinds of interacting charge carriers, that is to say, the normal quasiparticles and superconducting electrons, which breaks the Galilean invariant system.

5.2 Purpose of the cyclotron resonance study in the superconducting state

Another important aspect of URu_2Si_2 is that the hidden order phase hosts the unconventional superconducting phase below the transition temperature $T_{SC} = 1.4\,K$ at ambient pressure. The cyclotron mass m^*_{CR} in the superconducting state has also been a subject of theoretical debate [119–122]. By considering the ac dynamics of superconducting vortices, a theory predicts the violation of the Kohn's theorem and a peculiar temperature dependence of the resonance frequency in clean type-II superconductors [120]. Experimentally, however, this point has not yet studied mainly because the observation of cyclotron resonance in the superconducting state is difficult due to the microwave high energy and the limitation of microwave penetration depth which is usually short. We therefore made ^{3}He microwave cavity and observed cyclotron in the superconducting phase of URu_2Si_2. The temperature dependence of the cyclotron mass tells us whether the Kohn theorem works in the superconducting state. Another useful information on the superconducting state is obtained by the scattering rate estimated from the full width half maximum (FWHM) of the cyclotron resonance peak. In URu_2Si_2 sample, dHvA measurements show the Dingle temperature which is proportional to the scattering rate increased in the mixed state. On the other hand, thermal conductivity experiments revealed an unexpected enhancement of the quasiparticle mean free path below the melting transition, which implies that the quasiparticles are scattered less by the vortex lattice than liquid due to the formation of a novel Bloch-like state by the periodic vortex lattice. These results are controversial, so the scattering time estimated from cyclotron resonance can indicate important clue. Furthermore, we measure the surface impedance experiments under same setting of cyclotron resonance, which tells us whether the URu_2Si_2 sample actually shows the superconducting transition.

5.3 Experiments

5.3.1 Sample

Single crystals of URu_2Si_2 grown by the Czochralski pulling method in a tetra-arc furnace are provided by Dr. Yoshinori group at Japan Atomic Energy Agency. Figure shows the temperature dependence of the resistivity, resulting in exceptionally low residual resistivity $\rho_0 \simeq 0.5\,\mu\Omega$cm and large residual resistivity ratio of 670. It attest the highest quality currently achievable.

5.3.2 Methods

Our experiments are performed by OFHC copper cavity resonator in the TE_{011} mode. We analyze the Q-factor and resonant frequency by cavity perturbation method. Microwaves are coupled to the probe through a small circular coupling hole on the top of the cavity. We set the sample at the center of the cavity where the magnetic field is maximum and the electric field is nearly zero. This setting is same for cyclotron resonance in the hidden order state.

We used Hewlett-Packard 83640A synthesized sweeper as a microwave generator. The input signal is carried to the cavity via the coaxial cable or waveguide, and the output is read by Agilent 8757D scalar network analyzer, where the difference between the output and the reference signals is picked up. We can extract the resonant frequency f and the quality factor Q from the full frequency width at half-maximum Γ. Lakeshore model 340 were used to control each temperature of the sample and cavity.

45 GHz cavity

Fig. 5.2 shows the schematic picture of the 45 GHz cavity and its sample holder. The 45 GHz cavity is designed by Kosuke Ikada. For the TE_{011} mode, the resonant frequency and the quality factor of the Cu cavity are operated with $f \sim 45$ GHz and $Q \sim 40000$, respectively, in the absence of samples. The sample is placed at the center of the cavity and mounted on a sapphire rod with a tiny dot of Apiezon N grease. The sapphire rod is thermally disconnected with the cavity, but in contact with the block of copper which is thermally weakly coupled to the ^{3}He pot. In this system, we can cool the sample to 700 mK. The thermometer and heater are installed on the block of copper and we can control the temperature of the sample within ± 1 mK. This is the so-called hot finger technique [111, 112] and known to have high precision to measure the temperature dependence of both the surface resistance R_s and the surface reactance X_s even in small single crystals. The wires of the thermometer and heater pass through the stainless-steel pipe, whose one edge is covered with stycast 2850FT for maintaining vacuum inside the cavity, and reach the room-temperature apparatus.

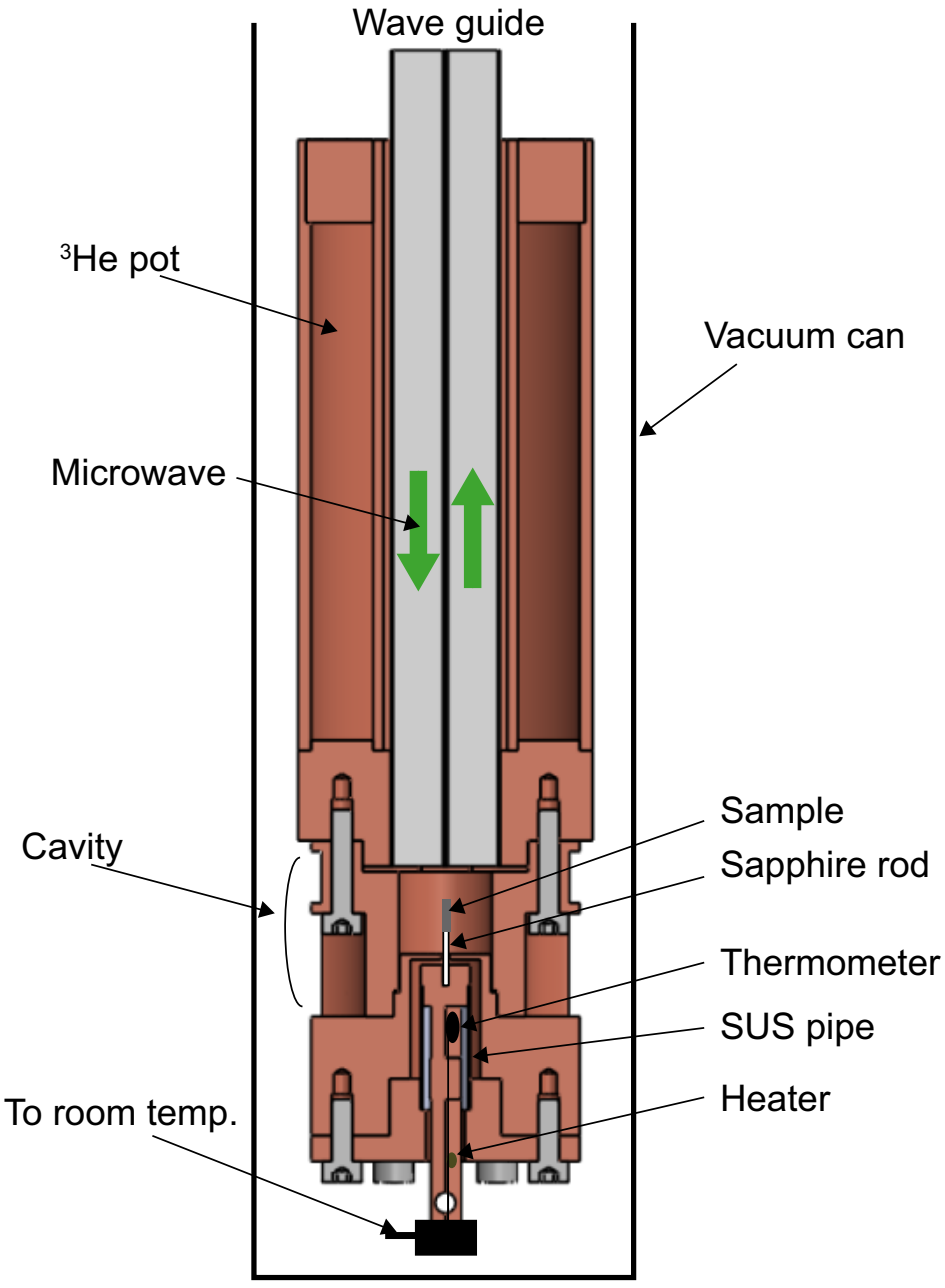

Figure 5.2: A schematic picture of 45 GHz cavity. This cavity has ^{3}He pot, which can the sample to about 700 mK.

5.4 Results

5.4.1 Temperature dependence of surface impedance

Next we discuss the results in the superconducting state, which have been obtained by using 45-GHz cavity with ^{3}He pot. To check the superconducting transition we measure the temperature dependence of the surface impedance ($Z_s = R_s + \mathrm{i}X_s$) at zero and finite magnetic fields. In our condition that the skin depth δ is smaller than sample dimensions, the change in the microwave power dissipation $\Delta 1/Q$ and the frequency shift Δf are proportional to the surface resistance R_s and the change of the surface reactance ΔX_s, respectively [111]. In many superconductors, the normal-state microwave electrodynamics is described by the Hagen-Rubens limit $\omega\tau \ll 1$, in which the surface resistance and reactance have the simple form

$$R_s = X_s = \sqrt{\frac{\mu_0 \omega \rho}{2}} = \frac{\mu_0 \omega \delta}{2}. \tag{5.1}$$

However, in the present case $\omega\tau$ becomes large and the Hagen-Rubens limit is not satisfied at low temperatures. Indeed the temperature dependence of X_s deviates from that of R_s even above T_{SC}, as shown in Fig. 5.3(a). Similar deviations have been observed, for example, in the Kondo semiconductor CeNiSn, where the gap formation reduces the scattering leading to $\omega\tau > 1$ at low temperatures [123].

In the SC state below T_{SC}, we clearly observe the reduction of R_s as well as the enhancement of X_s (Fig. 5.3(a)). The latter enhancement is not usually seen in superconductors, because X_s in the SC state can be approximately given by the magnetic penetration depth λ as

$$X_s = \mu_0 \omega \lambda, \tag{5.2}$$

when λ is much shorter than the skin depth δ. In URu_2Si_2, however, the small number and heavy mass of carriers result in very long penetration depth $\sim 1\,\mu$m [124], which is longer than the skin depth $\sim 0.24\,\mu$m at 45 GHz in our ultraclean crystals. Under magnetic fields, we observe essentially similar behaviours in the temperature dependence of Z_s (see Figs. 5.3(b) and (c)). The deviation between $R_s(T)$ and $X_s(T)$ is observed in the normal state, which is enhanced in the SC state. Previous measurements of electrical and thermal conductivities in fields [73] have provided evidence for the existence of extended region of vortex liquid state, where the resistivity is still finite even in the SC state below the mean-field transition temperature T_{SC}. In the vortex solid state below the melting temperature T_m, the resistivity becomes zero and the thermal conductivity shows an enhancement [73]. By a comparison with the reported vortex phase diagram (see Fig. 5.3(d)), we find that the deviation between $R_s(T)$ and $X_s(T)$ becomes much enhanced below T_m in the vortex solid state.

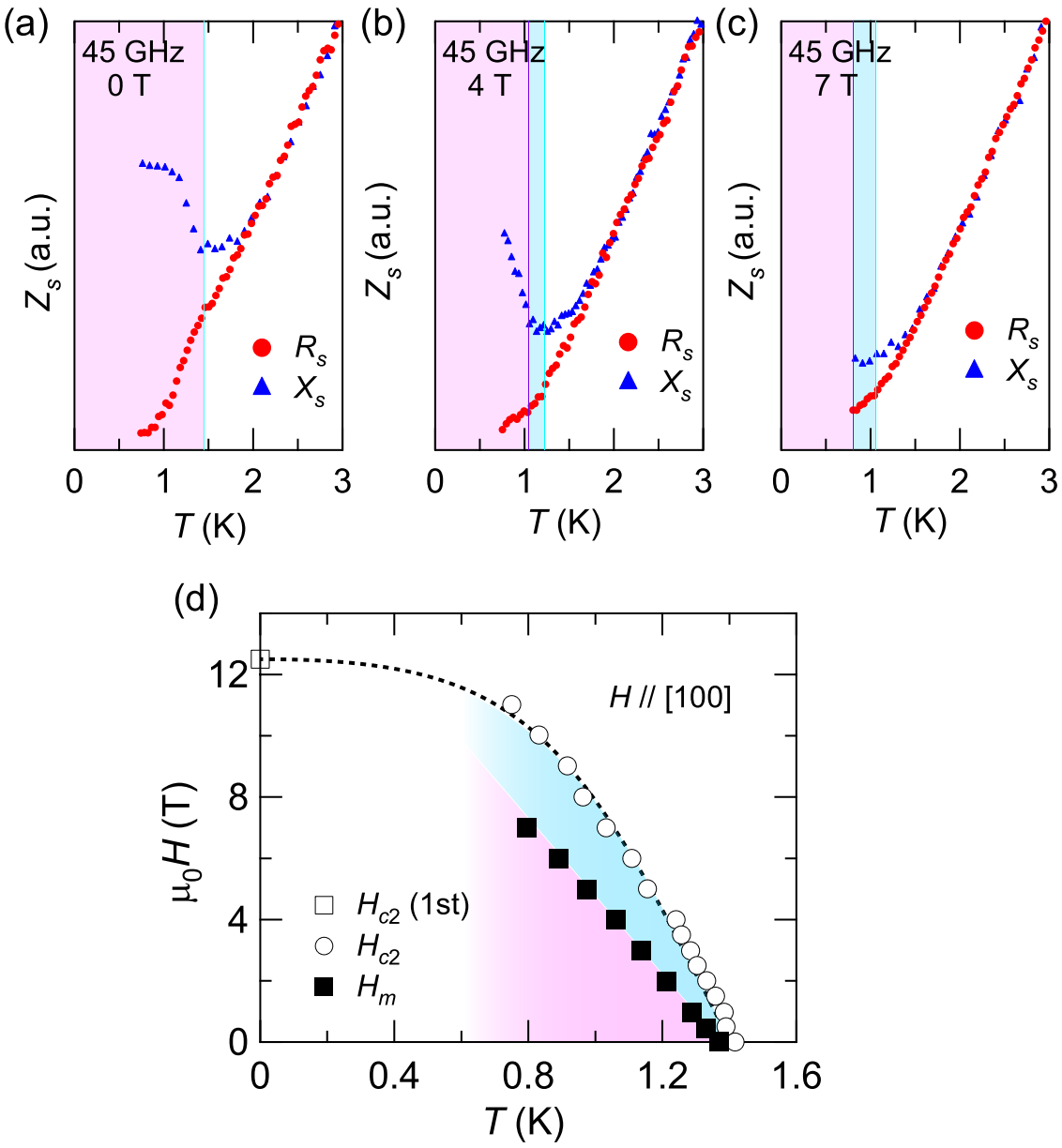

Figure 5.3: (a) Temperature dependence of surface resistance R_s and surface reactance X_s at 45 GHz in URu_2Si_2 at zero field. Shaded region represents the superconducting state below T_{SC}. (b), (c) Similar plots for data taken under magnetic fields $\boldsymbol{H} \parallel [100]$. (d) Field-temperature phase diagram for $\boldsymbol{H} \parallel [100]$ taken from Ref. [73]. In (a)-(c), the corresponding temperature regions for the vortex liquid (blue shade) and vortex solid (red shade) states are also indicated.

5.4.2 Cyclotron mass in the superconducting state

The field dependence of $\Delta 1/Q$ for $\boldsymbol{H} \parallel [100]$ at 45 GHz shows multiple CR lines, which persist down to the lowest temperature at 0.7 K (Figs. 5.4(a) and (b)). At this temperature 0.7 K, the upper critical field H_{c2} and vortex-lattice melting field H_m for $\boldsymbol{H} \parallel [100]$ are 11 and 7 T respectively [73]. Thus we focus on the resonance lines at low fields, labeled as D, E, F, and G. The surface impedance results in Fig. 5.3 clearly indicate that we cover the field and temperature range deep in the SC state, and thus for these lines the observed clear peaks in the SC state below T_{SC} can be considered as the first observation of the CR in the SC phase of heavy-fermion materials.

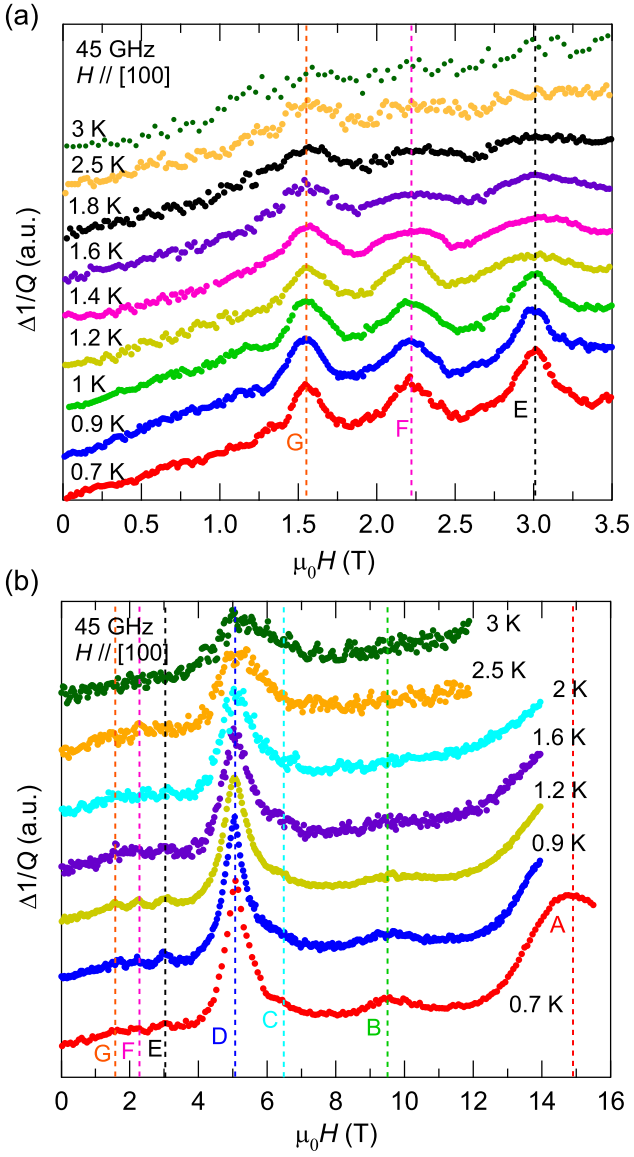

Figure 5.4: Observation of cyclotron resonance in the superconducting phase of URu_2Si_2. (a) Field dependence of the change $1/Q$ at several temperatures for $\boldsymbol{H} \parallel [100]$.

The temperature dependence of the cyclotron masses m^*_{CR} for these lines, which are determined by the resonance fields, is plotted in Fig. 5.5. Within experimental error, the masses are temperature independent, and we find that they do not exhibit any noticeable change between the HO and SC phases. Theoretically, in clean type-II superconductors, it has been shown [120] that the presence of superconducting and normal carriers in the vortex states leads to the violation of Kohn's theorem, and the temperature dependence of the superconducting carrier number results in a peculiar temperature dependence of the cyclotron frequency. In the present case, however, such temperature dependence is not observed. One possible reason for this difference is that in this multiband system, the Kohn's theorem is already violated in the normal state above T_{SC}, which may alter the description of CR in the vortex state. Further studies are necessary for the understanding of CR in heavy-fermion and multiband superconductors.

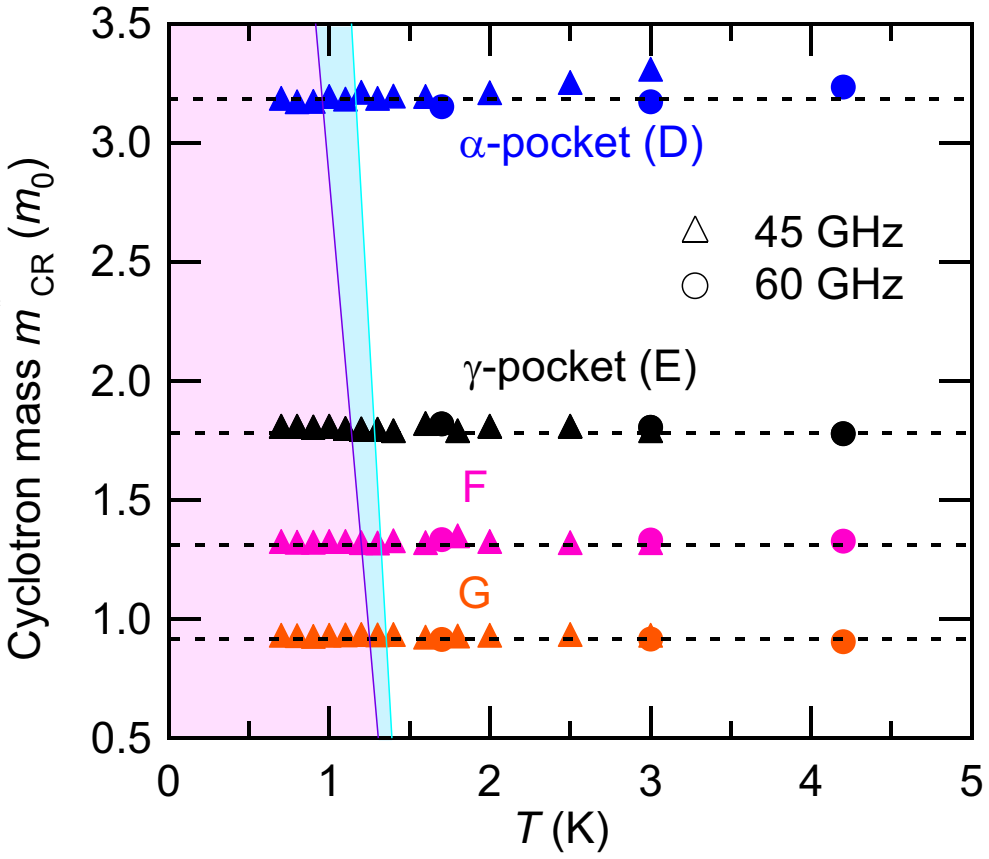

Figure 5.5: The temperature dependence of the cyclotron masses at 45 and 60 GHz for CR lines D-G. Corresponding vortex liquid (blue shade) and vortex solid (red shade) states for 45 GHz are determined from the phase diagram in Ref [73].

5.4.3 Temperature dependence of the scattering rate

A close look at the temperature dependence of the resonance line shape in Figs. 5.4(a) and (b) finds that the FWHM of the CR lines become broader with increasing temperature. We analyze the data by the Lorentzian fits to extract the temperature dependence of the quasiparticle scattering rate $1/\tau$, which is shown in Fig. 5.6. In the normal state above $T_{\rm SC}$ the scattering rate roughly follows T-linear dependence, which suggests the deviation from the standard Fermi-liquid theory of metals. Such non-T^2 dependence of scattering can also be found in the transport measurements of URu_2Si_2 [12, 125].

In the SC state below $T_{\rm SC}$, we observe that the scattering rate is suppressed not at $T_{\rm SC}$, but below the vortex-lattice melting transition temperature T_m for all four lines D-G (Figs. 5.6(a)-(d)). Such a suppression below T_m is consistent with the reported enhancement of thermal conductivity below T_m, and provides further evidence that the vortex solid state has much less scattering than the vortex liquid state. In very clean systems the vortices form a regular lattice in the solid state, which can act as a periodic potential for quasiparticles. In such a case, the formation of a Bloch-like state may be expected, where the quasiparticle scattering is reduced compared with the vortex liquid state having more disordered potentials. Thus our observation provides a strong support for the formation of the quasiparticle Bloch state in vortex-lattice state of clean superconductors.

We also note that the dHvA measurements [33] have shown that the Dingle temperature T_D, which is proportional to the scattering rate, increases when the field is reduced below the upper critical field at very low temperatures $\sim 35\,$mK. In this low temperature range, the upper critical field is suggested to be of first order [29], and the boundary between the vortex liquid and solid states is not fully resolved. This result can be explained by the enhanced scattering due to the Andreev reflection occurred at the boundary between the SC and normal (vortex core) regions in the vortex liquid state just below H_{c2}. This implies that there is sizeable vortex liquid region even in the low-temperature limit, where thermal fluctuations vanish. Such a possible quantum vortex liquid state, where quantum fluctuations melt the vortex lattice, has been suggested in organic and cuprate superconductors [126, 127]. It deserves further studies to determine the complete phase diagram down to the low temperature limit.

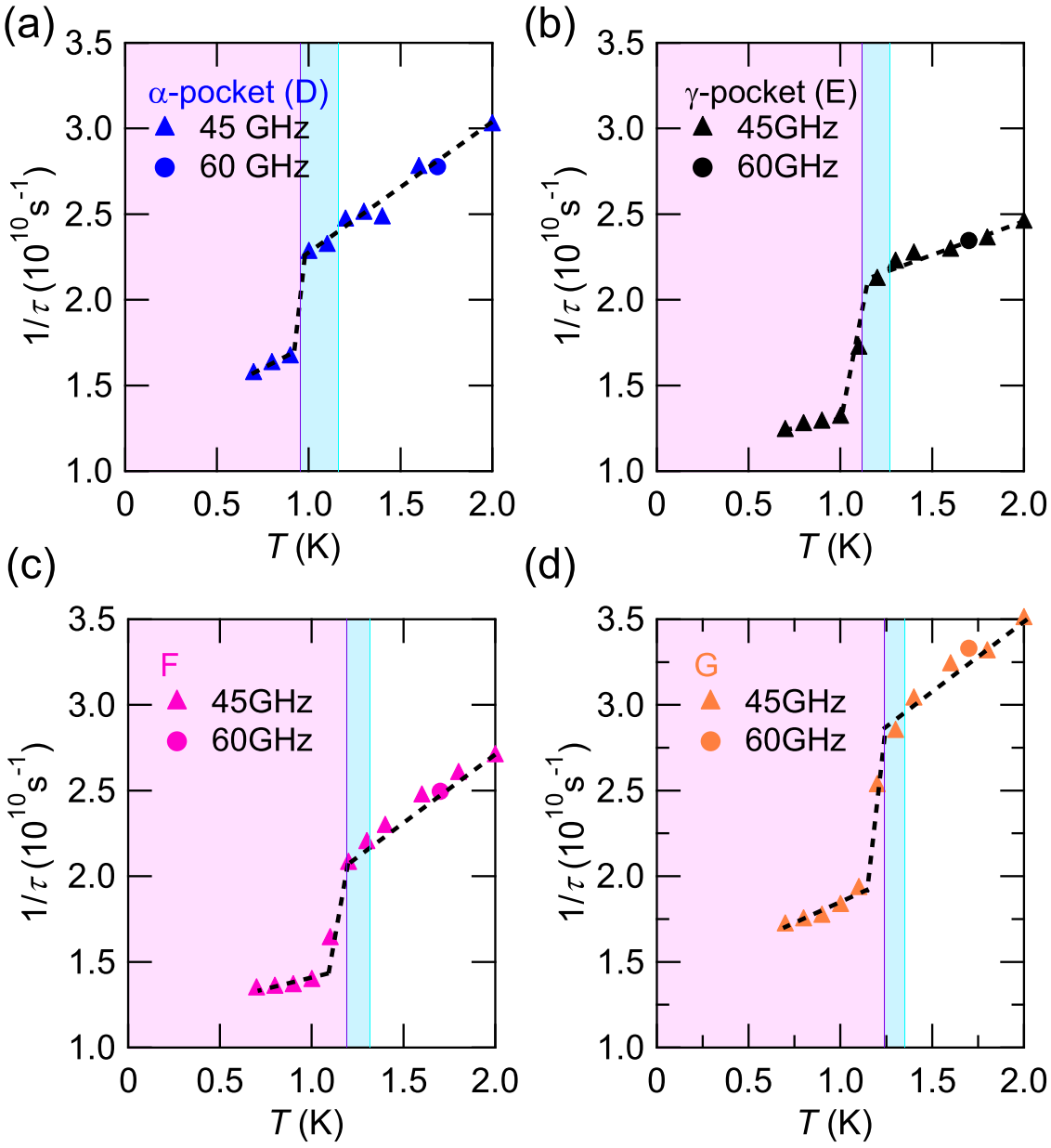

Figure 5.6: Temperature dependence of the scattering rate $1/\tau$ extracted from the CR line width at 45 and 60 GHz for CR lines D (a), E (b), F (c), and G (d). Corresponding vortex liquid (blue shade) and vortex solid (red shade) states for 45 GHz are determined from the phase diagram in Ref. [73].

5.5 Summary

In the SC phase embedded in the HO phase, we presented the first observation of cyclotron resonance in the vortex states. Contrary to the proposed temperature dependence, we find that the mass does not show any significant change below T_c. We rather find that the scattering rate at low temperatures exhibits characteristic temperature dependence; it shows non-Fermi liquid-like quasi T-linear dependence followed by a sudden decrease below the vortex-lattice melting transition temperature, which has been determined by the resistivity measurements [73]. This supports the formation of a coherent quasiparticle Bloch state in the vortex lattice phase.

Chapter 6

Conclusion

URu_2Si_2 is a heavy fermion compound which exhibits a "hidden order" transition at 17.5 K, whose order parameter remains unclarified despite experimental and theoretical efforts for more than a quarter century. The hidden order transition accompanies a huge amount of entropy loss, but neither magnetic ordering nor structural ordering has been observed. The key to the nature of hidden order lies in understanding which symmetry is being broken. Recent magnetic torque measurements [27] and NMR experiments [28] reveal the crystal C_4 rotational symmetry in the tetragonal URu_2Si_2 is broken below the hidden order phase transition. This newly suggested rotational symmetry breaking has raised several theoretical proposals, and calls for further experimental verifications by using other techniques.

Here, we report on the first observation of lattice deformation at zero field, which pins down the symmetry of the hidden order of URu_2Si_2. Our synchrotron X-ray crystal-structure analysis reveals tiny but finite orthorhombic distortion of the order of 10^{-5} (or lattice constant change less than 100 fm). Unlike previous studies, we focus on a high-angle (880) Bragg diffraction of the body-centered tetragonal crystal structure ($I4/mmm$), which shows a clear peak split below $T_{\rm HO}$, demonstrating a transformation to the orthorhombic $Fmmm$ structure. The smallness of the lattice change implies that the transition is driven by the electronic ordering which distorts the lattice owing to a small electron-lattice coupling. It also makes the detection quite difficult without high-resolution experiments, which explains why the broken symmetry has been hidden for so long. Small orthorhombic symmetry-breaking distortion sets in at $T_{\rm HO}$ with a jump, uncovering the weakly first-order nature of the hidden-order transition. This distortion is observed only in ultrapure sample, implying highly unusual coupling nature between electronic nematicity and underlying lattice.

Such four-fold rotational symmetry breaking is also observed by cyclotron resonance experiments. We report the first observation of the cyclotron resonance in ultrapure URu_2Si_2 crystals, which allows the full determination of the angle-dependent electron-mass structure of the main Fermi surface sheets with high precision. In the sharpest cyclotron resonance line corresponding to the hole α pocket, we observed anomalous splitting near the [110] direction, which is not expected in the calculations for antiferromagnetic state. The cyclotron resonance splitting can be naturally explained if we consider the twofold in-plane anisotropy of the mass

and the formation of micro-domains, which is consistent with the broken rotational fourfold symmetry.

The broken fourfold symmetry gives strong constraints on the symmetry of the order parameter in the hidden order phase. In the symmetry classification of the multipole order this is consistent with the two-dimensional E representations. Along this line, rank-2 quadrupole with E^+ symmetry, and rank-3 octupole and rank-5 dotriacontapole with E^- symmetry have been theoretically proposed, where the superscript + or − denotes the parity with respect to time reversal. More exotic nematic or hastatic states with and without time reversal symmetry breaking have also been proposed, which are also consistent with the broken fourfold symmetry. To pin down the genuine hidden order parameter, the next important step would be to identify whether time reversal symmetry is broken or not.

Another important aspect of URu_2Si_2 is that the hidden order phase hosts the unconventional superconducting phase below the transition temperature $T_{SC} = 1.4$ K at ambient pressure. In the superconducting phase embedded in the hidden order phase, we presented the first observation of cyclotron resonance in the vortex states. We found that while the cyclotron mass does not show any temperature dependence, the scattering rate shows a rapid suppression below the vortex lattice melting transition temperature. This provides evidence for the formation of quasiparticle Bloch state in the vortex lattice state.

References

[1] S. Doniach, Physica B **91**, 231 (1977).

[2] G. R. Stewart, Z. Fisk, J. O. Willis, and J. L. Smith, Phys. Rev. Lett. **52**, 679 (1984).

[3] C. Geibel, C. Schank, S. Thies, H. Kitazawa, C. D. Bredl, A. Bohm, M. Rau, A. Grauel, R. Caspary, R. Helfrich, U. Ahlheim, G. Weber, and F. Steglich, Z. Phys. B **84**, 1 (1991).

[4] C. Geibel, S. Thies, D. Kaczorowski, A. Mehner, A. Grauel, B. Seidel, U. Ahlheim, R. Helfrich, K. Petersen, C. D. Bredl, and F. Steglich, Z. Phys. B **83**, 305 (1991).

[5] S. S. Saxena, P. Agarwal, K. Ahilan, F. M. Grosche, R. K. W. Haselwimmer, M. J. Steiner, E. Pugh, I. R. Walker, S. R. Julian, P. Monthoux, G. G. Lonzarich, A. Huxley, I. Sheikin, D. Braithwaite, and J. Flouquet, Nature **406**, 587 (2000).

[6] D. Aoki, A. Huxley, E. Ressouche, D. Braithwaite, J. Flouquet, J.-P. Brison, E. Lhotel, and C. Paulsen, Nature **413**, 613 (2001).

[7] T. Akazawa, H. Hidaka, T. Fujiwara, T. C. Kobayashi, E. Yamamoto, Y. Haga, R. Settai, and Y. Onuki, J. Phys.: Condens. Matter **16**, L29 (2004).

[8] N. T. Huy, A. Gasparini, D. E. de Nijs, Y. Huang, J. C. P. Klaasse, T. Gortenmulder, A. de Visser, A. Hamann, T. Gorlach, and H. v. Lohneysen, Phys. Rev. Lett. **99**, 067006 (2007).

[9] T. T. M. Palstra, A. A. Menovsky, J. van den Berg, A. J. Dirkmaat, P. H. Kes, G. J. Nieuwenhuys, and J. A. Mydosh, Phys. Rev. Lett. **55**, 2727 (1985).

[10] M. B. Maple, J. W. Chen, Y. Dalichaouch, T. Kohara, C. Rossel, M. S. Torikachvili, M. W. McElfresh, and J. D. Thompson, Phys. Rev. Lett. **56**, 185 (1986).

[11] W. Schlabitz, J. Baumann, B. Pollit, U. Rauchschwalbe, H. M. Mayer, U. Ahlheim, and C. D. Bredl, Z. Phys. B **62**, 171 (1986).

[12] T. D. Matsuda, E. Hassinger, D. Aoki, V. Taufour, G. Knebel, N. Tateiwa, E. Yamamoto, Y. Haga, Y. Ōnuki, Z. Fisk, and J. Flouquet, J. Phys. Soc. Jpn. **80**, 114710 (2011).

[13] T. D. Matsuda, D. Aoki, S. Ikeda, E. Yamamoto, Y. Haga, H. Ohkuni, R. Settai, and Y. Ōnuki, J. Phys. Soc. Jpn. **77**, Suppl. A, 362 (2008).

[14] N. P. Butch, J. R. Jeffries, S. Chi, J. B. Leao, J. W. Lynn, and M. B. Maple, Phys. Rev. B **82**, 060408 (2010).

[15] F. Bourdarot, A. Bombardi, P. Burlet, M. Enderle, J. Flouquet, P. Lejay, N. Kernavanois, V. P. Mineev, L. Paolasini, M. E. Zhitomirsky, and B. Fak, Physica B **359**, 986 (2005).

[16] H. Amitsuka, K. Matsuda, I. Kawasaki, K. Tenya, M. Yokoyama, C. Sekine, N. Tateiwa,. T.C. Kobayashi, S. Kawarazaki, and H. Yoshizawa, J. Magn. Magn. Mater. **310**, 214 (2007).

[17] H. Amitsuka, K. Matsuda, M. Yokoyama, I. Kawasaki, S. Takayama, Y. Ishihara, K. Tenya, N. Tateiwa, T. C. Kobayashi, and H. Yoshizawa, Physica B **403**, 925 (2008).

[18] P. G. Niklowitz, C. Pfleiderer, T. Keller, M. Vojta, Y.-K. Huang, and J. A. Mydosh, Phys. Rev. Lett. **104**, 106406 (2010).

[19] E. Hassinger, G. Knebel, K. Izawa, P. Lejay, B. Salce, and J. Flouquet, Phys. Rev. B **77**, 115117 (2008).

[20] G. Motoyama, N. Yokoyama, A. Sumiyama, and Y. Oda, J. Phys. Soc. Jpn. **77**, 123710 (2008).

[21] R. Yoshida, Y. Nakamura, M. Fukui, Y. Haga, E. Yamamoto, Y. Ōnuki, M. Okawa, S. Shin, M. Hirai, Y. Muraoka, and T. Yokoya, Phys. Rev. B **82**, 205108 (2010).

[22] F. L. Boariu, C. Bareille, H. Schwab, A. Nuber, P. Lejay, T. Durakiewicz, F. Reinert, and A. F. Santander-Syro, Phys. Rev. Lett. **110**, 156404 (2013).

[23] J.-Q. Meng, P. M. Oppeneer, J. A. Mydosh, P. S. Riseborough, K. Gofryk, J. J. Joyce, E. D. Bauer, Y. Li, and T. Durakiewicz, Phys. Rev. Lett. **111**, 127002 (2013).

[24] I. Kawasaki, S. Fujimori, Y. Takeda, T. Okane, A. Yasui, Y. Saitoh, H. Yamagami, Y. Haga, E. Yamamoto, and Y. Ōnuki, Phys. Rev. B **83**, 235121 (2011).

[25] M. Biasini, J. Rusz, and A. P. Mills Jr., Phys. Rev. B **79**, 085115 (2009).

[26] A. F. Santander-Syro, M. Klein, F. L. Boariu, A. Nuber, P. Lejay, and F. Reinert, Nature Phys. **5**, 637 (2009).

[27] R. Okazaki, T. Shibauchi, H. J. Shi, Y. Haga, T. D. Matsuda, E. Yamamoto, Y. Onuki, H. Ikeda, and Y. Matsuda, Science **331**, 439 (2011).

[28] S. Kambe, Y. Tokunaga, H. Sakai, T. D. Matsuda, Y. Haga, Z. Fisk, and R. E. Walstedt, Phys. Rev. Lett. **110**, 246406 (2013).

[29] Y. Kasahara, T. Iwasawa, H. Shishido, T. Shibauchi, K. Behnia, Y. Haga, T. D. Matsuda, Y. Onuki, M. Sigrist, and Y. Matsuda, Phys. Rev. Lett. **99**, 116402 (2007).

[30] C. R. Wiebe, J. A. Janik, G. J. MacDougall, G. M. Luke, J. D. Garrett, H. D. Zhou, Y.-J. Jo, L. Balicas, Y. Qiu, J. R. D. Copley, Z. Yamani, and W. J. L. Buyers, Nat. Phys. **3**, 96 (2007).

[31] A. Villaume, F. Bourdarot, E. Hassinger, S. Raymond, V. Taufour, D. Aoki, and J. Flouquet, Phys. Rev. B **78**, 012504 (2008).

[32] C. Broholm and J. K. Kjems, W. J. L. Buyers, P. Matthews, T. T. M. Palstra, A. A. Menovsky, and J. A. Mydosh, Phys. Rev. Lett. **58**, 1467 (1987).

[33] H. Ohkuni, Y. Inada, Y. Tokiwa, K. Sakurai, R. Settai, T. Honma, Y. Haga, E. Yamamoto, Y. Onuki, H. Yamagami, S. Takahashi, and T. Yanagisawa, Philo. Mag. B **79**, 1045 (1999).

[34] E. Hassinger, G. Knebel, T. D. Matsuda, D. Aoki, V. Taufour, and J. Flouquet, Phys. Rev. Lett. **105**, 216409 (2010).

[35] H. Ikeda, M. Suzuki, R. Arita, T. Takimoto, T. Shibauchi, and Y. Matsuda, Nat. Phys. **8**, 528 (2012).

[36] P. Blaha, K. Schwarz, G. K. H. Madsen, D. Kvasnicka and, J. Luitz, WIEN2K, An augmented plane wave + local orbitals program for calculating crystal properties. (Karlheinz Schwarz, Techn. Universität Wien, Austria, 2001).

[37] G. Cordier, E. Czech, H. Schafer and, P. Woll, J. Less-Common Met. **110**, 327-330 (1985).

[38] P. M. Oppeneer, J. Rusz, S. Elgazzar, M.-T. Suzuki, T. Durakiewicz, and J. A. Mydosh, Phys. Rev. B **82**, 205103 (2010).

[39] P. Santini and G. Amoretti, Physica B: Condensed Matter **206-207**, 421 (1995).

[40] H. Harima, K. Miyake, and J. Flouquet, J. Phys. Soc. Jpn. **79**, 033705 (2010).

[41] P. Santini and G. Amoretti, Phys. Rev. Lett. **73**, 1027 (1994).

[42] F. J. Ohkawa and H. Shimizu, J. Phys.: Condens. Mater. **11**, L519 (1999).

[43] K. Hanzawa, Journal of Physics: Condensed Matter **19**, 072202 (2007).

[44] K. Hanzawa, J. Phys. Soc. Jpn. **81**, 114713 (2012).

[45] A. Kiss, and P. Fazekas, Phys. Rev. B **71**, 054415 (2005).

[46] P. Fazekas, A. Kiss, and K. Radnoczi, Progress of Theoretical Physics Supplement **160**, 114 (2005).

[47] H. Kusunose and H. Harima, J. Phys. Soc. Jpn. **80**, 084702 (2011).

[48] K. Haule and G. Kotliar, Europhysics Letters **89**, 57006 (2010).

[49] K. Haule, and G. Kotliar, Nature Phys. **5**, 796 (2009).

[50] F. Cricchio, F. Bultmark, O. Granas, and L. Nordstrom, Phys. Rev. Lett. **103**, 107202 (2009).

[51] V. P. Mineev and M. E. Zhitomirsky, Phys. Rev. B **72**, 014432 (2005).

[52] H. Ikeda and Y. Ohashi, Phys. Rev. Lett. **81**, 3723 (1998).

[53] K. M. A. Virosztek and B. Dora, Int. J. Mod. Phys. B **16**, 1667 (2002).

[54] S. Elgazzar, J. Rusz, M. Amft, P. M. Oppeneer, and J. A. Mydosh, Nature Mater. **8**, 337 (2009).

[55] Y. Okuno and K. Miyake, J. Phys. Soc. Jpn. **67**, 2469 (1998).

[56] A. E. Sikkema, W. J. L. Buyers, I. Affleck, and J. Gan, Phys. Rev. B **54**, 9322 (1996).

[57] H. Amitsuka and T. Sakakibara, J. Phys. Soc. Jpn. **63**, 736 (1994).

[58] P. Chandra, P. Coleman, J. A. Mydosh, and V. Tripathi, Nature. **417**, 831 (2002).

[59] C. M. Varma, and L. Zhu, Phys. Rev. Lett. **96**, 036405 (2006).

[60] Y. Dubi, and A. V. Balatsky, Phys. Rev. Lett. **106**, 086401 (2011).

[61] V. Barzykin and L. P. Gor'kov, Phys. Rev. Lett. **74**, 4301 (1995).

[62] C. Pépin, M. R. Norman, S. Burdin, and A. Ferraz, Phys. Rev. Lett. **106**, 106601 (2011).

[63] J. G. Rau, and H.-Y. Kee, Phys. Rev. B **85**, 245112 (2012).

[64] P. S. Riseborough, B. Coqblin, and S. G. Magalhaes, Phys. Rev. B, **85**, 165116 (2012).

[65] S. Fujimoto, Phys. Rev. Lett. **106**, 196407 (2011).

[66] P. Thalmeier, and T. Takimoto, Phys. Rev. B **83**, 165110 (2011).

[67] P. Chandra, P. Coleman, and R. Flint, Nature **493**, 621-626 (2013).

[68] Y. Kohori, K. Matsuda, and T.Kohara, J. Phys. Soc. Jpn. **65**, 1083 (1996).

[69] K. Matsuda, Y. Kohori and T. Kohara, J. Phys. Soc. Jpn. **65**, 679 (1996).

[70] K. Yano, T. Sakakibara, T. Tayama, M. Yokoyama, H. Amitsuka, Y. Homma, P. Miranovic, M. Ichioka, Y. Tsutsumi, and K. Machida, Phys. Rev. Lett. **100**, 017004 (2008).

[71] A. V. Sologubenko, J. Jun, S. M. Kazakov, J. Karpinski, and H. R. Ott, Phys. Rev. B **66**, 014504 (2002).

[72] G. Seyfarth, J. P. Brizon, M. A. Measson, J. Flouquet, K. Izawa, Y. Matsuda, H. Sugawara, and H. Sato, Phys. Rev. Lett. **95**, 107004 (2005).

[73] R. Okazaki, Y. Kasahara, H. Shishido, M. Konczykowski, K. Behnia, Y. Haga, T. D. Matsuda, Y. Onuki, T. Shibauchi, and Y. Matsuda, Phys. Rev. Lett. **100**, 037004 (2008).

[74] G. Blatter, M. V. Feigel'man, V. B. Geshkenbein, A. I. Larkin, and V. M. Vinokur, Rev. Mod. Phys. **66**, 1125 (1994).

[75] A. Larkin, and A. Varlamov, *Theory of fluctuations in superconductors*, Oxford Univ. Press, Oxford (2005).

[76] E. G. Haamappel, W. Joss, P. Wyder, S. Askenazy, F.M. Mueller, K. Trubenbach, Hj. Mattausch, A. Simon, and M. Osofsky, J. Phys. Chem Sol. **54**, 1261 (1993).

[77] M. Hedo, Y. Inada, T. Ishida, E. Yamamoto, Y. Haga, Y. Onuki, M. Higuchi, and A. Hasegawa, J. Phys. Soc. Jpn. **64**, 4535 (1995).

[78] Y. Haga, Y. Inada, K. Sakurai, Y. Tokiwa, E. Yamamoto, T. Honma, and Y. Onuki, J. Phys. Soc. Jpn. **68**, 342 (1999).

[79] K. Maki, Phys. Rev. B **44**, 2861 (1991).

[80] W. R. Busing, and H. A. Levy, Acta Cryst. **22**, 457 (1967).

[81] J. A. Mydosh, and P. M. Oppeneer, Rev. Mod. Phys. **83**, 1301 (2011).

[82] K. Kuwahara, H. Amitsuka, T. Sakakibara, O. Suzuki, S. Nakamura, T. Goto, M. Mihalik, A. A. Menovsky, A. de Visser, and J. J. M. Franse, J. Phys. Soc. Jpn. **66**, 3251 (1997).

[83] N. Kernavanois, P. Dalmas de Reotier, A. Yaouanc, J.-P. Sanchez, K.D. Lib, and P. Lejay, Physica B **259**, 648 (1999).

[84] K. Matsuda, Y. Kohori, T. Kohara, K. Kuwahara, and H. Amitsuka, Phys. Rev. Lett. **87**, 087203 (2001).

[85] S. Takagi, S. Ishihara, S. Saitoh, H. Sasaki, H. Tanida, M. Yokoyama, and H. Amitsuka, J. Phys. Soc. Jpn. **76**, 033708 (2007).

[86] S. Tonegawa, K. Hashimoto, K. Ikada, Y.-H. Lin, H. Shishido, Y. Haga, T. D. Matsuda, E. Yamamoto, Y. Onuki, H. Ikeda, Y. Matsuda, and T. Shibauchi, Phys. Rev. Lett. **109**, 036401 (2012).

[87] S. Tonegawa, K. Hashimoto, K. Ikada, Y. Tsuruhara, Y.-H. Lin, H. Shishido, Y. Haga, T. D. Matsuda, E. Yamamoto, Y. Onuki, H. Ikeda, Y. Matsuda, and T. Shibauchi, (accepted in PRB)

[88] F. Bourdarot, N. Martin, S. Raymond, L.-P. Regnault, D. Aoki, V. Taufour, and J. Flouquet, Phys. Rev. B. **84**, 184430 (2011).

[89] H. Schmid, E. Burkhardt, E. Walker, W. Brixel, M. Clin, J.-P. Rivera, J.-L. Jorda, M. Francois, and K. Yvon, Z. Phys. B - Condensed Matter **72**, 305 (1988).

[90] M. A. Tanatar, A. Kreyssig, S. Nandi, N. Ni, S. L. Bud ' ko, P. C. Canfield, A. I. Goldman, and R. Prozorov, Phys. Rev. B. **79**, 180508 (2009).

[91] S. Kambe, D. Aoki, B. Salce, F. Bourdarot, D. Braithwaite, J. Flouquet, and J.-P. Brison, Phys. Rev. B. **87**, 115123 (2013).

[92] S. Kasahara, H. J. Shi, K. Hashimoto, S. Tonegawa, Y. Mizukami, T. Shibauchi, K. Sugimoto, T. Fukuda, T. Terashima, Andriy H. Nevidomskyy and Y. Matsuda, Nature **486**, 382 (2012).

[93] R. A. Borzi, S. A. Grigera, J. Farrell, R. S. Perry, S. J. S. Lister, S. L. Lee, D. A. Tennant, Y. Maeno,and A. P. Mackenzie, Science **315**, 214 (2007).

[94] T. Yanagisawa, S. Mombetsu, H. Hidaka, H. Amitsuka, M. Akatsu, S. Yasin, S. Zherlitsyn, J. Wosnitza, K. Huang, and M. B. Maple, J. Phys. Soc. Jpn. **82**, 013601 (2013).

[95] T. Shibauchi and Y. Matsuda, Physica C **481**, 229 (2012).

[96] S. Takagi, S. Ishihara, M. Yokoyama, and H. Amitsuka, J. Phys. Soc. Jpn. **81**, 114710 (2012).

[97] M. Y. Azbel', and E. A. Kaner, J. Phys. Chem. Solids **6**, 113 (1958).

[98] J. D. Jackson, *Classical Electrodynamics* (Jhon Wiley & Sons, New York, 1975).

[99] O. Klein, S. Donovan, M. Dressel, and G. Griiner, Int. J. Infrared and Millimeter Waves **14**, 2423 (1993).

[100] S. Donovan, O. Klein, M. Dressel, K. Holczer, and G. Griiner, Int. J. Infrared and Millimeter Waves **14**, 2459 (1993).

[101] G. H. Papas, J. Appl. Phys. **25**, 1552 (1954).

[102] L. D. Landau and E. M. Lifshitz, *Electrodynamics of Continuous Media* (Pergmon, Oxford, 1984).

[103] W. Kohn, Phys. Rev. **123**, 1242 (1961).

[104] K. Kanki, and K. Yamada, J. Phys. Soc. Jpn. **66**, 1103 (1997).

[105] A. J. Leggett, Ann. Phys. (N.Y.) **46**, 76 (1968).

[106] C. M. Varma, K. Miyake, and S. Schmitt-Rink, Phys. Rev. Lett. **57**, 626 (1986).

[107] K. Behnia, R. Bel, Y. Kasahara, Y. Nakajima, H. Jin, H. Aubin, K. Izawa, Y. Matsuda, J. Flouquet, Y. Haga, Y. Ōnuki, and P. Lejay, Phys. Rev. Lett. **94**, 156405 (2005).

[108] D. Aoki, G. Knebel, I. Sheikin, E. Hassinger, L. Malone, T. D. Matsuda, and Jacques Flouquet, J. Phys. Soc. Jpn. **81**, 074715 (2012).

[109] P. Aynajiana, E. H. da Silva Netoa, C. V. Parkera, Y. Huangb, A. Pasupathyc, J. Mydoshd, and A. Yazdani, Proc. Natl. Acad. Sci. U. S. A. **107**, 10383 (2010).

[110] A. R. Schmidt, M. H. Hamidian, P. Wahl, F. Meier, A. V. Balatsky, J. D. Garrett, T. J. Williams, G. M. Luke, and J. C. Davis, Nature **465**, 570 (2010).

[111] T. Shibauchi, H. Kitano, K. Uchinokura, A. Maeda, T. Kimura and K. Kishio, Phys. Rev. Lett. **72**, 2263-2266 (1994).

[112] Y. Shimono, T. Shibauchi, Y. Kasahara, T. Kato, K. Hashimoto, Y. Matsuda, J. Yamaura, Y. Nagao, and Z. Hiroi, Phys. Rev. Lett. **98**, 257004 (2007).

[113] H. Shishido, K. Hashimoto, T. Shibauchi, T. Sasaki, H. Oizumi, N. Kobayashi, T. Takamasu, K. Takehana, Y. Imanaka, T. D. Matsuda, Y. Haga, Y. Onuki, and Y. Matsuda, Phys. Rev. Lett. **102**, 156403 (2009).

[114] Y. J. Jo, L. Balicas, C. Capan, K. Behnia, P. Lejay, J. Flouquet, J. A. Mydosh, and P. Schlottmann, Phys. Rev. Lett. **98**, 166404 (2007).

[115] M. M. Altarawneh, N. Harrison, S. E. Sebastian, L. Balicas, P. H. Tobash, J. D. Thompson, F. Ronning, and E. D. Bauer, Phys. Rev. Lett. **106**, 146403 (2011).

[116] L. M. Falicov and Henryk Stachowiak, Phys. Rev. **147**, 505-515 (1966).

[117] T. Ebihara, I. Umehara, A. K. Albessard, K. Satoh, and Y. Ōnuki, J. Phys. Soc. Jpn. **61**, 1473-1476 (1992).

[118] S. Tonegawa, S. Kasahara, T. Fukuda, K. Sugimoto, N. Yasuda, Y. Tsuruhara, D. Watanabe, Y. Mizukami, Y. Haga, T. D. Matsuda, E. Yamamoto, Y. Onuki, H. Ikeda, Y. Matsuda, and T. Shibauchi, (unpublished).

[119] H. D. Drew, and T. C. Hsu, Phys. Rev. B **52**, 9178 (1995).

[120] N. B. Kopnin, and V. M. Vinokur, Phys. Rev. Lett. **87**, 017003 (2001).

[121] N. B. Kopnin, and V. M. Vinokur, Phys. Rev. B **62**, 9770 (2000).

[122] N. B. Kopnin, Phys. Rev. B **57**, 11775 (1998).

[123] T. Shibauchi, M. Sato, A. Mashio, T. Tamegai, H. Mori, S. Tajima, and S. Tanaka, Phys. Rev. B **55**, R11977 (1997); T. Shibauchi, T. Nakano, M. Sato, T. Kisu, N. Kameda, N. Okuda, S. Ooi, and T. Tamegai, Phys. Rev. Lett. **83**, 1010 (1999).

[124] A. Amato, Rev. Mod. Phys. **69**, 1119-1180 (1997).

[125] Z. Zhu, E. Hassinger, Z. Xu, D. Aoki, J. Flouquet, and K. Behnia, Phys. Rev. B **80**, 172501 (2009).

[126] T. Sasaki, W. Biberacher, K. Neumaier, W. Hehn, K. Andres, and T. Fukase, Phys. Rev. B **57**, 10889?10892 (1998)

[127] T. Shibauchi, L. Krusin-Elbaum, G. Blatter, and C. H. Mielke, Phys. Rev. B **67**, 064514 (2003).

Acknowledgements

I would like to thank Professor Takasada Shibauchi for his continuous supports, and warm encouragement throughout my PhD student course. His valuable guidance and great perspective helped me in all the time of research. I also would like Professor Yuji Matsuda, who provides me with extensive advice and fruitful discussion on my experimental results. Had it not been for them, I would never have developed this study.

I wish to express my great appreciation Professor Yoshichika Onuki, Dr. Yoshinori Haga, Dr. Tatsuma Matsuda and Dr. Etsuji Yamamoto for providing with high-quality URu_2Si_2 single crystals. I also would like to acknowledge Dr. Tatsuo Fukuda, Dr. Kunihisa Sugimoto and Dr. Nobuhiro Yasuda who support X-ray experiments at Spring8.

I would like to thank Professor Takahito Terashima, Professor Minoru Yamashita and Professor Hiroaki Shishido for experimental supports and helpful discussion. I would like to thank Professor Shigeru Kasahara, Professor Kenichiro Hashimoto and Professor Ryuji Okazaki for teaching experimental technique and thinking skills. I would like to appreciate Mr. Yuta Mizukami, Mr. Daiki Watanabe, Mr. Kousuke Ikada, Mr. Yugo Tsuruhara, Ms. Yao-Han Lin and Mr. Takuya Yamashita for experimental assistance. I am also deeply indebted to all members of Professor Matsuda and Professor Shibauchi group in Kyoto University, namely Mr. Masaaki Shimozawa, Mr. Takuya Mikami, Mr. Yuta Kawamoto, Mr. Tatsuya Watashige, Mr. Ryota Endou, Mr. Satoshi Kurata.

I wish to acknowledge the financial support provided by the Research Fellowship of the Japan Society for Promotion of Science for Young Scientists.

Finally, I would like to express my gratitudes to my parents, my sister and the rest of my family for their supports and warm encouragement.